THE UNIVERSITY
of EDINBURGH

This thesis has been submitted in fulfilment of the requirements for a postgraduate degree (e.g. PhD, MPhil, DClinPsychol) at the University of Edinburgh. Please note the following terms and conditions of use:

This work is protected by copyright and other intellectual property rights, which are retained by the thesis author, unless otherwise stated. A copy can be downloaded for personal non-commercial research or study, without prior permission or charge. This thesis cannot be reproduced or quoted extensively from without first obtaining permission in writing from the author. The content must not be changed in any way or sold commercially in any format or medium without the formal permission of the author. When referring to this work, full bibliographic details including the author, title, awarding institution and date of the thesis must be given.

School of Engineering, University of Edinburgh

THE UNIVERSITY
of EDINBURGH

Passive Load Alleviation by Morphing Blades for Tidal Turbines

Gabriele Pisetta

A dissertation submitted to the University of Edinburgh in accordance with the requirements of the degree of Doctor of Philosophy in the School of Engineering.

November 2021

Lay Summary

All around the world, scientists, engineers, and amateurs are putting lots of efforts to develop devices that harvest energy from renewable energy sources. One of the most promising technologies are tidal turbines. These devices are placed at the bottom of the sea and use tidal currents to spin their blades and generate electricity. Thanks to the regularity of the tides, tidal turbines will constitute a green, reliable, and predictable source of energy for our future needs. However, there is a catch: this technology is not ready yet.

Tidal turbines are still too expensive to be deployed on such a large scale as wind turbines. They are designed to operate for 20 years, but predictions estimated a much shorter lifespan. This happens because of the harshness of the marine environment, where waves and currents generate ever changing flow conditions that cause massive load fluctuations on the turbine blades. The blades eventually break, decreasing the lifespan of the device and causing the need for expensive maintenance operations.

The question is: how can we make those blades survive for 20 years?

In my PhD project, I investigated a particular design called morphing blades. The idea is that a part of the blade is flexible such that when the flow conditions change, the blade can bend to mitigate the load fluctuations. Much like a fish swims smoothly by flapping its body.

In this thesis, I present the results from a numerical code I developed that simulates a tidal turbine equipped with morphing blades, I explain the physics underlying load mitigation by morphing blades, and I present the findings from proof-of-concept experiments I performed in a world-leading testing facility. Results are very promising: I found that once optimised, the system can alleviate up to 99% of load fluctuations responsible for the blade damage. Moreover, experiments confirmed that morphing blades are capable of alleviating load fluctuations in all the tested conditions. This means that

morphing blades will generate the electricity that we need, but they won't break. Therefore, if we equip tidal turbines with morphing blades, those turbines will last longer, they will cost less, and they will grant us a greener future.

This work aims to underpin the future development of morphing blades by providing a simple, yet reliable numerical model, and by proving experimentally the capabilities of this technology.

Abstract

This thesis presents a novel passive load control to reduce the unsteady hydrodynamic loads on the blades of tidal turbines, enabling lighter, more resilient and less expensive turbines.

Existing load control strategies are inadequate to mitigate the high frequency loads experienced by tidal turbines. The ideal solution should provide a fast, local control action on every section of the blade. Research on wind turbines suggests that the most promising option are trailing edge flaps, and passive, flexible materials are recommended over rigid control surfaces to maximise the device reliability.

Beyond some pioneering examples of morphing blades, the fundamental principles underlying their efficacy have yet to be fully understood, withholding further development and the adoption by the industry.

I present a numerical investigation of morphing blades to show the principles underlying unsteady load alleviation by morphing blades, and I demonstrate their capabilities via proof-of-concept experiments.

I develop a low-order model where the blade flexibility is represented by a torsional spring that controls the blade pitch motion, and I optimise the system for a specific turbine design operating in different flow conditions. The fluctuations of the root bending moment can be reduced up to 99% when the turbine operates in shear flow, and by 87% when operating in large wave conditions. The system is governed by the blade flexibility, but the blade inertia, material damping, and unsteady flow phenomena can affect the load-alleviating performance greatly.

To verify the system capabilities, I conduct a series of experiments in FloWave, a 25 m wide, 2 m deep, circular tank testing facility, using a 1:15 scale turbine and custom designed passively-pitching blades. The system consistently reduces the fluctuations of the root bending moment, thrust

and torque over a range of different tip speed ratios. While the experiments featured a passively-pitching blade, the results are a good indication of the potential of morphing blades, and the analytical low-order code is equally representative of a rigid blade with a flexible trailing edge.

This work aims to underpin the future development of morphing blades by providing a simple, yet reliable numerical model, and by proving experimentally the capabilities of this technology.

Keywords: unsteady load mitigation, passive load control, pitch control, morphing, fluid-structure interaction, tidal turbine

Declaration

I declare that this thesis was composed by myself, that the work contained herein is my own except where explicitly stated otherwise in the text, and that this work has not been submitted for any other degree or professional qualification except as specified.

Parts of this work have been published in the journal article:

Pisetta, G., Le Mestre, R., & Viola, I. M. (2021). **Morphing blades for tidal turbines: A theoretical study**. Renewable Energy

Gabriele Pisetta

July 30, 2022

Contents

Lay Summary **ii**

Abstract **iv**

Declaration **v**

Contents **vi**

List of figures **ix**

List of tables **xv**

Nomenclature **xxi**

1 Introduction **1**

1.1 The tidal environment 1
1.2 Turbine's unsteady loads 3
1.3 Load control systems 5
1.3.1 Actively controlled trailing edge flaps 6
1.3.2 Passive trailing edge flaps 9
1.4 Morphing blades background 10
1.5 Morphing blades for tidal turbines 13
1.6 Summary of previous work and motivation 14
1.7 Scope of the PhD 15
1.8 Overview of the thesis 16

2 Literature on morphing blade models **17**

2.1 Turbine modelling 17
2.2 Morphing blade modelling 19
2.2.1 Early models from aeronautics 19
2.2.2 Morphing blades models for wind turbines 21
2.2.3 High-fidelity models 21

2.2.4 Flexible flapping foils 22
2.2.5 Revisiting conventional flaps and the impulse method . 22
2.3 Overview of morphing blade model for tidal turbines 23

3 Numerical method: how to model a morphing blade 25
3.1 Rigid Blade Model 25
3.2 Morphing Blade Model 31
3.3 Quasi-steady Analysis of a Morphing Foil 34
3.4 Quasi-steady Analysis of the 3D Morphing Blade 37
3.5 Dynamic Analysis of the 3D Morphing Blade 39
3.5.1 Unsteady Hydrodynamics 42
3.6 Real inflow conditions 46
3.6.1 Fourier decomposition of generic inflow 47

4 Code inputs and validation 50
4.1 Input parameters 50
4.2 Code Validation 51

5 Numerical results 63
5.1 Quasi-steady Analysis of a Morphing foil 63
5.2 Quasi-steady Analysis of the 3D Morphing Blade 67
5.3 Dynamic Analysis of the 3D Morphing Blade 71
5.4 Effect of Blade Mechanical Damping 73
5.5 Morphing blade performance in real flow conditions 75

6 Experimental method 79
6.1 The FloWave facility 80
6.2 Turbine model 80
6.3 Passive-pitch blade model design 82
6.3.1 Blade design 82
6.3.2 Passive-pitch system design 86
6.3.3 Torsional spring design 87
6.3.4 Model assembly and operating principle 88
6.4 Structural considerations on the passive-pitch system 90
6.4.1 Harshest flow condition and maximum design loads . . 90

6.4.2 Blade and composite components 92
6.4.3 Shaft and casing 95
6.4.4 Bearings 96
6.5 Instrumentation 97
6.6 Test programme and execution 98
6.7 Data analysis 100
6.8 Uncertainty analysis 102

7 Experimental results **105**
7.1 Benchmark case: the rigid blade 105
7.1.1 Turbine instability 109
7.2 Passive-pitch system effectiveness 111
7.2.1 Effect of preload angle 111
7.2.2 Effect of friction on the system performance 116
7.2.3 Load mitigation 118
7.3 Discussion 125
7.4 Differences between experiments and low-order model 129

8 Conclusions **132**
8.1 Future work 135

References **137**

List of figures

1.1 Schematic diagram of a passive flap actuation based on a (red) counterweight (Bottasso et al. [76]). 9
1.2 Schematic diagram of the adaptive camber airfoil (Cordes et al. [77]). The leading edge motion drives the deflection of the trailing edge. 10
1.3 Schematic diagram of the first adaptive blade system (Cheney and Spierings [85]). When the blade speed increases due to a gust, the greater centrifugal force moves the pendulum mass (red circle) towards the rotor plane, thus increasing the blade pitch angle. 11
1.4 Schematic diagram of the passive blade tip (Kuik and Dekker [90]). Under higher speed, the centrifugal force pulls the blade tip outwards, and the screw cylinder twists it to feather. 13

3.1 Schematic diagram of a tidal turbine coordinate systems. On the left, the side view shows the interaction of the turbine with a shear flow. On the right, front view of the turbine. 26
3.2 Flow velocities and forces acting on a 2D blade section. 28
3.3 Morphing blade concept. Part of the blade can bend to mitigate inflow fluctuations. 31
3.4 Morphing blade model. The flexibility is modelled by a torsional spring. 32
3.5 Morphing blade models. 33
3.6 The blade is composed by a composite shell filled with water. . 40
3.7 A generic small element of a section that does not lie on the pitch axis is subjected to a centrifugal moment $\boldsymbol{M}_{\mathrm{c}}^{B}$. 41
3.8 The fluctuations of the angle of attack are approximated by a sinusoidal shape (shown here for $r = 0.75R$). 43

3.9 Time history of the angle of attack at $r/R = 0.75$. Graph shows original signal (blue line), and signal approximated using 50 (red dashed line), 100 (green dot-dash line), and 150 (purple dotted line) Fourier components respectively. 48

4.1 TGL blade geometry adapted from Gretton and Ingram [174]. 51
4.2 Quarter chord pitching moment coefficient for a NACA $63_3 - 418$ as a function of α, at Re $= 3 \times 10^6$. Data taken from Abbott and Von Doenhoff [175]. 51
4.3 Spanwise thrust distribution. Comparison of sectional thrust predicted using quasi-steady and unsteady models with experimental results from NREL UAE VI, at four different wind speeds. 54
4.4 Spanwise torque distribution. Comparison of sectional torque predicted using quasi-steady and unsteady models with experimental results from NREL UAE VI, at four different wind speeds. 55
4.5 Thrust, torque and RBM at different wind speeds/TSR. The horizontal axis on the bottom indicates the TSR, whereas the horizontal axis on the top indicates the corresponding wind speed. 56
4.6 Comparison of the BEMT results of this study and the CFD results from Gretton and Ingram [174] using $U_{\text{hub}} = 2$ m s^{-1}. C_P and C_T refer to the entire turbine. 57
4.7 Lift coefficient on an oscillating foil NACA0012, with reduced frequency $\overline{\kappa} = 0.4$, $\overline{\alpha} = 0$ deg, $\alpha = \overline{\alpha} \pm 6.7$ deg. Present results are compared to numerical and experimental data. 59
4.8 Comparison of CFD and analytical results showing the difference of C_T between rigid and morphing blades. 60
4.9 Comparison of CFD and analytical results showing the difference of C_T between rigid and morphing blades. Continuous lines represent the CFD results, dashed lines represent low-order model results (blue - rigid, red - morphing). 62

5.1 Section at $r = 0.5R$: evolution of angle of attack (a) and thrust coefficient (b). 64
5.2 Section at $r = 0.75R$: evolution of angle of attack (a) and thrust coefficient (b). 64
5.3 Reaction of the morphing foil to an increase of angle of attack and flow speed; (a) reference condition; (b) effect of the angle of attack only and (c) combined effect of the increase of both the angle of attack and flow speed. 65
5.4 Fluctuations of $C_T^{2\mathrm{D}}$ (top) and α (bottom) for the section at $r = 0.75R$, for a range of values of Γ. 66
5.5 Variations of the power and thrust coefficients as the inflow angle varies through the rotation of the blade, (a) for a large range of values $\Gamma \in [10^{-5}, 10]$ and (b) around $\Gamma_0 = 4.5 \times 10^{-4}$. 67
5.6 Map of the angle of attack fluctuations over the rotor disc for (a) a rigid blade and (b) a morphing blade. For each blade section, the values are normalised by the average angle of attack on that section. 69
5.7 Map of the thrust coefficient over the rotor disc for (a) a rigid blade and (b) a morphing blade. 69
5.8 Quasi-steady analysis of the flapwise one-blade root bending moment C_{RBM}. The blade is equipped with a spring with $C_\kappa^{\mathrm{qs}} = 6.0 \times 10^{-3}$ and $\theta_0^{\mathrm{qs}} = 313$ deg. 70
5.9 Dynamic analysis of the evolution of C_{RBM}. The blade is equipped with a spring with $C_\kappa^{\mathrm{dy}} = 1.1 \times 10^{-2}$ and $\theta_0^{dy} = 171$ deg. 71
5.10 Dynamic contributions to the moment equilibrium of the blade, for $C_\kappa^{\mathrm{dy}} = 1.1 \times 10^{-2}$ and $\theta_0^{dy} = 171$ deg. 72
5.11 Normalised amplitude of the root bending moment for a range of values of C_κ and C_μ. 74
5.12 Evolution of $\Delta\theta$ for a range of values of C_κ and C_μ. 75
5.13 Root bending moment under real flow conditions from quasi-steady analysis of a rigid blade (blue line) and a morphing blade (red dashed line). 76

5.14 Root bending moment under real flow conditions from the dynamic analysis of a rigid blade (blue line) and a morphing blade (green dash-dot line). 77

6.1 Schematic of FloWave in plan and oblique section showing: (A) Wavemaker paddles around circumference (168 Nr) (B) Turning vanes and flow conditioning filters (C) Current drive impeller units (28 Nr) (D) Buoyant raisable floor (15 mØ) below test area (E) Idealised streamlines of flow across tank floor. (Noble et al. [163]) 81
6.2 Passive-pitch blade design (left) and realised model on the tank floor (right). 83
6.3 Blade dimensions. Each section is numbered from 1 (root) to 20 (tip) and is described by the position along the blade span, or radius, the chord length and the position of the pitch axis with respect to the leading edge as a percentage of the chord. 84
6.4 Overview of the blade pressure side (left) and of the trailing edge (right). The bottom of both pictures shows the perforated flange used to bolt the blade shell to the passive-pitch system. 86
6.5 Passive-pitch system components: A) flanged cone; B) shaft; C) torsional spring; D) circlips to retain E) bearings; F1, F2) casing halves; G) angular plate; H1, H2) fairing. 87
6.6 Blade and passive-pitch system assembled (left) and section of the assembly (right). 89
6.7 Outline of structural analysis of blade and passive-pitch system. 91
6.8 Estimated blade loads at $U_\infty = 0.9$ m s^{-1} over a range of tip speed ratios λ. From the top, showing the distribution of thrust (dT) and torque (dQ) along the blade span, and the bending moment (RBM). At $\lambda = 9.5$, the blade experiences the highest bending moment and zero torque: the positive torque contributions (green-shaded) are cancelled by the negative contributions (red-shaded). 93

6.9 Load path from the blade to the hub. The hydrodynamic pressure (green arrows) loads the blade which transfers the stresses (red arrow-path) to the inner cone. The stresses climb up the cone and are transferred to the shaft, they pass through the bearings and the casing and are finally transferred to the hub. 95
6.10 Measured spring moments. Each curve represents a different spring and each measurement point feature a one-standard deviation errorbar. 104

7.1 Average values of rotor torque Q, thrust T and rigid blade root bending moment RBM at flow speed $U_\infty = 0.8$ m s^{-1}. The load fluctuations are represented by one standard deviation errorbars. 106
7.2 Torque power spectra at different tip speed ratios λ, $U_\infty = 0.8$ m s^{-1}. The dashed, vertical lines identify the frequency of relevant load harmonics. 108
7.3 Thrust power spectra at different tip speed ratios λ, $U_\infty = 0.8$ m s^{-1}. The dashed, vertical lines identify the frequency of relevant load harmonics.The red circles identify a periodic load that happens at a fixed frequency and does not depend on the rotational speed of the turbine. 109
7.4 RBM power spectra at different tip speed ratios λ, at $U_\infty = 0.8$ m s^{-1}. The dashed, vertical lines identify the frequency of relevant load harmonics. The red circles identify a periodic load that happens at a fixed frequency and does not depend on the rotational speed of the turbine. 110
7.5 Spectra at different tip speed ratios λ, at $U_\infty = 0.8$ m s^{-1}. Starting from the top, the graphs show the torque spectra, thrust spectra, the spectra of the point-measured flow velocities, and the spectra of the rotational speed of the turbine at $U_\infty = 0.8$ m s^{-1} and in the absence of flow. ($^*\lambda$ for the "no flow" condition represent the turbine rotational speed and are computed using a flow speed of 0.8 m s^{-1}) 112

7.6 Average values of rotor torque Q, thrust T and root bending moment RBM for the rotor with one passively pitching blade, at flow speed $U_\infty = 0.8$ m s^{-1}. The fluctuations of loads and λ are represented by vertical and horizontal one standard deviation errorbars respectively. The rigid blade loads are shown as dashed black lines. (*Passive Pitch, preload angle is indicated in parenthesis) 113
7.7 Spring dimension and clearance from shaft. 118
7.8 Mitigation of the amplitude of torque Q, thrust T, root bending moment M_{RB}, and rotational speed ω fluctuations with respect to the fully-rigid rotor. The amplitudes are represented by the respective standard deviations. Green bars indicate a reduction of the amplitude, red bars indicate an increase. . . . 119
7.9 Power spectra of torque Q, thrust T, root bending moment M_{RB} and rotor speed ω at $\lambda = 4.5$. Each graph compares the spectra of the rigid and the passive pitch systems. (*Passive Pitch, preload angle is indicated in parenthesis) 121
7.10 Power spectra of torque Q, thrust T, root bending moment M_{RB} and rotor speed ω at $\lambda = 5$ (left) and $\lambda = 6$ (right). Each graph compares the spectra of the rigid (black) and the passive pitch systems (blue and cyan). (*Passive Pitch) 122
7.11 Power spectra of torque Q, thrust T, root bending moment M_{RB} and rotor speed ω at $\lambda = 7$. Each graph compares the spectra of the rigid and the passive pitch systems. (*Passive Pitch) 126
7.12 Power spectra of torque Q, thrust T, root bending moment M_{RB} and rotor speed ω at $\lambda = 8$. Each graph compares the spectra of the rigid and the passive pitch systems. (*Passive Pitch) 127

List of tables

1.1 Loads increase on tidal turbines subjected to unsteady flow conditions with respect to quasi-steady loads(*the effects are replicated using the oscillating mounting of the turbine). . . . 4
1.2 Effectiveness of active trailing edge flaps for unsteady load mitigation. (*2D means two-dimensional, 3D means three-dimensional) 8

4.1 Blade geometry. 52
4.2 Simulation parameters. 53

5.1 Minimum load fluctuations using optimal springs for two blade sections. The number in parenthesis refer to the respective rigid blade sections. 64
5.2 Optimal quasi-steady results for the morphing blade model. . 70
5.3 Optimal dynamic results for the morphing blade model. The numbers within the parenthesis refer to the quasi-steady analysis that employed the spring optimised for the dynamic case. 73
5.4 Optimal morphing blade when subjected to real flow conditions (quasi-steady analysis). 76
5.5 Optimal morphing blade when subjected to real flow conditions (dynamic analysis). The numbers in parenthesis show the results obtained for a quasi-steady analysis when the inflow is Fourier-approximated as for the dynamic analysis. . . . 77

6.1 Structural parameters of the blade root section. 94

7.1 Change in spring dimension and clearance from shaft due to preloading. 118

7.2 Mitigation of loads variance across different frequency components and tip speed ratio. The values represent the variance of the passively pitching blade loads as a fraction of the variance of the rigid blade loads. Values smaller than one indicate a reduction of the variance associated to that frequency component. (* For $\lambda = 6$, only one frequency band is considered above the 3P band, since there is no load peak at 4.5 Hz) . . . 123

7.3 Mitigation of RBM variance across different frequency components and tip speed ratios. The values represent the variance of the passively pitching blade loads as a fraction of the variance of the rigid blade loads. Values smaller than one indicate a reduction of the variance associated to that frequency component. (* For $\lambda = 6$, only one frequency band is considered above the 3P band, since there is no load peak at 4.5 Hz) . . 124

7.4 Mitigation of loads variance across different frequency components and tip speed raios. The values represent the variance of the passively pitching blade loads as a fraction of the variance of the rigid blade loads. Values smaller than one indicate a reduction of the variance associated to that frequency component.128

7.5 Mitigation of RBM variance across different frequency components and tip speed ratios. The values represent the variance of the passively pitching blade loads as a fraction of the variance of the rigid blade loads. Values smaller than one indicate a reduction of the variance associated to that frequency component. 128

Nomenclature

A area swept by the blade [m^2]

A^{2D} perimeter of a blade annulus [m]

$C(k)$ Theodorsen's function [-]

C^{c}_{am} circulatory damping coefficient [Nm $s^{-1}deg^{-1}$]

C^{nc}_{am} non-circulatory damping coefficient [Nm $s^{-1}deg^{-1}$]

C_{κ} stiffness coefficient [-]

C^{dy}_{κ} optimal stiffness coefficient (dynamic analysis) [-]

C^{qs}_{κ} optimal stiffness coefficient (quasi-steady analysis) [-]

C_{RBM} root bending moment coefficient [-]

C_{tot} total damping [Nm $s^{-1}deg^{-1}$]

C_{μ} damping coefficient [-]

C_D drag coefficient [-]

C_L lift coefficient [-]

C_M foil's pitching moment coefficient [Nm]

C_P power coefficient [-]

C_P^{2D} sectional power coefficient [-]

C_T thrust coefficient [-]

C_T^{2D} sectional thrust coefficient [-]

D drag force [N]

E_{Al} aluminium Young's modulus [GPa]

F force [N]

F_{Co} Coriolis force [N]

F_{Eu} Euler force [N]

F_c centrifugal force [N]

I_{am} added mass coefficient [Nm s^2deg^{-1}]

I_y section second moment of area [mm^4]

J blade pitching inertia [kgm^2]

J^{2D} blade section inertia [kgm]

J_{tot} total inertia [kgm^2]

K_{S1}, K_{S2}, β_S bearings empirical constants [-]

K_{am} added stiffness coefficient [Nmdeg^{-1}]

K_{tot} total stiffness [Nmdeg^{-1}]

L lift force [N]

M pitching moment [Nm]

M_c^{2D} sectional centrifugal moment [N]

M_{dy}^{2D} hydrodynamic moment on a blade section [N]

M_{qs}^{2D} sectional quasi-steady hydrostatic moment [N]

M_{RB} root bending moment [Nm]

M_c blade centrifugal moment [Nm]

M_{dy} hydrodynamic moment on the blade [Nm]

M_{qs} blade quasi-steady hydrostatic moment [Nm]

M_{seal} bearings friction moment [Nm]

M_s spring moment [Nm]

M_s^{2D} spring moment per unit span [N]

N number of blade sections [-]

N_b number of blades [-]

N_k number of Fourier component [-]

P power extracted [W]

P^{2D} sectional power [Wm^{-1}]

Q blade torque [Nm]

R tip radius [m]

S_Q power spectrum [N^{2}m^2/Hz]

S_T power spectrum [N^2/Hz]

S_ω power spectrum [rpm^2/Hz]

S_{U_x} power spectrum [m^{2}s^{-2}/Hz]

T blade thrust force [N]

T^{2D} sectional thrust force [Nm^{-1}]

U inflow velocity [m s^{-1}]

U_{hub} free stream velocity at hub height [m s^{-1}]

U_x axial component of the inflow velocity [m s^{-1}]

U_∞ free stream velocity [m s^{-1}]

U_ψ tangential component of the inflow velocity [m s^{-1}]

ZZ' plane of a generic blade section [-]

$\boldsymbol{A}$ position of the pitching axis of a section [m]

$\boldsymbol{B}$ position of a generic point on a section [m]

$\overline{\boldsymbol{AB}}$ distance of a generic point from the pitching axis of a section [m]

δr span of a section [m]

γ angular coordinate on a blade section [m]

$\hat{C}_M$ flat plate's pitching moment coefficient [Nm]

$\hat{F}$ Prandtl's tip loss factor [-]

$\hat{J}$ objective function of the optimisation problem [-]

$\hat{T}$ period of a periodic quantity [s]

$\hat{x}$ chordwise coordinate on a blade section [m]

$\hat{x}_A$ distance of the pitching axis from the leading edge of a section [m]

Re Reynolds number [-]

μ blade mechanical damping [Nm s^{-1}deg^{-1}]

ψ blade azimuthal position [deg]

a axial induction factor [-]

a' tangential induction factor [-]

b half-chord length [m]

c chord length [m]

d distance of the pitching axis from the half chord [m]

f Prandtl's tip loss factor exponent [-]

f_k/ ω_k frequency [Hz]/[rad s^{-1}]

m mass of a small blade element [kg]

r radial coordinate [m]

r_{CG} radial coordinate of centre of gravity [m]

t time [s]

t_h thickness of blade shell [mm]

x horizontal streamwise coordinate [m]

xy foil thickness in percentage of chord [-]

y distance of blade shell from centre of section [mm]

z vertical coordinate from the seabed [m]

z_{hub} height of the hub from the seabed [m]

$\mathrm{d}Q$ sectional torque [Nm]

$\mathrm{d}T$ sectional thrust force [N]

d_S bearings seal counterface diameter [mm]

var variance [*]

Γ sectional non-dimensional stiffness [-]

Γ_0 optimal sectional non-dimensional stiffness [-]

Ω_N system natural frequency [radss^{-1}]

Ω_{s} blade cross-sectional shell area [m^2]

Ω_{w} blade cross-sectional internal area [m^2]

α angle of attack [deg]

β pitch angle [deg]

β_0 twist angle [deg]

χ_k phase of Fourier component [deg]

κ stiffness of the spring [Nmdeg^{-1}]

κ^{2D} spring stiffness per unit span [Ndeg^{-1}]

λ tip speed ratio [-]

λ_0 optimal tip speed ratio [-]

ω rotational speed [rads^{-1}]

$\overline{\kappa}$ reduced frequency [-]

ϕ inflow angle [deg]

ρ_s density of blade shell [kgm^{-3}]

ρ_w density of water [kgm^{-3}]

σ standard deviation [*]

σ_{Al} aluminium yield strength [MPa]

σ_B computed bending stress [Mpa]

τ_f bypass blocked flow factor [-]

θ spring strain angle [deg]

θ^{dy} spring strain angle (dynamic analysis) [deg]

θ_0^{dy} optimal preload (dynamic analysis) [deg]

θ^{qs} spring strain angle (quasi-steady analysis) [deg]

θ_0^{qs} optimal preload (quasi-steady analysis) [deg]

θ_0 preload of the spring [deg]

ζ damping ratio [-]

2D Two-dimensional

3D Three-dimensional

BEMT Blade Element Momentum Theory

HATT Horizontal Axis Tidal Turbine

HAWT Horizontal Axis Wind Turbine

LCOE Levelised Cost Of Energy

Nomenclature note: time derivatives are shown with a dot above the variable; overbars show mean values over a blade revolution; bold symbols describe vector variables; Δ represents the difference between the maximum and minimum values of a fluctuating variable; δ represents a small variation; quantities that refer to the rigid fixed-pitch turbine are indicated by subscripts $|_{\kappa\to\infty}$. * this variable takes the unit of the quantity it represent.

1

Introduction

Tidal energy is a promising renewable energy source that could critically contribute to energy security [1]. The world's first arrays of tidal turbines (Meygen and Nova's Bluemull Sound, 2016) have only recently been deployed in Scotland. For this energy sector to develop further, new technology must be developed to reduce the levelised cost of energy (LCOE), which is the minimum constant price at which electricity has to be sold in order to break-even over the lifetime of the project. Technology that enables more reliable and cheaper tidal turbines would contribute to a reduction in the LCOE and it would provide more competitive renewable energy.

1.1 The tidal environment

Tidal turbines operate from cut-in speeds of 1 ms^{-1} or less [2], and are typically deployed at sites and where the water current can reach up to 5 ms^{-1}. For typical MW-rated turbines, like the TGL turbine considered in this work (see Chapter 3), SIMEC Atlantis AR1500 turbine [2], and Orbital Marine Power O2 [3], the rotor diameter is $18 - 20$ m and the Reynolds number, at the device scale, is $1 - 8 \cdot 10^6$. The tidal stream is vertically sheared with turbulence intensities in the streamwise direction of up to 20%, dominant time scales of $6 - 10$ s, and integral length scales of tens of meter in the streamwise direction but with significantly smaller magnitudes in the vertical and transverse directions [4, 5].

Tidal deployment sites are often close to the land, where the current speed

is enhanced by local conformations like channels, coastal inlets or bays, a headland, or an island near a land mass. In such shielded locations, waves are not as strong as mid-ocean swells which can reach up to 20 m, but can still achieve heights of several meters. Whelan et al. [6] indicated that a ten-year wave at a typical tidal site (i.e. an extreme wave that occurs statistically once every ten years) has a period of 9 s, significant wave height 9 m, and can cause velocity fluctuations of up to 3 ms^{-1}. However, such extreme wave is slow, with frequency 0.7 rads^{-1}, corresponding to about one third of the rotational frequency of a large turbine (e.g. SIMEC Atlantis AR1500 operates around 14 rpm, or $\omega = 2.1$ rads^{-1} [2]), or several blade revolutions for a smaller and faster kW-rated turbine. Conversely, a more regular wave pattern with a significant wave height of 0.75 m, has a shorter period of about 3 s and frequency 2.1 rads^{-1}, comparable to the rotational frequency of the turbine. Although the magnitude of the flow speed fluctuations is smaller, the turbine blades experience greater flow unsteadiness due to the higher frequency of the phenomenon.

Sequeira and Miller [7] summarised the parameter space of unsteady flow conditions experienced by tidal turbines at the blade mid-span section as follows. Wave-induced flow fluctuations are mainly low frequency (reduced frequency $\overline{\kappa} = \omega c/U < 0.2$) that may be approximated as a quasi-steady phenomena with large amplitude that can push the blade past its static stall angle. Instead, seabed turbulence has typically small amplitude but higher frequency ($\overline{\kappa} \leq 0.7$) and should be approximated using unsteady flow models. Rotating through a shear current causes moderate flow unsteadiness ($\overline{\kappa} \approx 0.2$) with fluctuation amplitudes comparable to those caused by turbulence.

When considering the blade onset flow, each section experiences different inflow velocities, corresponding to different levels of unsteadiness. Near the root, where the velocity due to the blade rotation is small, unsteady flow generates greater fluctuations than at the tip, where the onset flow velocity is dominated by the rotational component. Scarlett et al. [8] showed that on a full-scale turbine operating in large wave conditions, a section at the blade tip

($r/R = 0.96$, i.e. 96% of the blade span) experiences flow fluctuations at low frequency $\overline{\kappa} \approx 0.02$, which cause quasi-steady fluctuations with magnitude $\Delta\alpha = \max(\alpha) - \min(\alpha) \leq 6$ deg within the attached flow region. Near the mid span ($r/R = 0.40$), larger fluctuations ($\Delta\alpha \approx 10$ deg) cause the angle of attack to slightly exceed the static angle of attack, however, the unsteadiness generated by the moderate frequency $\overline{\kappa} \approx 0.2$ delays the onset of separation thus preventing it. At the root ($r/R = 0.15$), flow fluctuations at high reduced frequency ($\overline{\kappa} \approx 0.3$) and high magnitude fluctuations of the angle of attack ($\Delta\alpha \approx 16$ deg) generate highly unsteady conditions. Since root sections operate around the static stall angle, they experience deep dynamic stall, with abrupt separation near the leading edge and generation of large vortices which cause large load fluctuations. In the presence of additional unsteady phenomena like, for instance, strong turbulence and yawed flow, the unsteadiness over the lower half of the blade can reach even higher reduced frequency ($\overline{\kappa} > 0.56$) causing even larger load fluctuations [9].

1.2 Turbine's unsteady loads

The large load fluctuations induced by the shear and turbulence of the onset flow, wave-induced current fluctuations, yaw misalignment, interaction with the support structures, wave-induced motion of floating devices, and wakes of the upstream devices present a major challenge to the design of tidal turbines [8, 10]. In particular, Scarlett and Viola [9] developed a code based on blade element momentum theory to study the unsteady loads on an 18 m diameter tidal turbine and they found that waves and turbulence are the main sources of unsteady loads. Using onset flow conditions measured at the European Marine Energy Centre (EMEC) test site, they showed that a turbine operating in large waves experiences fluctuations of the root bending moment that can exceed by 50% the steady-state values [8]. Similar conclusions are shared by other authors, who measured significantly higher loads when the turbine was subjected to waves and large scale turbulence compared to quasi-steady reference loads (Table 1.1). As a result, tidal turbine blades are designed with high safety factors, which leads to thick structures with short fatigue

Authors	Method	Disturbance	Loads
Scarlett et al. [8]	low-order code	waves	root bending moment +50%
Barltrop et al. [12]	wave tank experiments	waves	peak thrust +40%
Galloway et al. [13]	wave tank experiments	waves	root bending moment +175%
Milne et al. [14]	towing tank*	waves, large scale turbulence*	root bending moment +15% (attached flow)
Milne et al. [15]	towing tank*	waves, large scale turbulence*	root bending moment +25% (dynamic stall)

Table 1.1: Loads increase on tidal turbines subjected to unsteady flow conditions with respect to quasi-steady loads(*the effects are replicated using the oscillating mounting of the turbine).

life that push up capital and operational costs [11].

The development of tidal farms will see the deployment of a large number of turbines in array configurations. To increase local blockage and thus yields, tidal turbines might be placed in close proximity [16–18]. The interaction with the wake of upstream turbines generates additional unsteady load fluctuations on the downstream turbine [19], and the mean rotor power and thrust are also affected [20, 21]. However, this is a relatively unexplored area, and most research is on the effects of upstream wakes focuses on the yield of a downstream turbine [22, 23] and the optimisation of spacing within the array to optimise power extraction [24–26], rather than understanding unsteady loads arising from turbine-wake interaction. Load fluctuations are transmitted from the blades to the rest of the turbine making fatigue failures a key limit to reliability [27]. Furthermore, unsteady loads are reflected in large power output fluctuations [28], which result in over-dimensioned power-take-off systems [29] and in a lower operating rated power.

Carroll et al. [30] reported that, for wind turbines, blades, hub and gearbox have the highest repair time and repair cost, and that blades repairs require the highest number of technicians. However, the failure rate of wind turbine

blades that require major replacements is so low that blades are not likely to contribute significantly to overall Operation and Maintenance (O&M) costs. Conversely, blades of axial-flow tidal turbines represent a major contributor to the maintenance cost of the device [31]. Operating in seawater can cause a reduction of the blades design life of $1 - 3$ years [32], and fatigue failures of tidal turbines require divers to remove the blades, a dangerous process that further raises the O&M costs [33]. Kennedy et al. [32] showed that the blades of a tidal turbine equipped with a conventional pitch control system can have 10% thinner laminates than the blades of a stall-regulated turbine for the same fatigue design life. Advanced load mitigation strategies could allow manufactures to design blade with less conservative safety factors, with significant savings in the amount of material used, which would reduce considerably the production costs [34].

Given the harsh load conditions experienced by tidal turbines and the high maintenance cost, it is essential to understand how to mitigate fatigue loads to help manufacturers to design blades capable of withstanding a longer life, which will ultimately reduce the Levelised Cost Of Energy (LCOE) and enhance the competitiveness of tidal energy. I review the main strategies that have been investigated to alleviate blade loading, drawing from both wind and tidal industries. A passive load control mechanism is then proposed as a method of alleviating blade fatigue generated by unsteady flow. Its performances are investigated through numerical simulations and proof-of-concept experiments.

1.3 Load control systems

Load fluctuations are most commonly mitigated by actively varying the turbine speed or by actively pitching the blades [35]. Individual pitch control is typically the most advanced active control employed by commercial-scale tidal and wind turbines and it's capable of considerable reductions of the blade fatigue loads [36–39]. Unfortunately, the effectiveness of these control systems decreases with the size of the blade. With the scale-up to larger devices, the turbine diameter becomes closer to the size of the most energetic

turbulent eddies in the flow stream [40], and the increase in the blade flexibility leads to higher aeroelastic coupling [41]. The system dynamics changes and the blade experiences bending moments which may be too high to be sustained using conventional blade design [42]. Moreover, there is a trade off between the power that can be spent to actively control the rotor and the highest frequency that can be mitigated. From the results of Barlas and Lackner, Barlas et al. [43, 44], for example, pitch control is up to about 50 times slower than required to cancel up to the highest load fluctuations experienced by wind turbines. Therefore, different load-mitigating technologies have been explored.

1.3.1 Actively controlled trailing edge flaps

Fast-actuated flaps, like those used on aircraft wings, could mitigate higher frequency fluctuations [43–46]. Trailing edge flaps are indicated as the most promising device, with performances comparable or greater than individual pitch control [47, 48]. These devices allow for a local, distributed control action over the blade, they have lower weight and power requirements, and greater aerodynamic efficiency. Active control systems are preferred by the wind industry due to the higher control over unsteady flow changes.

Bernhammer et al. [49] reviewed the effects of a trailing edge flap applied to a wind turbine. A flap that covers about 10% of the chord and $5-30\%$ of the blade span is expected to reduce fatigue loads by $5.7-59\%$, depending on the type of controller, size and positioning of the flap, and harshness of the flow conditions, where strong turbulence and gusts correspond to poorer performance. Similar results are confirmed by other authors and are summarised in Table 1.2. The flap performs better when there are no time lags in the sensor or actuator systems [50], and loads are alleviated even when the frequency of the disturbances is of the order of the natural frequency of the model [51]. When applied to a turbine blade, the load alleviation performance of trailing edge flaps is lower compared to two-dimensional cases due to the vortex-downwash at the flap edges caused by strong gradients in the bound circulation in the span-wise direction [52]. A flap that covers a larger portion of the blade span minimises this effect and is thus considered

favourable. Although the performance on a turbine is lower than on a two-dimensional airfoil, hub, shaft, nacelle and tower also benefit from fatigue reduction [49, 53, 54]. Pitch control is also capable of mitigating deterministic 1P loads (i.e. occurring once per revolution), however, trailing edge flaps are much more effective at alleviating the loads due to stochastic disturbances like the wakes of upstream turbines [55]. Even better results are achieved when combining flaps with individual pitch control [56, 57].

All the studies found in the literature agree on the effectiveness of actively controlled trailing edge flaps to reduce fatigue loads. They focus on the optimisation of the flap size (chord-wise and span-wise), positioning along the blade [47, 58, 59], and different control strategies [60–64]. The use of active control systems for load mitigation is so well established that even wear and tear of the actuators is taken into account for cost considerations [65]. Overall, active trailing edge flaps, whether with a rigid or a compliant structure, are shown to be a technology enabler for rotor upscaling thanks to extreme and fatigue loads reduction [66, 67].

Authors	Test	Flap structure	Flap size	Disturbance	Load mitigation
Buhl et al. [68]	2D* aeroelastic simulation	flexible	10% chord	turbulence	normal force std dev −81%
Van Wingerden et al. [69]	3D* exp (non rotating)	flexible	50% chord, 12% span	sinusoidal	root strain 1p amplitude −90%
				turbulence	root strain 1p amplitude −37%, 3p −55%
Frederick et al. [70]	2D* exp	rigid	4% chord	vortex wake	lift RMS −79%
Castaignet et al. [71]	3D* exp (rotating)	rigid	13% chord, 5% span	environmental wind	root bending moment 1p amplitude −20%
Zhang et al. [72]	3D* aeroelastic simulation (rotating)	flexible	10% chord, 20% span	environmental wind	root bending moment RMS −35%

Table 1.2: Effectiveness of active trailing edge flaps for unsteady load mitigation. (*2D means two-dimensional, 3D means three-dimensional)

1.3.2 Passive trailing edge flaps

The cost of maintenance of both offshore wind and tidal turbines is a major driver compared to onshore wind [73]. Hence, reliability is paramount [74] and passive load control strategies would make simpler and more reliable systems. However, only a few results can be found about passive flaps even though it has been shown that they have similar gust-mitigating performance of controlled flaps [75].

Bottasso et al. [76] proposed a passive flap actuation mechanism where a mass is offset from the flap hinge such that if the blade accelerates in one direction the flap deflects in the same direction (Fig. 1.1). The concept was designed to mitigate vibrations and it reduced 1P, 2P and 3P loads over a wide range of rotor speeds and wind speeds, with virtually no reduction of power. The inertia-driven system might not be suited for tidal turbines because of the greater added mass on the flap and the need of a rigid hinge to couple the motion of the offset mass and the flap.

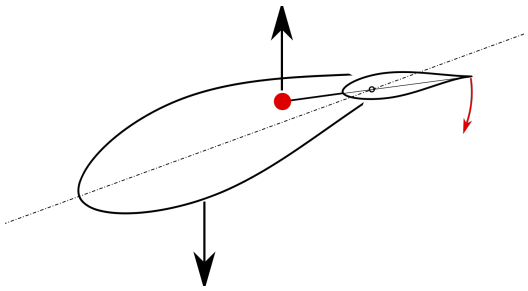

Figure 1.1: Schematic diagram of a passive flap actuation based on a (red) counterweight (Bottasso et al. [76]).

Cordes et al. [77] developed an airfoil that features a rigid flap and hinged leading edge (Fig. 1.2). The linkage system is such that both hinged surfaces move up or down together. The motion is balanced by a torsional spring. The idea is that the leading edge surface can sense the changes in pressure and command the cambering/decambering of the foil through the linkage system before the loads are affected. They showed that this "adaptive camber airfoil" is capable of alleviating up to 60% of the load fluctuations due to large scale turbulence, 20% of lift overshoots due to Mexican Hat gusts [78], and it can

effectively reduce the effects of dynamic stall thanks to the upward rotation of the leading edge which facilitates the disruption of intense leading edge vortices [79].

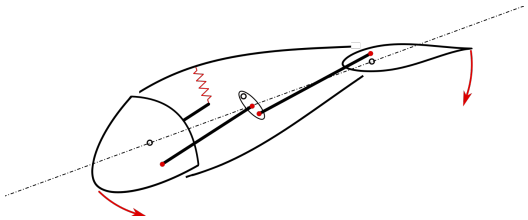

Figure 1.2: Schematic diagram of the adaptive camber airfoil (Cordes et al. [77]). The leading edge motion drives the deflection of the trailing edge.

These systems are smaller and therefore could have a faster response than a whole blade pitching system, but they still require complex linkage systems and bearings that are exposed to debris and biofouling, known to cause considerable drawbacks [80]. This additional complexities are seen by industry as posing a risk to the turbine reliability. Most tidal turbines feature individual pitch control, however, some tidal companies such as Nova Innovation, Nautricity and Schottel Hydro adopt fixed blade turbines to maximise reliability. Orbital Marine Power and SIMEC Atlantis Energy, which operate the largest rotors, only use collective pitch control, which cannot mitigate fast load fluctuations due to, for example, shear, turbulence, yaw misalignment, etc. Simpler, more reliable systems are thus needed. Blades with passively morphing trailing edge flaps are lightweight, have a quicker activation, no mechanical parts, and are less exposed to the environment, providing a better, more robust alternative than conventional flaps [81, 82].

1.4 Morphing blades background

Last year, blades with built-in chordwise flexibility were identified by the European Commission as one of the most promising concepts for reducing the costs of the blades and the downstream components of turbines [83]. A flexible trailing edge would provide the same performance of flaps, with fewer components and no actuation mechanisms. Building blades that passively

adapt to the flow conditions is not a new idea, and it dates back at least to 1978 [84], when the concept of aeroelastic tailoring was introduced.

The first example of adaptive blade was presented in 1978 by Cheney and Spierings [85] for wind turbines and it is shown in Fig. 1.3. Their blades featured a unidirectional composite spar which allowed for torsion at the root, where the pitch motion is caused by the motion of a pendulum connected to the blade. At rest, the pendulum lies outside of the rotation plane. As the turbine speed increases, the centrifugal moment drives the pendulum towards the rotor plane. Flapwise motions of the pendulum thus translate directly into increase of the pitch angle of the blade (i.e. twist to feather). The system worked as a passive pitch system to regulate the power at different wind speed, and it improved the self-starting capabilities of the turbine. Since the system is based on the anisotropic properties of composites, it is considered the forefather of aeroelastic tailoring.

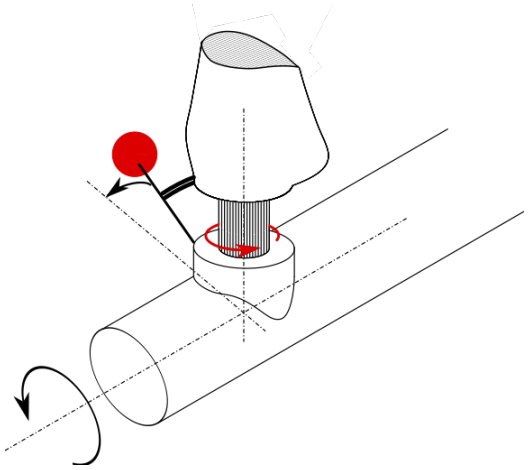

Figure 1.3: Schematic diagram of the first adaptive blade system (Cheney and Spierings [85]). When the blade speed increases due to a gust, the greater centrifugal force moves the pendulum mass (red circle) towards the rotor plane, thus increasing the blade pitch angle.

In 1981, Bottrell [86] developed a flexible rotor concept called "balanced-pitch rotor", where the blades of a two-bladed rotor shared the same spar which was held by two sets of bearings and by two linear springs which constrained the pitch motion. As the blades are connected, in the presence

of wind shear or cross wind, the blade experiencing higher loads pitches nose-down (i.e. twist to feather) and drives the lower blade into a nose-up motion, balancing the loads across the rotor and minimising cyclic torque fluctuations. The author did not provide any performance data. In 1988, Karaolis et al. [87, 88] introduced the idea of biased composite lay-ups to achieve twist coupling in response to blade bending or centrifugal loads. With increasing wind speed the blade would twist to stall, therefore regulating power generation. The concept was initially dismissed due to the difficulty of predicting power in post-stall regimes and manufacturing limitations [84], but it gained popularity from 1996 as a promising system to improve energy yield and torque startup [89]. In the same period, the Dutch Flexhat programme [90] investigated a system that uses a screw cylinder and a preloaded spring to harness the centrifugal loads to passively pitch the blade tip to feather for power control (Fig. 1.4). The concept was improved in 1998, when Joosse and Berg [91] proposed the "TenTorTube", where a composite tube replaced the screw cylinder and the spring, to twist in response to centrifugal loads caused by rotor speed changes.

A more recent example are the flexible blades designed by Cognet et al. [92], where the blade flexibility was optimised to improve efficiency and harvested power up to +35% for wind conditions typical of the North Sea, and extending the operating regime of the machine [93]. Several other designs have been tested over the years [94, 95], and it has been investigated also for tidal turbines [96, 97]. Although it was sometimes reported an improvement of the fatigue life of the blades thanks to the blade embedded flexibility [84, 98], the main focus has always been power control across the operational wind speed range of the turbine [99–101].

Passive bend-twist coupling is currently adopted by Schottel Hydro, whose 70 kW turbines are 6.3 m in diameter. On the other hand, the higher loads on SIMEC Atlantis Energy's MW-scale tidal turbines are incompatible with the flexibility required for passive twist. This mechanism primarily mitigates the unsteady load at the tip, which is the major contribution to the torque and thrust, but it does not prevent large flow separation occurring near the blade

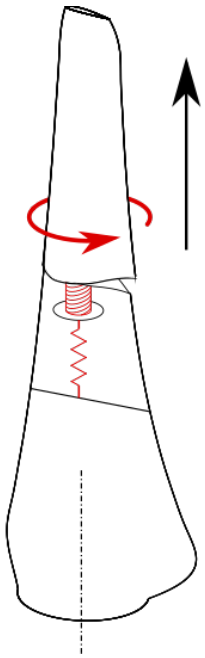

Figure 1.4: Schematic diagram of the passive blade tip (Kuik and Dekker [90]). Under higher speed, the centrifugal force pulls the blade tip outwards, and the screw cylinder twists it to feather.

root [8]. This results in less energy remaining available to the downstream turbines, and thus to lower efficiency for compacted arrays. Smaller devices are better suited for fatigue loads mitigation [43, 44].

1.5 Morphing blades for tidal turbines

To my knowledge, Tully and Viola [102] are the only ones who studied how to alleviate unsteady loads on tidal turbines using passive morphing blades for camber control. They compared the performance of two NACA 4415 airfoils, each with 0.15 m chord and 0.3 m span. The first airfoil was rigid and the other was flexible, and their stiffness differed by more than 3 orders of magnitude. The airfoils were tested at a nominal incidence of 10 deg (blockage ratio 4.3%) in a water flume at Reynolds 75000, 3% turbulence, and opposing waves at 9 Hz that generated fluctuations of the angle of attack of ±12 deg. By comparing the loads measured with a load cell, they found that a passively morphing blade is capable of reducing the angle of attack fluctu-

ations and thus mitigating the amplitude of the fluctuations of the normal force by more than 30%. Moreover, the morphing foil can reduce separation and drag at high angles of attack, increasing the lift to drag ratio by more than 25%. Their pioneering study showed the potential of passively morphing blades for unsteady load mitigation but it also highlighted some issues. Both foils were tested in one flow condition and it is not known how the foil performs in different conditions. The foil material determined the flexibility which could not be tuned, or optimised for a different environment, without replacing the foil altogether. Moreover, the experiments investigated a two-dimensional flow field which differs significantly from the three-dimensional flow field generated by a rotating turbine [9].

1.6 Summary of previous work and motivation

Unsteady load mitigation is a key feature to improve tidal turbines and to enable their deployment on a wide commercial scale. Conventional load control systems are inadequate to alleviate the high frequency loads arising in a tidal environment, but at present there is no proven alternative. The wind industry suggests that the most promising option are trailing edge flaps to provide lightweight, fast-acting load control, and the need for higher reliability prompts the use of passive, flexible materials rather than actuated, rigid control surfaces. In this work, a blade featuring a flexible trailing edge for load control purposes will be referred to as "morphing blade". However, I could find only one study (Tully and Viola [102]) that analysed the effectiveness of passively morphing blades to alleviate unsteady loads on tidal turbines. Despite the encouraging results, the study was limited to one load condition, and it did not provide an explanation of the governing physics. Hence, I decided to investigate the underlying principles of load alleviation through passive blade morphing and to optimise the system under different load conditions.

1.7 Scope of the PhD

I aim to answer the following research questions:

(1) What are the physical phenomena that underlie unsteady load alleviation by morphing blades?

(2) Which are the key factors of a practical implementation that can decrease their effectiveness?

(3) How does the system perform under different load conditions?

To address these questions, I developed a low-order model of a morphing blade, identified the parameters that govern the system performance, and performed proof-of-concept experiments using a 1:15 scale model turbine in the wave tank at FloWave Ocean Energy Research Facility [103]. The code was also used to inform the design of the tank-scale model, for the sizing of the morphing mechanism.

The physical mechanism underlying load alleviation by morphing blades is first introduced for the case of a turbine operating in shear flow, where the load fluctuations are caused by the blade rotating through a steady, non-uniform flow field. Devoid of the complexity of real tidal currents and unsteady flow phenomena, this scenario can be reliably described by the proposed low-order model. The simplicity of the model allows to investigate the first-order phenomena that determine load fluctuations and the effectiveness of morphing blades, which are identified in Chapter 3 as a correction of the blade effective angle of attack in response to fluctuations of the onset flow velocity and the resulting angle of attack and load variations. Once the fundamentals of the morphing blade concept have been established and the reader has gained confidence in the system performance, more realistic scenarios are presented, to gain an indication of the capabilities of morphing blades in more complex, unsteady flows, despite the limits of the model that neglects higher-order phenomena. This work focuses on the underlying physical mechanism of load alleviation by morphing blades and it aims to pave the way for future designs.

1.8 Overview of the thesis

The rest of the paper is organised as follows. In chapter 2, I review different numerical models found in the literature, to justify the method that I chose to model morphing blades for tidal turbines. In chapter 3, I present the morphing blade low-order model. In chapter 4, I describe the model inputs and its validation respectively. Chapter 5 shows the numerical analysis of the morphing blade model, how I optimised its load alleviation capabilities, a parametric study of the effect of the morphing blade properties on the system performance, and the potential load mitigation of morphing blades on a turbine subjected to different load conditions. In chapter 6, I describe the tank-scale model and the experimental equipment. In Chapter 7, I show the results from the experiments, I discuss their validity and their limits. In the conclusive Chapter 8, I summarise my findings.

2

Literature on morphing blade models

To investigate the effects of morphing blades on tidal turbines, I develop a low-order model. The main challenge is to integrate a morphing blade model withing a tidal turbine model to obtain a simple, yet accurate, representation of the underlying physics.

2.1 Turbine modelling

A simple model for tidal turbines is blade element momentum theory (BEMT) [104]. It represents the effect of the whole rotor on the incoming flow by applying axial and tangential induction factors, and it computes the loads from the aerodynamics of the different blade sections. It considers only the main physics and neglects higher order phenomena. Moreover, it has a high degree of modularity. If needed, non-linear phenomena like dynamic stall and returning wake can also be included (see for instance [7, 9]). On the other hand of the spectrum, we find blade-resolved CFD models. These models give the most accurate representation of the turbine and allow to capture the finest details of the surrounding flow [105–107]. However, they are extremely expensive to run and they are suited for detailed studies rather than repeated runs for parametric investigations. To overcome the simplicity of BEMT and the cost of blade-resolved CFD, two methods have been suggested. The simplest is a uniform actuator disk model embedded in either Reynolds-averaged Navier-Stokes simulations (RANS) or large eddy simulation (LES) as a momentum sink [108, 109]. Next is the actuator line method [110]. This unsteady method is based on BEMT with

a Navier-Stokes description of the flow field. It treats a blade as a line of elements representing the blade profiles with their lift and drag coefficients. The inflow is sampled at the quarter-chord of each element to compute onset velocity and angle of attack. To model an entire wind farm, where the interaction with the wakes of upstream turbines is paramount, the actuator line method coupled to unsteady RANS or LES has become the standard [111, 112]. Instead, where the relevant phenomena happen close to the blade, this method is more expensive and no better than BEMT. Additional methods have been developed to investigate turbines, like unsteady vortex lattice methods [113, 114] and the asymptotic acceleration potential method [115]. In vortex lattice methods the blade is discretised into panels with associated vortex rings that provide the circulation. At each time step, the circulation of the trailing edge panel is shed into the wake, and the non-penetration condition is imposed on each panel at a collocation point. The wake vorticity offers all the information needed to analyse the problem physics, however, it can be computationally expensive and it tends to diverge due to vortex singularities. The asymptotic acceleration potential method solves the Poisson equation for pressure, assuming small perturbation of the mean flow. It is fast to run but the flow field is modelled using linear potential flow theory which does not suit well modelling of highly unsteady flow conditions, thus it doesn't offer significant advantages over BEMT.

BEMT is the most established industrial design tool which has been implemented in commercial softwares like Tidal Bladed (GL Garrad Hassan) [116] and other advanced aeroelastic models like AeroDyn (NREL) [117], DU_SWAP (Delft University) [60], HAWC2 (Denmark Technical University) [62], and Flex5 (Denmark Technical University) [118]. Advanced methods allow to better capture details of the underlying physics, but the added computational cost and low versatility makes them less attractive than BEMT to model tidal turbines. Knowing that it will be coupled with a second model to represent a morphing blade, a simple, well established tool like BEMT is my best option.

2.2 Morphing blade modelling

In its broadest sense, a morphing blade is a wing or an airfoil that can change camber, by virtue of a flexible trailing edge, a rigid flap, or any mechanical reconfiguration of the wing shape. Several numerical models have been proposed to represent morphing blades from an aerodynamic point of view.

2.2.1 Early models from aeronautics

In 1935, Theodorsen [119] formulated one of the earliest models of a flat plate with a rigid trailing edge flap, to investigate the mechanism of flutter on aircrafts. His model is two-dimensional, it is based on potential flow, and the plate is obtained by conformal transformation of a cylinder whose boundary is represented by a distribution of sources and sinks of equal strength, whereas the wake is represented by a continuous vortex sheet. Despite the complexity of the mathematical model, Theodorsen offered a set of equations to compute in closed form the loads due to harmonic motions of the plate, of the flap, and harmonic fluctuations of the angle of attack. Theodorsen's unsteady aerodynamics model is still widely used thanks to its simplicity, it compares very well with more advanced techniques like vortex lattice methods [120], and it provides reliable results as long as the assumptions of thin-airfoil theory are met (i.e. small mean angle of attack, attached flow) [121].

Using a different conformal transformation, in 1955, Keune [122] also modelled a flat plate with a deflected trailing edge. However, the model considered only static configurations.

During the 70s, with the rapid growth of civil and commercial aviation, trailing edge flaps and leading edge slats received lots of attention and a number of potential flow models were developed to predict their performance. Williams [123] (1971) developed a potential flow model for two adjacent lifting airfoils. The method considers two circles which are transformed into airfoils via conformal transformations. Using the circle theorem [124], in the presence of a streaming flow represented by a complex potential, the

circle boundary is obtained by superimposing the complex potential of a doublet, which represents the image system that ensures the non-penetration condition. By adding a second circle representing the flap, its boundary is defined by two image systems: one for the streaming flow and one for the doublet representing the first airfoil. The process has to be repeated on the first airfoil to consider the image systems for the flap, and so on. Williams proved that each new set of images has decreasing strength, each series of doublets converges, and the loop can be stopped after a certain number of iterations. However, the process has to be repeated when the lifting vortex is added to each circle to provide circulation. Although this method allows an exact mathematical representation of a flapped airfoil, it is too complex and expensive to be implemented in a BEMT code. Ives [125] (1976), building on Garrick's work on biplanes [126], presented a different strategy where the incompressible flow between two concentric circles is used to calculate the flow around an airfoil with a trailing edge flap. The method enables rapid and accurate calculations, but the mapping of each airfoil to a circle requires four different transformation, which would prove inefficient within a BEMT code. In 1979, Halsey [127] presented a generalised procedure for potential flow analysis of multi-element airfoil using conformal mapping. The method allows to model any number of lifting surface by mapping of each airfoil into a circle. Once again, the method requires to perform multiple transformations on each airfoil. Moreover, Halsey highlighted how the mapping of one element distorts nearby elements depending on how close they lie, which makes it suitable only for configurations where the flap is detached from the airfoil.

In the same period, Katz and Weihs [128, 129] developed a potential flow model to estimate the propulsive force of flexible foil representing a fish. They considered a flat, flexible plate, and they compute the deformation using a cantilever beam model. Their method computes the loads from the vortex wake, which grows over time and makes the code computationally expensive.

In 1994, Leishmann [130, 131] expanded the work on flaps and unsteady aerodynamics of Theodorsen [119]. As the original model worked only for harmonic motions, Leishmann coupled it with Wagner's indicial function

concept [132] to study arbitrary motions of the flap in compressible and incompressible flows, for helicopter applications. In 1995, Narkiewitz [133, 134] developed a similar method to account for arbitrary motions of the airfoil and of the flap. The airfoil bound circulation is calculated as the sum of a series where each contribution is associated to a Fourier component of the onset velocity and computed using Theodorsen's model.

2.2.2 Morphing blades models for wind turbines

In 2010, Gaunaa [135] presented an unsteady model of thin variable geometry airfoils for wind turbine applications. The model is an extension of Theodorsen's work, where the superposition of chord-wise deflection mode shapes allows to represent any deflection of the camber line, as long as it is small, instead of just a rigid flap as in the original formulation. It was later improved to include dynamic stall modelling [136]. In first approximation, the camber represents the curvature of the airfoil and it affects its angle of zero lift, whereas local deformations are higher-order phenomena which are relevant for the interactions they have with local flow features. Since the purpose of my study is to capture first order phenomena that define the mechanism of load alleviation by morphing blades, higher-order phenomena like local foil deformations are here neglected. Therefore, Gaunaa's model has higher complexity, thus higher computational cost, whilst providing the same insight on first-order phenomena as Theodorsen's model.

2.2.3 High-fidelity models

To my knowledge, no other low-order models have been developed to study morphing blades for wind or tidal turbines. CFD models have also been proposed to investigate morphing trailing edges both for wind turbine applications [63, 137] and flapping foils applications [138, 139]. Although CFD provides detailed results, embedding a two-dimensional (2D) CFD model within a BEMT solver is meaningless. The accuracy of CFD results strongly depends on the accuracy of the inputs which a BEMT code cannot provide, resulting in a time-consuming tool and no better results.

2.2.4 Flexible flapping foils

Following the work of Katz and Weihs [128, 129] more models have been proposed to investigate the interaction of passive flexible foils with the surrounding fluid propulsion or power generation by flapping motion. Michelin and Llewellyn Smith [140] developed a potential flow model where the wing is represented by an elastic sheet clamped at the leading edge and heaved harmonically. The surrounding flow is determined by a wake of vortices which are shed once their circulation reaches a limit value, and that enforce the Kutta condition at the trailing edge. The flexible sheet is modelled as a Euler-Bernoulli beam, and it deforms in a non-linear fashion due to the local pressure resulting from the induced velocities. Similarly, Alben et al. [141–143] studied flag-flapping instabilities on a flexible sheet using a potential model where the relevant flow features are determined by a streak of shed vortices. They also considered the non-linear contribution of viscous boundary layer drag, an important component of the force balance in the horizontal direction. Other models have been proposed, including non-linear Euler-Bernoulli beam kinematics coupled with 2D unsteady panel method [144], a distributed flexibility plate model coupled to immersed boundary layer method [145], immersed boundary-lattice Boltzmann method applied to an airfoil with thin, flexible trailing edge [146, 147], and viscous vortex particle method coupled to the dynamics of two rigid bodies connected by a torsional spring [148]. In all cases, the accurate modelling of the vortices in the wake was paramount, as the position, speed and intensity of each vortex determines the airfoil performance at extracting energy from the flow or propelling itself [149, 150]. The deformation of the foil is also described using accurate, non-linear, thus complex models.

2.2.5 Revisiting conventional flaps and the impulse method

The work of Wu [150] on vortex impulse was adopted in recent years to investigate non-linear unsteady aerodynamics [151, 152], wing-gust encounters [153], and how to alleviate the gust generated loads using trailing edge flaps [154]). Similarly to Theodorsen's theory, loads are generated by circulatory

and non-circulatory phenomena. Both contributions can be computed from the knowledge of the "free" vorticity in the flow field (i.e. detached from the wing), the bound vorticity, and their rate of change. When comparing the vortex impulse method to Theodorsen's model, it has been found that they both accurately predict experimental results [154]. As opposed to Theodorsen's model, the vortex impulse method does not rely on the hypothesis of attached flow, and it allows to compute different load contributions even in highly separated flow conditions. However, it requires the knowledge of the vorticity field at all times, which has to be provided either by experimental visualisations or by computing it using, for instance, a discrete vortex method. Moreover, even if it violates its underlying assumptions, Theodorsen's model has shown considerable resilience in its lift prediction capabilities in separated flow conditions [155, 156].

2.3 Overview of morphing blade model for tidal turbines

My objective is to develop a low-order model to identify the first order phenomena that underlie load alleviation by morphing blades on tidal turbine blades. Although several models have been developed for similar purposes, I found that most of them are excessively accurate and resource demanding for the scope of my study. BEMT is a low-order, low-cost model whose speed would be impaired by coupling it with an expensive morphing blade model. I believe Theodorsen's model is the most suitable to represent morphing blades. The model is the benchmark for unsteady aerodynamics and is still widely used in its original form [157, 158] or with small adjustments [7, 8, 135, 159]. Its strengths are that it provides closed form equations for the unsteady loads on an airfoil which makes it ideal to couple with a BEMT model for quick computations, it includes wake effects with no need for time-consuming wake models, and its modularity allows to include additional models to refine the level of accuracy and to widen its applicability. Additionally, although the model assumes harmonic disturbances, it is linear, allowing for superposition of effects to represent complex flow conditions typ-

ical of tidal environments. Details of the model are explained in Chapter 3, and its capabilities are shown and validated in Chapter 4.

3

Numerical method: how to model a morphing blade

I present the numerical methodology for a turbine subjected to flow fluctuations caused by a modelled shear flow. Nonetheless, the method can be readily generalised for flow fluctuations induced by other sources, like turbulence, waves and wakes, or for real flow conditions, as described in Section 5.5. The specific flow conditions, the turbine properties, and the spatial and temporal discretizations are introduced in Section 4.1.

3.1 Rigid Blade Model

I consider a 3 blades tidal turbine with a rotor diameter of 18 m (hub diameter 2.5 m, blade tip at $R = 9$ m from the rotor axis, blade length 7.75 m) operating in a sheared velocity profile, at the constant, optimal tip speed ratio of 4.5. The turbine hub is at 20 m from the seabed, the mean flow velocity at the hub is $U_{\text{hub}} = 2$ m s^{-1}, and the velocity profile varies with a 1/7 power law. While in reality the interaction of the turbine with freestream fluctuations is a complex phenomenon which includes the response of the turbine control system with its inherent delays, complex unsteady hydrodynamic phenomena like dynamic stall at the blade root causing large load swings, elastic bending and twisting of the blades, and fluctuating spanwise flow, in first approximation the effect of flow fluctuations can be described by fluctuations of the inflow speed and subsequent angle of attack and load variations at each blade section. Each blade experiences periodic onset flow,

such that the inflow speed and the angle of attack are maximum for each section when the blade is pointing upwards, and minimum when pointing downwards. I employ Blade Element Momentum Theory (BEMT) to compute the local inflow conditions [104]. BEMT was developed for the analysis of wind turbines and it doesn't account for the flow confinement in a tidal channel and the consequent blockage caused by a turbine. The water surface is deformed, and a static pressure difference builds across the flow passage causing power extraction efficiencies greater than the Betz limit [25, 160]. The effects are more pronounced for compacted arrays. Although it's been shown that the blade root bending moment increases with flow confinement, despite the availability of models to account for the phenomenon [161], I consider it a second order phenomenon and I neglect it for the purpose of this investigation. My focus is not to predict as accurately as possible the loads and the power extracted but to provide compelling evidence that a morphing blade can reduce the load fluctuations for any load condition.

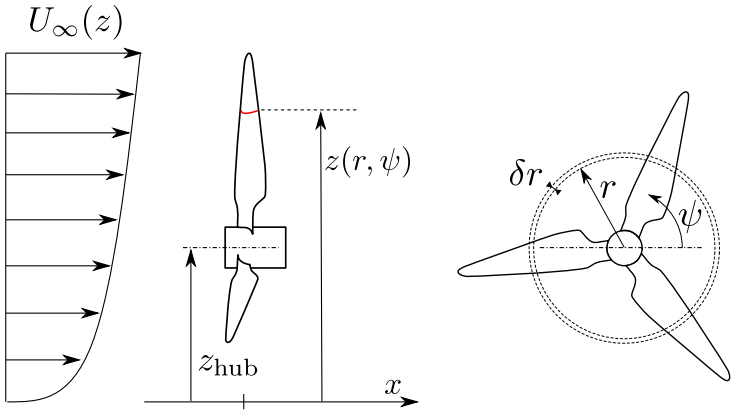

Figure 3.1: Schematic diagram of a tidal turbine coordinate systems. On the left, the side view shows the interaction of the turbine with a shear flow. On the right, front view of the turbine.

BEMT computes the change in flow momentum for every annulus of radius r and thickness δr as shown in Fig. 3.1. Radial flow is neglected. The axial velocity experiences vertical variations due to the shearing caused by the boundary effects of the seabed. The velocity profile of the free stream velocity is described using a 1/7 power law and is given by

$$U_\infty(z) = U_{\text{hub}} \left(\frac{z}{z_{\text{hub}}} \right)^{\frac{1}{7}}, \tag{3.1}$$

where U_{hub} is the velocity at the hub height z_{hub} from the seabed, and z is the vertical coordinate. The 1/7 power law is commonly used to describe the velocity profile across a turbulent boundary layer (Schlichting and Gersten [162]). It is often applied to tidal flow in coastal regions [163], and its use is recommended by the UK Health and Safety Executive [164] to model velocity profiles in coastal regions around the UK.

The turbine's power extraction mechanism is manifested by the fluid loads acting on the blades in the form of a thrust force in the direction of the incoming flow and torque that pushes the blades in the rotating motion. On the other hand, the reaction of the blades on the fluid flow is such that the thrust slows down the free stream axial flow and the torque induces a rotating motion in the wake which is opposite to that of the turbine. These two effects are considered by applying an axial induction factor a and a tangential induction factor a' to the incoming flow. The axial (U_x) and tangential (U_ψ) components of the flow speed relative to the blade sections are depicted in Fig. 3.2 and they are computed following the approach of Burton et al. [104] as

$$\begin{aligned} U_x &= U_\infty - a\overline{U}_\infty, \\ U_\psi &= \omega r(1 + a'), \end{aligned} \tag{3.2}$$

where ω is the turbine rotational speed and r is the section position along the blade. $\overline{U}_\infty$ is the average upstream axial velocity seen by a blade rotating in a shear flow and is defined as

$$\overline{U}_\infty = \frac{1}{2\pi} \int_0^{2\pi} U_\infty \, \mathrm{d}\, \psi, \tag{3.3}$$

where $U_\infty = U_\infty(z)$ and z, in turns, depends on the polar coordinate ψ

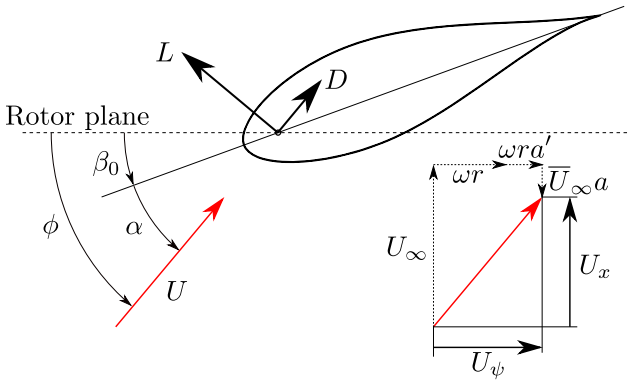

Figure 3.2: Flow velocities and forces acting on a 2D blade section.

(Fig. 3.1).

From the vectors shown in Fig. 3.2, the flow relative to the blade is obtained as

$$\begin{aligned} U &= \sqrt{U_x^2 + U_\psi^2}, \\ \phi &= \tan^{-1}\left(\frac{U_x}{U_\psi}\right), \end{aligned} \tag{3.4}$$

where U is the magnitude of the relative flow speed experienced by the blade section and ϕ is the inflow angle (Fig. 3.2). Let β_0 be the twist angle of a blade section, the angle of attack is

$$\alpha = \phi - \beta_0. \tag{3.5}$$

Aerodynamic theory [165], shows that the lift L and the drag D are approximately proportional to the dynamic pressure ($\rho_w U^2/2$) and the chord of the blade,

$$\begin{aligned} L &= \frac{1}{2}\rho_w U^2 c C_L, \\ D &= \frac{1}{2}\rho_w U^2 c C_D, \end{aligned} \tag{3.6}$$

where ρ_w is the water density, c is the foil's chord, C_L and C_D are constant and known as lift and drag coefficients, respectively.

The pressure jump across the rotor is equalised towards the blade tip due to tip vortex, and the effect is accounted by a tip loss correction factor. Prandtl's tip loss enables a more realistic modelling of the flow physics than a purely two-dimensional formulation [104]. Studies have shown that loads can be predicted with greater accuracy when considering how the spanwise flow changes near the tip [166, 167] which are not accounted by Prandtl's method, or by recalibrating the tip correction factor using data from blade resolved simulations [168]. However, these corrections are typically used for high fidelity simulations, and for the sake of simplicity I did not implement them. I compute the tip loss factor following Burton et al. [104] as

$$\hat{F} = \frac{2}{\pi} \cos^{-1}(e^{-f}), \tag{3.7}$$

where

$$f = \frac{N_b}{2} \frac{1-r}{r \sin \phi}, \tag{3.8}$$

and N_b is the number of blades.

The BEMT algorithm evaluates the induction factors with an iterative procedure that uses the mean loads acting on each section. I define the mean inflow conditions as

$$\begin{aligned} \overline{U} &= \sqrt{\overline{U}_x^2 + U_\psi^2}, \\ \overline{\phi} &= \operatorname{atan}\left(\frac{\overline{U}_x}{U_\psi}\right), \end{aligned} \tag{3.9}$$

where $\overline{U}_x = \overline{U}_\infty(1-a)$. The average angle of attack experienced by each section is

$$\overline{\alpha} = \overline{\phi} - \beta_0. \tag{3.10}$$

The mean loads are computed from Eq. 3.6 for $U = \overline{U}$. Coefficients $C_L(\overline{\alpha})$ and $C_D(\overline{\alpha})$ are initially evaluated with $a = {}^1/_3$ and $a' = 0$ for each section. The resulting lift and drag are then used to update the values of the induction factors

$$\begin{aligned} a &= \left(\frac{4\pi r \hat{F} \sin \overline{\phi}^2}{N_b c (C_L \cos \overline{\phi} + C_D \sin \overline{\phi})} + 1 \right)^{-1}, \\ a' &= \left(\frac{4\pi r \hat{F} \sin \overline{\phi} \cos \overline{\phi}}{N_b c (C_L \sin \overline{\phi} - C_D \cos \overline{\phi})} - 1 \right)^{-1}. \end{aligned} \tag{3.11}$$

The procedure is repeated until a, a', C_L and C_D converge. When the induction factor a is greater than 0.4, BEMT does not provide reliable data [104, 169]. This happens as a heavily loaded rotor becomes more impervious to the flow, forcing separation at the edge of the rotor. The high static pressure on the upstream side and the low pressure zone behind the rotor due to separated flow further increase the static pressure jump across the rotor and thus the thrust [104]. A first empirical correction to account for this effect was presented by Glauert [170], but I used the empirical formula developed by Buhl [171], which provides better results when a tip loss correction is employed [169].

The performance of the turbine is evaluated in terms of the non-dimensional power and thrust coefficients. For a blade section, they are respectively defined as

$$\begin{aligned} C_P^{2\mathrm{D}} &= \frac{P^{2\mathrm{D}}}{\frac{1}{2}\rho_w U_{\mathrm{hub}}^3 A^{2\mathrm{D}}}, \\ C_T^{2\mathrm{D}} &= \frac{T^{2\mathrm{D}}}{\frac{1}{2}\rho_w U_{\mathrm{hub}}^2 A^{2\mathrm{D}}}, \end{aligned} \tag{3.12}$$

where $A^{2D} = 2\pi r$ is the perimeter swept by the blade section at spanwise position r, and the thrust T^{2D} and the power P^{2D} are

$$\begin{aligned} T^{2D} &= L\cos\phi + D\sin\phi, \\ P^{2D} &= \omega r\big(L\sin\phi - D\cos\phi\big). \end{aligned} \tag{3.13}$$

For a turbine's blade, these coefficients are computed respectively as

$$\begin{aligned} C_P &= \frac{P}{\frac{1}{2}\rho_w U_{\text{hub}}^3 A}, \\ C_T &= \frac{T}{\frac{1}{2}\rho_w U_{\text{hub}}^2 A}, \end{aligned} \tag{3.14}$$

where $A = \pi R^2$ is the area swept by the turbine, $T = \sum_i T_i^{2D}\delta r_i$ and $P = \sum_i P_i^{2D}\delta r_i$, for $i = 1...N$, where δr_i is the thickness of the section and is chosen sufficiently small to ensure the desired accuracy.

3.2 Morphing Blade Model

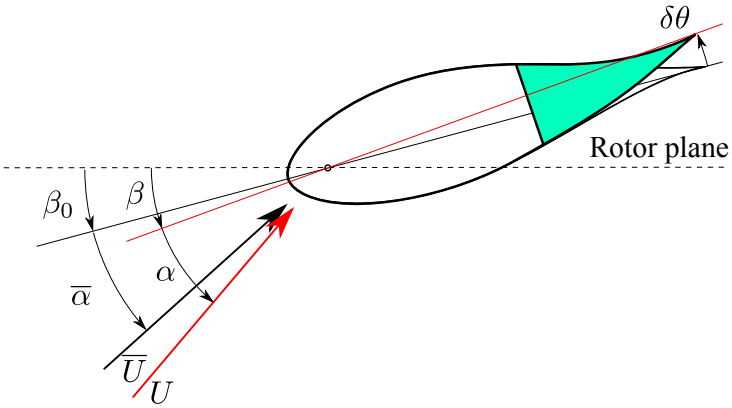

Figure 3.3: Morphing blade concept. Part of the blade can bend to mitigate inflow fluctuations.

The blade can bend its trailing edge to mitigate the changes in the flow

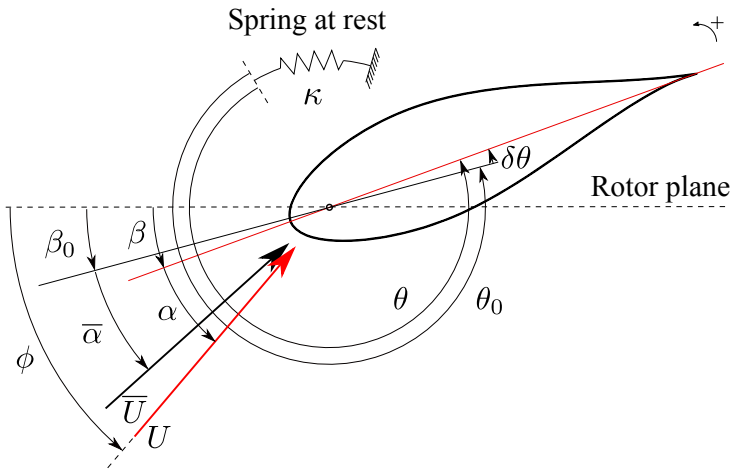

Figure 3.4: Morphing blade model. The flexibility is modelled by a torsional spring.

incidence, thus alleviating the load fluctuations. Let's assume that the loads on a blade section result in the elastic deformation of the foil as shown in Fig. 3.3. In first approximation, such geometric variation changes the effective angle of attack of the original foil. Therefore, the shape deformation is analogous to the pitch rotation of a rigid foil, and its flexibility can be modelled by a torsional spring with constant properties that controls the pitching motion of the blade (Fig. 3.4). The angular position of the blade is thus determined by the balance of the moments acting along the pitch axis.

The analysis is carried out for two different scenarios. Firstly, I consider a blade where there is no interaction between the sections such that each section moves independently from the others (Fig. 3.5a). This condition is representative, for example, of a blade made of a flexible material with a very low shear modulus, such that the shear stresses between the sections are negligible. The blade flexibility is represented by a torsional spring for each section, and the deflection of each section is determined by the local flow conditions. This model is described using a 2D analysis in Section 3.3, and it is optimised for each section of the blade, to allow the same mean load as the rigid foil and to minimise the fluctuations.

Secondly, I consider a blade where all sections experience the same de-

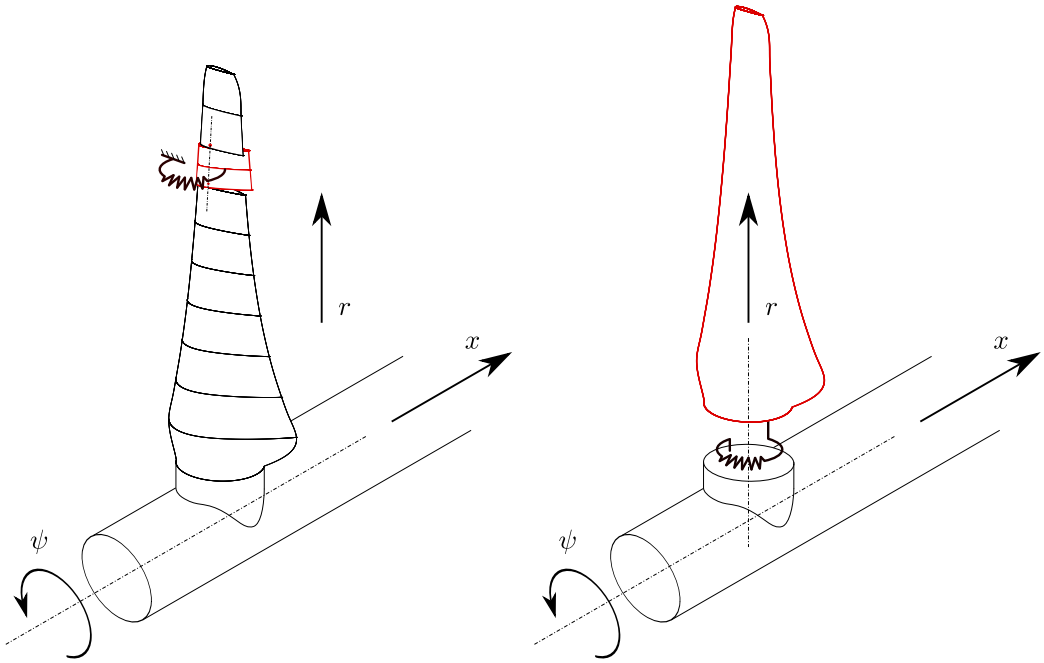

(a) Each section moves independently. **(b)** All the sections deflect together.

Figure 3.5: Morphing blade models.

flection along the span (Fig. 3.5b). As opposed to the previous scenario, this model could represent a blade material with a very high shear modulus. Therefore, the stresses caused by the external loads are efficiently redistributed along the blade such that each section deforms by the same amount. The blade deflection is thus seen as a rigid rotation with the flexibility concentrated at the root of the blade. This flexible connection is modelled with a torsional spring placed at the root that adds a variable pitch angle $\delta\theta$ to the rigid blade twist angle β_0. This condition is presented in Section 3.4, where the entire blade is considered, and the spring's parameters are optimised to minimise the fluctuations in the root bending moment without reducing the average power extracted. In Section 3.5, I extend such model to include the dynamics of the blade and the unsteadiness of the flow, to check the robustness of the optimal system when the blade dynamics are considered, and to investigate the effect of the blade inertia, the unsteady hydrodynamics and the blade mechanical damping on the performance of the morphing blade.

3.3 Quasi-steady Analysis of a Morphing Foil

I assume that each section can move independently from the others (Fig. 3.5a), such that every blade section can be optimised separately. The section angular position is determined by balancing the moments acting along its pitch axis. There are two moments that compete to determine the angular position of a blade section: the reaction of the spring

$$M_{\mathrm{s}}^{\mathrm{2D}} = -\kappa^{\mathrm{2D}}\theta, \tag{3.15}$$

where θ is the spring strain and κ^{2D} is the spring stiffness of a 2D section, and the hydrostatic pitching moment

$$M_{\mathrm{qs}}^{\mathrm{2D}} = \frac{1}{2}\rho_w U^2 c^2 C_M(\alpha). \tag{3.16}$$

The blade pitches around the point at the chordwise coordinate $\hat{x}_A = 0.1c$ from the leading edge of each section. Although the position of pitch axis seems practically not feasible due to the minimal space left near the leading edge to install a pitching mechanism, I will show in Chapter 6 that only minimal changes at the blade root are needed to realise the system. Moreover, the model developed in this work is representative of a morphing blade capabilities without claiming to be how a morphing blade should be practically realised. In fact, a morphing blade is envisioned as a continuously deforming surface with no discontinuities and no need for a physical pitch axis within the blade. The moment coefficient C_M is obtained from the quarter-chord moment coefficient $C_{M_{1/4}}$ by adding the moment contributions of lift and drag with respect to the pitch axis position $\hat{x}_A$, and is computed as

$$C_M(\alpha) = -C_{M_{1/4}} - \left(\frac{1}{2} + \frac{d}{b}\right)\frac{1}{2}\left[C_L\cos(\alpha) + C_D\sin(\alpha)\right], \tag{3.17}$$

where the location of the pitch axis is indicated with d (following Theodorsen's notation [119]), such that the distance of the pitch axis from the mid-chord is $d = -0.8b$, where $b = {}^{c}/_{2}$. C_M is positive in the clockwise

direction according to the sign convention in Fig. 3.4.

Since the passively controlled system works around the average flow condition for the rigid turbine (i.e. $\alpha(t) \approx \overline{\alpha}$), the hydrostatic pitching moment is linearised as

$$C_M(\alpha) = C_{M,0} + C_{M,\alpha}\alpha, \tag{3.18}$$

where $C_{M,0}$ and $C_{M,\alpha}$ are the best fitting linear regression coefficients of Eq. 3.17 over a 6 deg range of angle of attacks (i.e. $\alpha \in [\overline{\alpha} - 3\,\text{deg}\,,\, \overline{\alpha} + 3\,\text{deg}]$). Equation 3.16 is thus rewritten as

$$M_{\text{qs}}^{\text{2D}} = \frac{1}{2}\rho_w U^2 c^2 \big[C_{M,\alpha}\alpha + C_{M,0}\big]. \tag{3.19}$$

The quasi-steady equations for the foil in Fig. 3.4 are

$$\begin{cases} M_{\text{s}}^{\text{2D}} + M_{\text{qs}}^{\text{2D}} = 0 & \text{(a)} \\ \phi(t) = \beta(t) + \alpha(t) & \text{(b)} \\ \beta(t) = \beta_0 + \delta\theta(t) & \text{(c)} \end{cases} \tag{3.20}$$

where β is the blade pitch angle and $\delta\theta(t) = \theta(t) - \theta_0$.

The optimisation problem consists in finding the morphing blade that minimises the flapwise bending moment fluctuations on the blade over its revolution, with the requirement that the mean power extracted from the flow is the same as for the rigid turbine. For a 2D foil, the condition on the average power is restricted to the power generated by a single section of the blade and I attempt to minimise the fluctuations of the thrust acting on the section ΔC_T^{2D}, as it ultimately contributes to the fluctuations of the flapwise bending moment. Hence, in 2D the optimisation problem is

$$\begin{aligned} \min_{\kappa^{2\mathrm{D}}} \hat{J}(\kappa^{2\mathrm{D}}) &= \Delta C_T^{2\mathrm{D}} \\ \text{s.t.} \quad & \frac{\partial \overline{C}_P^{2\mathrm{D}}}{\partial \kappa^{2\mathrm{D}}} = 0, \end{aligned} \tag{3.21}$$

where

$$\overline{C}_P^{2\mathrm{D}} = \frac{1}{2\pi} \int_0^{2\pi} C_P^{2\mathrm{D}} \, \mathrm{d}\, \psi. \tag{3.22}$$

The problem is solved using an exhaustive search algorithm.

I approximate the average power extracted with the power generated by average flow conditions, namely $\overline{C}_P \approx C_P\left(\overline{\alpha}, \overline{U}\right)$. The average flow conditions $\alpha(t) = \overline{\alpha}$ and $U(t) = \overline{U}$, thus constant power generation, are achieved for a constant pitch angle $\beta(t) = \beta_0$. The requirement, $\beta(t) = \beta_0$, is satisfied with a spring extended by $\theta(t) = \theta_0$ where

$$\theta_0 = \frac{1}{2}\rho_w \overline{U}^2 c^2 \left(\frac{C_{M,\alpha}\overline{\alpha} + C_{M,0}}{\kappa^{2\mathrm{D}}} \right). \tag{3.23}$$

θ_0 will be referred to as the preload of the spring. The angle of attack is evaluated from the Eq. 3.20a where the expression for θ is obtained by combining Eq. 3.20c with $\delta\theta = \theta - \theta_0$. The expression for α is then rearranged to

$$\alpha(t) = \frac{\kappa^{2\mathrm{D}}\left(\phi(t) - \beta_0 + \theta_0\right) - \frac{1}{2}\rho_w c^2 U^2 C_{\mathrm{M},0}}{\kappa^{2\mathrm{D}} + \frac{1}{2}\rho_w c^2 U^2 C_{\mathrm{M},\alpha}}. \tag{3.24}$$

It's noted that the equation for α is consistent with the definition of the angle of attack for a fixed foil, in fact

$$\lim_{\kappa^{2\mathrm{D}} \to \infty} \alpha = \phi - \beta_0. \tag{3.25}$$

The spring deformation θ is evaluated by substituting Eq. 3.20c in Eq. 3.20b, such that

$$\theta(t) = \phi(t) - \alpha(t) - \beta_0 + \theta_0. \tag{3.26}$$

For a given value of κ, all the required quantities can be computed and the loads are assessed.

The results for a 2D section will be shown over a range of the non-dimensional spring stiffness

$$\Gamma = \frac{\kappa^{2\mathrm{D}}}{\rho_w c^2 \overline{U}^2}. \tag{3.27}$$

Γ is the ratio between the two-dimensional stiffness and a representative hydrodynamic moment. The latter is taken as the product of the hydrodynamic force $\rho_w \overline{U}^2 c$ and the arm c.

3.4 Quasi-steady Analysis of the 3D Morphing Blade

In this section, I study a morphing blade where the blade deflection at every spanwise position is the same. The blade morphing is seen as a rigid rotation around the pitch axis and its flexibility is modelled as a torsional spring mounted at the root of the blade (Fig. 3.5b). I study the impact of the proposed passive pitch system for a rigid blade pitching around an axis at the chordwise coordinate $\hat{x}_A = 0.1c$, rotating at the optimal tip speed ratio $\lambda_0 = 4.5$ for a far-field speed $U_{\mathrm{hub}} = 2$ m s^{-1} at the hub height z_{hub}. The pitching equilibrium is again dictated by the spring reaction and by the hydrostatic loads. The spring acts as a lumped, flexible connection between the blade and the hub and its moment reaction is

$$M_{\mathrm{s}} = -\kappa\theta. \tag{3.28}$$

The hydrostatic moment M_{qs} takes into account the sum of the moments applied on each i-th section of the blade, and is computed as

$$M_{\mathrm{qs}} = \sum_i \frac{1}{2}\rho_w U_i(t)^2 c_i^2 C_{M_i}(\alpha_i)\delta r_i. \tag{3.29}$$

The quasi-steady equations that describe the motion of the blade are

$$\begin{cases} M_{\mathrm{s}} + M_{\mathrm{qs}} = 0 & \text{(a)} \\ \phi_i(t) = \beta_i(t) + \alpha_i(t) & (\mathrm{b}_i) \\ \beta_i(t) = \beta_{0_i} + \delta\theta(t) & (\mathrm{c}_i) \end{cases} \tag{3.30}$$

The optimisation problem is stated similarly to the 2D section case. However, since the entire blade is considered, the minimisation is imposed on the out-of-plane blade root bending moment coefficient C_{RBM}, whereas the constraint considers the power generated by the entire blade. The optimisation problem is stated as

$$\begin{aligned} \min_{\kappa} \hat{J}(\kappa) &= \Delta C_{\mathrm{RBM}} \\ \text{s.t.} \quad & \frac{\partial \overline{C}_P}{\partial \kappa} = 0 \end{aligned} \tag{3.31}$$

where

$$\overline{C}_P = \frac{1}{2\pi}\int_0^{2\pi} C_P(\psi)\,\mathrm{d}\,\psi, \tag{3.32}$$

and ΔC_{RBM} is the amplitude of $C_{\mathrm{RBM}} = M_{\mathrm{RB}} / \left(\frac{1}{2}\rho_w U_{\mathrm{hub}}^2 RA\right)$, with $M_{\mathrm{RB}} = \sum_i r_i T_i^{2\mathrm{D}} \delta r_i$ the blade root out-of-plane bending moment.

The optimisation problem is solved using an exhaustive search approach.To meet the requirement of constant power extracted, the spring preload is computed similarly to the two-dimensional case as

$$\theta_0 = \frac{1}{\kappa} \sum_i \frac{1}{2} \rho_w \overline{U}_i^2 c_i^2 (C_{M_i,\alpha} \overline{\alpha}_i + C_{M_i,0}) \delta r_i. \tag{3.33}$$

By combining Eq. 3.30 with $\delta\theta = \theta - \theta_0$ I compute the spring deformation θ at each time step as

$$\theta(t) = \frac{\sum_i \frac{1}{2} \rho_w c_i^2 U_i^2 \left(C_{M_i,\alpha} \left(\phi(t) - \beta_0 + \theta_0 \right) + C_{M_i,0} \right) \delta r_i}{\kappa + \sum_i \frac{1}{2} \rho_w c_i^2 U_i^2 C_{M_i,\alpha} \delta r_i}. \tag{3.34}$$

Then, using the complementarity of angles (Eqs. 3.30b$_i$, c$_i$), the angle of attack is determined as

$$\alpha_i(t) = \phi_i(t) - \beta_{0_i} - \theta + \theta_0. \tag{3.35}$$

Using the above equations for θ and α and the preload θ_0, all the loads acting on the blade can be computed.

3.5 Dynamic Analysis of the 3D Morphing Blade

I consider a hollow blade made of composite layers then filled with water Bir et al. [172]. The inertia $J^{2\mathrm{D}}$ of each blade section is obtained by

$$J^{2\mathrm{D}} = \rho_s \int_{\Omega_s} \overline{\boldsymbol{AB}}^2 d\Omega + \rho_w \int_{\Omega_w} \overline{\boldsymbol{AB}}^2 d\Omega, \tag{3.36}$$

where ρ_s and ρ_w are the density of the blade shell and the density of water respectively, Ω_s is the area of the blade shell on the section, Ω_w is the area occupied by the water within and $\overline{\boldsymbol{AB}}$ represents the relative position of a

generic section element from the pitching axis (Fig. 3.6). A blade usually presents a box spar for structural reasons. Since the spar is placed very close to the pitch axis, it has little influence on the blade inertia and its torsional dynamics, and it is therefore neglected. The inertia J of the entire blade is then computed as

$$J = \sum_i J_i^{2\mathrm{D}} \delta r_i, \tag{3.37}$$

for $i = 1...N$, with N the number of equally spaced blade sections.

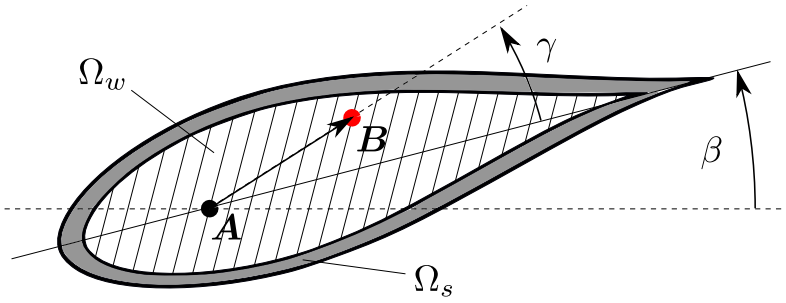

Figure 3.6: The blade is composed by a composite shell filled with water.

The blade rotates around the rotor axis with angular velocity ω. This leads to the Euler force $\boldsymbol{F}_{\mathrm{Eu}} = -m\frac{d\boldsymbol{\omega}}{dt} \wedge \boldsymbol{r}$, the Coriolis force $\boldsymbol{F}_{\mathrm{Co}} = -m\boldsymbol{\omega} \wedge \frac{d\boldsymbol{r}}{dt}$ and the centrifugal force $\boldsymbol{F}_{\mathrm{c}} = -m\boldsymbol{\omega} \wedge \big(\boldsymbol{\omega} \wedge \boldsymbol{r}\big)$. In this case, the Euler force disappears because I consider a constant rotation rate ($\frac{d\boldsymbol{\omega}}{dt} = 0$). The Coriolis force is also equal to zero because solid points on the blade do not move radially ($\frac{d\boldsymbol{r}}{dt} = 0$). Conversely, there is a component of $\boldsymbol{F}_{\mathrm{c}}$ that lies in the section plane which generates a pitching moment (Fig. 3.7). For a generic point $\boldsymbol{B}$ on a blade section, this force, $\boldsymbol{F}_{\mathrm{c}}^B$, generates a moment $\boldsymbol{M}_{\mathrm{c}}^B = \overline{\boldsymbol{AB}} \wedge \boldsymbol{F}_{\mathrm{c},\psi}^B$ that tends to align the blade with the rotor plane.

The centrifugal moment is evaluated for each section as

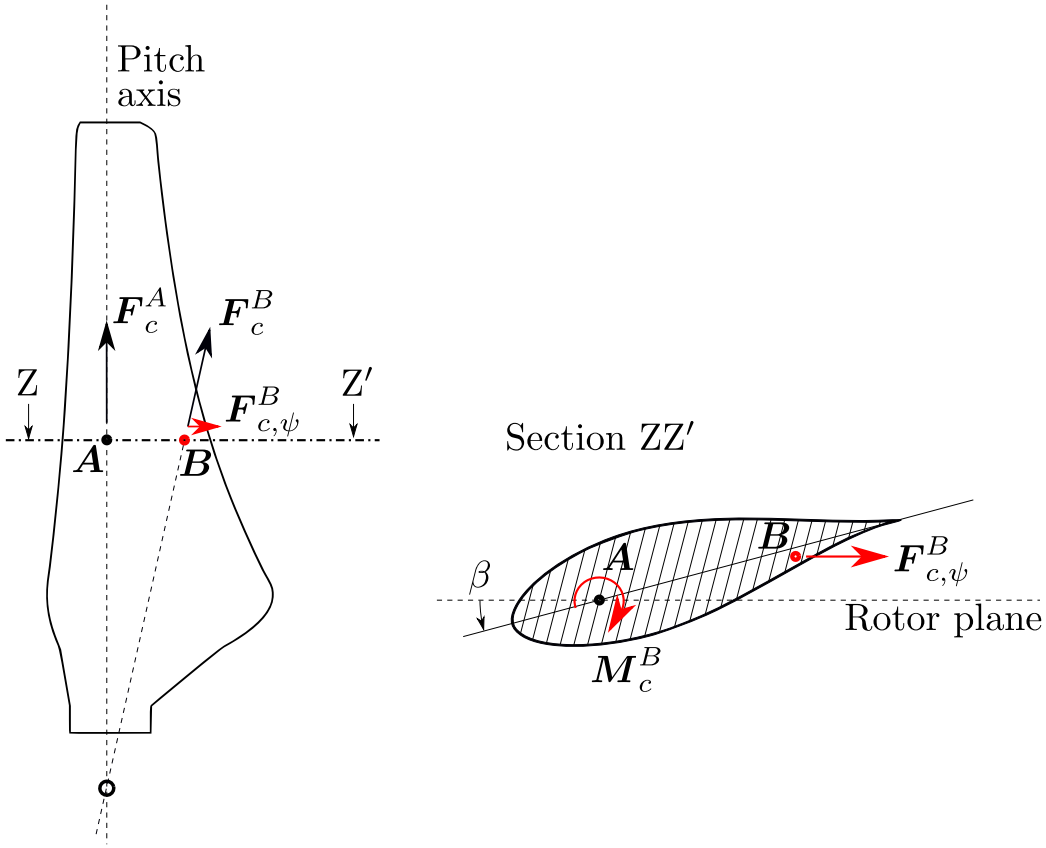

Figure 3.7: A generic small element of a section that does not lie on the pitch axis is subjected to a centrifugal moment $\boldsymbol{M}_c^B$.

$$\begin{aligned} M_c^{2D}(\beta) = &- \frac{1}{2}\omega^2\rho_s \int_{\Omega_s} \overline{\boldsymbol{AB}}^2 \sin(2(\beta+\gamma))\,\mathrm{d}\,\Omega \\ &- \frac{1}{2}\omega^2\rho_w \int_{\Omega_s} \overline{\boldsymbol{AB}}^2 \sin(2(\beta+\gamma))\,\mathrm{d}\,\Omega, \end{aligned} \tag{3.38}$$

where $\beta+\gamma$ is the angular distance of a blade element from the rotor axis (Fig. 3.6).

A Taylor-Young first-order expansion is used to approximate the centrifugal moment as

$$M_c^{2D} \approx M_c^{2D}(\beta_0) + \frac{\partial M_c^{2D}}{\partial \beta}\delta\beta. \tag{3.39}$$

This approximation is valid as long as $\beta \approx \beta_0$, a condition that is met by imposing the requirement of constant power generated (Eq. 3.31). By construction, $\delta\beta \equiv \delta\theta$ (Fig. 3.4). Hence, Eq. 3.39 is rearranged to make explicit the dependency of the centrifugal moment to the spring deformation. The centrifugal moment acting on the entire blade is

$$M_{\mathrm{c}} \approx \sum_i \left(M_{\mathrm{c}_i,0} + M_{\mathrm{c}_i,\theta}\delta\theta\right)\delta r_i, \tag{3.40}$$

where $M_{\mathrm{c},0} = M_{\mathrm{c}}^{\mathrm{2D}}(\beta_0)$ and $M_{\mathrm{c},\theta} = \frac{\partial M_{\mathrm{c}}^{\mathrm{2D}}}{\partial\theta}$.

The preload angle is computed for average flow conditions, and pitch angle $\beta(t) = \beta_0$. Under these conditions, the centrifugal moment is the only dynamic contributions to the preload angle. Equation 3.33 is thus modified as

$$\theta_0 = \frac{1}{\kappa}\sum_i \left[\frac{1}{2}\rho_w \overline{U}_i^2 c_i^2 (C_{M_i,\alpha}\overline{\alpha}_i + C_{M_i,0}) + M_{\mathrm{c}_i,0}\right]\delta r_i. \tag{3.41}$$

A detailed calculations of the centrifugal and inertial terms on a rotating blade can be found in centforces.

The contribution of the gravity force is neglected. The composite blade shell is filled with water [172], the density of the whole blade is assumed to match that of the surrounding water, and the gravitational force is in equilibrium with the buoyancy force.

3.5.1 Unsteady Hydrodynamics

The oscillations due to the shear flow are periodic but not harmonic, and to estimate the dynamic loads acting on the blade using Theodorsen's theory, I have to consider sinusoidal variations of the angle of attack. I determined the fluctuations of the axial velocity (U_x) such that the angle of attack would fluctuate harmonically with the same amplitude and the same mean value as the inflow oscillations due to the shear profile (Fig. 3.8). This procedure can be

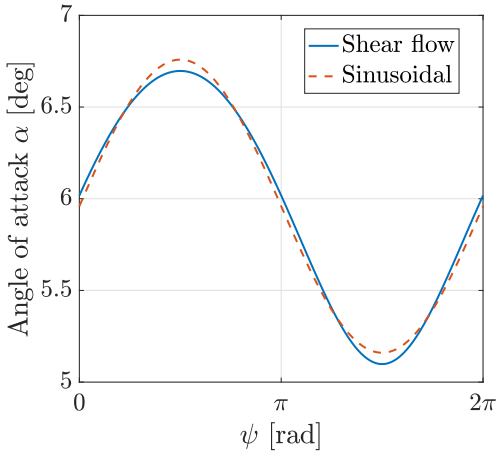

Figure 3.8: The fluctuations of the angle of attack are approximated by a sinusoidal shape (shown here for $r = 0.75R$).

readily extended to generic inflow conditions, where the signal is decomposed in its Fourier harmonic components, and their effects are superimposed via Theodorsen's linear theory. The variations in the angle of attack and in the axial velocity lead to additional pitching moment contributions. Following Theodorsen, the moment on a 2D foil pitching sinusoidally is

$$\begin{aligned} M_{\mathrm{dy}}^{\mathrm{2D}} = \rho_w b^3 \pi \left[\left(\frac{1}{2} - \frac{d}{b} \right) U \delta\dot{\alpha} + b \left(\frac{1}{8} + \left(\frac{d}{b} \right)^2 \right) \delta\ddot{\theta} \right] \\ -2\rho_w U b^3 \pi \left(\frac{1}{2} + \frac{d}{b} \right) C(k) \left(\frac{1}{2} - \frac{d}{b} \right) \delta\dot{\theta} \\ + \frac{1}{2} \rho_w U^2 c^2 C_{M,\alpha} C(k) \delta\alpha \\ + \frac{1}{2} \rho_w U^2 c^2 \left[C_{M,\alpha} \overline{\alpha} + C_{M,0} \right], \end{aligned} \tag{3.42}$$

where $\delta\alpha = \alpha - \overline{\alpha}$, $C(k)$ is Theodorsen's circulation function that us expressed in terms of Hankel functions of the reduced frequency $k = \frac{\omega b}{U}$. The unsteady pitching moment for the whole blade accounts for the contributions of each section and it is computed as

$$M_{\mathrm{dy}} = \sum_i M^{\mathrm{2D}}_{\mathrm{dy}_i} \delta r_i, \tag{3.43}$$

The aerodynamic lift L for the quasi-steady analysis accounts only for the hydrostatic loads (Eq. 3.6) whereas, in the dynamic analysis, it accounts for both the dynamic and the hydrostatic contributions and is computed as

$$\begin{aligned} L = \pi\rho_w b^2 \left[U\delta\dot{\alpha} - b\left(\frac{d}{b}\right)\delta\ddot{\theta} \right] + 2\pi\rho_w U b^2 C(k) \left(\frac{1}{2} - \frac{d}{b}\right)\delta\dot{\theta} \\ + \frac{1}{2}\rho_w U^2 c \left[C(k) C_L(\alpha) + (1 - C(k))\, C_L(\overline{\alpha}) \right]. \end{aligned} \tag{3.44}$$

The dynamic equations for the blade are

$$\begin{cases} M_{\mathrm{s}} + M_{\mathrm{c}} + M_{\mathrm{dy}} - \mu\delta\dot{\theta} = J\delta\ddot{\theta} & (\mathrm{a}) \\ \phi_i(t) = \beta_i + \alpha_i(t) & (\mathrm{b}_i) \\ \beta_i(t) = \beta_{0_i} + \delta\beta_i(t), & (\mathrm{c}_i) \end{cases} \tag{3.45}$$

where μ is a parameter that accounts for the mechanical damping of the blade.

The sectional hydrodynamic torque $M^{\mathrm{2D}}_{\mathrm{dy}_i}$ is a function of the average angle of attack $\overline{\alpha}_i$ and of its fluctuations $\delta\alpha_i$ (Eq. 3.42). Using the complementarity of the angles in Eqs. 3.45b$_i$ and 3.45c$_i$, it is possible to express $\delta\alpha_i$ as a function of $\delta\theta$, and to obtain an expression for the blade hydrodynamic torque in Eq. 3.43 which depend only on $\delta\theta$ and its first and second time derivative. By substituting Eqs. 3.28, 3.40, 3.43 into Eq. 3.45a, the morphing blade dynamic equilibrium is formulated as:

$$\begin{aligned}\left(J-\sum_i I_{\mathrm{am}_i}\delta r_i\right)\delta\ddot{\theta}+\left(\mu+\sum_i\left(C^{nc}_{\mathrm{am}_i}-C^{c}_{\mathrm{am}_i}\right)\delta r_i\right)\delta\dot{\theta}\\ +\left(\kappa+\sum_i\left(K_{\mathrm{am}_i}-M_{\mathrm{c}_i,\theta}\right)\delta r_i\right)\delta\theta\\ =\sum_i\left(C^{nc}_{\mathrm{am}_i}\delta\dot{\phi}_i+K_{\mathrm{am}_i}\delta\phi_i+M^{\mathrm{2D}}_{\mathrm{qs}_i}(\overline{\phi}_i-\beta_{0_i})+M_{\mathrm{c}_i,0}\right)\delta r_i-\kappa\theta_0,\end{aligned}\tag{3.46}$$

where

$$\begin{aligned}I_{\mathrm{am}}&=\rho_w b^4\pi\left(\frac{1}{8}+\left(\frac{d}{b}\right)^2\right),\\ C^{c}_{\mathrm{am}}&=-\rho_w U b^3\pi\left(\frac{1}{2}-\frac{d}{b}\right)\left(1+2\frac{d}{b}\right)C(k),\\ C^{nc}_{\mathrm{am}}&=-\rho_w U b^3\pi\left(\frac{1}{2}-\frac{d}{b}\right),\\ K_{\mathrm{am}}&=\frac{1}{2}\rho_w U^2 c^2 C_{M,\alpha}C(k),\\ M^{\mathrm{2D}}_{\mathrm{qs}_i}(\overline{\alpha})&=\frac{1}{2}\rho_w U^2 c^2\left[C_{M,\alpha}\overline{\alpha}+C_{M,0}\right],\end{aligned}\tag{3.47}$$

The fluctuations are defined by $\delta\phi=\frac{\Delta\phi}{2}\exp(j\omega t)$ and $\delta\alpha=\frac{\Delta\alpha}{2}\exp(j\omega t)$, where $\Delta\phi$ and $\Delta\alpha$ represent the amplitude of the fluctuations of the respective angles and j is the imaginary unit. The blade is expected to oscillate with the same period, namely $\delta\theta=\frac{\Delta\theta}{2}\exp(j\omega t+\chi)$. By substituting $\delta\dot{\theta}=j\omega\delta\theta$, $\delta\ddot{\theta}=-\omega^2\delta\theta$, $\delta\dot{\phi}=j\omega\delta\phi$ and $\delta\ddot{\phi}=-\omega^2\delta\phi$, Eq. 3.46 is rewritten as

$$\begin{aligned}\Bigg[-\omega^2\left(J-\sum_i I_{\mathrm{am}_i}\delta r_i\right)+j\omega\left(\mu+\sum_i\left(C^{nc}_{\mathrm{am}_i}-C^{c}_{\mathrm{am}_i}\right)\delta r_i\right)\\ +\left(\kappa+\sum_i\left(K_{\mathrm{am}_i}-M_{\mathrm{c}_i,\theta}\right)\delta r_i\right)\Bigg]\delta\theta\\ =\sum_i\left(\left(j\omega C^{nc}_{\mathrm{am}_i}+K_{\mathrm{am}_i}\right)\delta\phi_i+M^{\mathrm{2D}}_{\mathrm{qs}_i}(\overline{\phi}_i-\beta_{0_i})+M_{\mathrm{c}_i,0}\right)\delta r_i-\kappa\theta_0.\end{aligned}\tag{3.48}$$

The dynamics of $\delta\theta$ are determined by the algebraic solution of Eq. 3.48 for each time step and the equilibrium position of the blade is computed as $\theta = \theta_0 + \delta\theta$. The solution method is inspired by the work of medina2018lift.

The optimisation problem is defined as for the quasi-steady case (Eq. 3.31), where the loads account for the unsteady contributions described in Eq. 3.44. The angle of attack is determined as for the quasi-steady analysis using Eq. 3.35, hence all the loads acting on the blade can be computed.

In the Results (Sections 5.2, 5.3), I present the spring stiffness κ and the material damping μ in terms of the nondimensional coefficients

$$\begin{aligned} C_\kappa &= \frac{\kappa}{\rho_w U_{\text{hub}}^2 A c}, \\ C_\mu &= \frac{\mu}{\rho_w U_{\text{hub}} A c^2}. \end{aligned} \tag{3.49}$$

Akin to Γ, also C_κ and C_μ are made nondimensional using a hydrodynamic force and the length scale c. Here, the force is that acting on the rotor disk and it is proportional to $\rho_w U_{\text{hub}}^2 A$. It is noted that both the coefficients are based on the force on the rotor disk and do not account for the hydrodynamic force associated with the tangential velocity. Hence, as the tip speed ratio increases, the optimum κ and C_κ are expected to increase to match the higher hydrodynamic force associated with the rotation.

3.6 Real inflow conditions

To verify whether the proposed morphing blade concept can be effective in mitigating unsteady flow conditions, I test the performance of the model using real inflow conditions. The inflow data was acquired at the EMEC tidal test site during field measurements campaigns conducted by the University of Edinburgh for the ReDAPT project (2011-2015). Environmental data acquired up to October 2014 is publicly available at the UKERC Energy Data Centre UKERC [173]. For this study, I use a flow sample measured at EMEC during a flood tide on 22 November 2014. This sample was originally chosen

by Scarlett et al. [8] to investigate numerically the unsteady hydrodynamic response of the Tidal Generation Limited (TGL) turbine subjected to large waves and opposing current. The significant wave height in the sample is 4.2 m, the maximum observed height is about 5 m, and the wave period is 10 s. The turbine is operating at the optimal tip speed ratio 4.5, the magnitude of the inflow speed averaged over the area and the sample time period is 2.77 m s^{-1}, and the rotational speed of the turbine is $\omega = 1.38$ rad s^{-1}. Further details about the measured flow conditions and the measurement system are found in Scarlett et al. [8].

3.6.1 Fourier decomposition of generic inflow

The blade deflection at every spanwise position is computed in a similar fashion to what described in Section 3.4, the blade flexibility is modelled as a torsional spring mounted at the root, and the blade pitches around an axis at the chordwise coordinate $\hat{x}_A = 0.1c$. The pitching equilibrium is described using the quasi-steady analysis in Eq. 3.30 and the unsteady analysis in Eq. 3.45. To use Theodorsen's unsteady aerodynamic theory, the inflow fluctuations must be harmonic and for each section it is approximated using a series of Fourier components, instead of a single sinusoid like in the simpler case of shear flow. The amplitude of the fluctuations is defined for each section as

$$\delta\phi = \sum_{k=1}^{N_k} \frac{\Delta\phi_k}{2} \exp(j\omega_k t + \chi_k) \tag{3.50}$$

and

$$\delta\alpha = \sum_{k=1}^{N_k} \frac{\Delta\alpha_k}{2} \exp(j\omega_k t + \chi_k), \tag{3.51}$$

where N_k is the number of Fourier components considered, $\Delta\alpha_k$ and $\Delta\phi_k$ are the amplitudes of each component, and the period of the slowest harmonic ω_1 corresponds to the length of the inputs time series (i.e. 56 rota-

tional periods). Figure 3.9 shows the time history of the angle of attack at the blade spanwise position $r/R = 0.75$, over 10 rotational periods T_r, and the approximated signal using $N_k = 50$, 100 and 150 Fourier components. The main source of unsteadiness is due to low-frequency waves, which are well approximated in all three cases. Increasing the number of Fourier components improves the approximation of high frequency components which carry less energy and are thus less important. The series converges slowly, the computational cost rises rapidly, and the approximation improves less and less with each additional Fourier component. The unsteady simulations presented in Chapter 5 are run using $N_k = 100$ Fourier components, which allow to capture phenomena with twice the rotational frequency of the turbine.

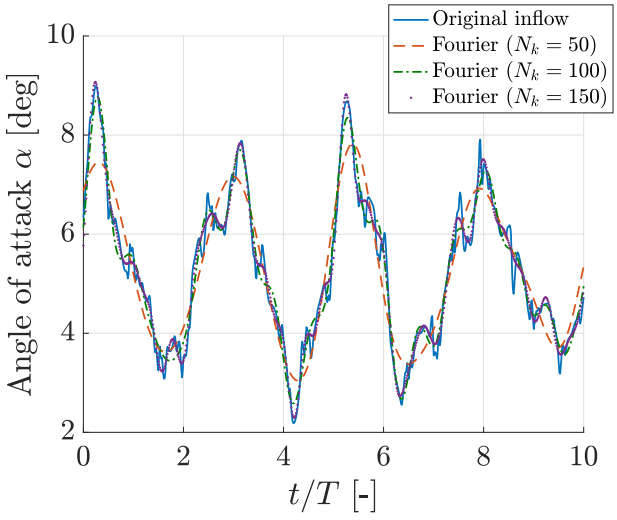

Figure 3.9: Time history of the angle of attack at $r/R = 0.75$. Graph shows original signal (blue line), and signal approximated using 50 (red dashed line), 100 (green dot-dash line), and 150 (purple dotted line) Fourier components respectively.

To solve the pitch dynamics, Eq. 3.48 is rewritten as

$$\begin{aligned}\Bigg[-\omega_k^2 \left(J - \sum_i I_{\mathrm{am}_i} \delta r_i \right) + j\omega_k \left(\mu + \sum_i \left(C^{nc}_{\mathrm{am}_i} - C^{c}_{\mathrm{am}_{i,k}} \right) \delta r_i \right) \\ + \left(\kappa + \sum_i \left(K_{\mathrm{am}_{i,k}} - M_{\mathrm{c}_i,\theta} \right) \delta r_i \right) \Bigg] \delta\theta_k \\ = \sum_i \left(\left(j\omega_k C^{nc}_{\mathrm{am}_i} + K_{\mathrm{am}_{i,k}} \right) \delta\phi_{i,k} + M^{\mathrm{2D}}_{\mathrm{qs}_i} (\overline{\phi}_i - \beta_{0_i}) + M_{\mathrm{c}_i,0} \right) \delta r_i - \kappa\theta_0.\end{aligned} \tag{3.52}$$

and it is solved for $\delta\theta_k$ for each Fourier component ($k = 1 : N_k$). The total blade deflection is obtained as $\delta\theta = \sum_{k=1}^{N_k} \delta\theta_k$. The lift is computed for each section as

$$\begin{aligned}L = \sum_{k=1}^{N_k} \pi\rho_w b^2 \left[U\delta\dot{\alpha}_k - b\left(\frac{d}{b}\right)\delta\ddot{\theta}_k \right] + 2\pi\rho_w U b^2 C(k_k) \left(\frac{1}{2} - \frac{d}{b} \right) \delta\dot{\theta} \\ + \frac{1}{2}\rho_w U^2 c \left[C(k_k) C_L(\overline{\alpha} + \delta\alpha_k) + (1 - C(k_k))\, C_L(\overline{\alpha}) \right].\end{aligned} \tag{3.53}$$

The optimisation problem is defined in Eq. 3.31 and solved using an exhaustive search algorithm varying the input spring stiffness. For any stiffness, the preload is computed using Eq. 3.33. The optimum is represented by the stiffness and preload that minimise the fluctuations of the out-of-plane blade root bending moment C_{RBM}, whilst keeping constant the average power generated by the turbine.

4

Code inputs and validation

4.1 Input parameters

The aerodynamic coefficients C_L, C_D for the blade sections profiles are taken from Gretton and Ingram [174] for a Reynolds number $\mathrm{Re} = 3 \times 10^6$ which matches the flow on a full-scale tidal turbine. The shape of the blade sections is the NACA $63_{(318)}-4xy$, based on the NACA 6−series designation given by, for instance, Abbott and Von Doenhoff [175]. The thickness xy in percentage of the foil chord varies from the NACA $63_{(318)} - 455$ near the root to the NACA $63_{(318)} - 418$ at the blade tip. An overview of the blade geometry is showed in Fig. 4.1 and data is provided in Table 4.1. The blades are thicker at the root, which results in a smooth force variation near the stall angle. For the blade sections with thickness up to 40%, the foil characteristics are interpolated from the data provided by Gretton and Ingram [174]. Instead, for thicker sections, the C_L and C_D of the 40%-thick section are used.

The quarter-chord pitching moment $C_{M_{1/4}}$, which is not provided by Gretton and Ingram [174], for all sections is that of a NACA $63_3 - 418$ (Fig. 4.2), taken from Abbott and Von Doenhoff [175]. The parameters used in the simulations are resumed in Table 4.2.

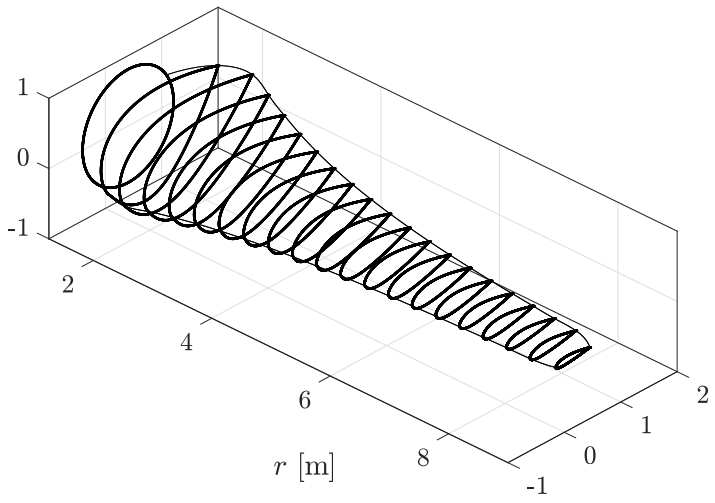

Figure 4.1: TGL blade geometry adapted from Gretton and Ingram [174].

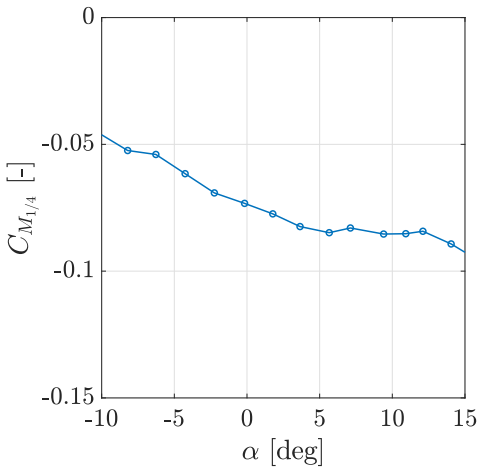

Figure 4.2: Quarter chord pitching moment coefficient for a NACA $63_3 - 418$ as a function of α, at $\mathrm{Re} = 3 \times 10^6$. Data taken from Abbott and Von Doenhoff [175].

4.2 Code Validation

The low-order code is validated for different aspects that determine the results accuracy. First, the predictions of average turbine loads and blade load distributions are compared to experimental results over a range of operating conditions to verify that the code can reliably predict the loads on an

Radius [m]	Twist [deg]	Chord [m]	Thickness ratio	Profile
1.25	32.5	1.612	1.000	Circle
2.05	23.2	2.271	0.550	$63_{(318)} - 455$
2.45	19.9	2.119	0.533	$63_{(318)} - 453$
2.85	17.2	1.962	0.511	$63_{(318)} - 451$
3.25	14.9	1.813	0.485	$63_{(318)} - 449$
3.65	13.1	1.677	0.454	$63_{(318)} - 445$
4.05	11.5	1.556	0.422	$63_{(318)} - 442$
4.45	10.2	1.447	0.390	$63_{(318)} - 439$
4.85	9.1	1.351	0.359	$63_{(318)} - 436$
5.25	8.1	1.265	0.330	$63_{(318)} - 433$
5.65	7.2	1.189	0.306	$63_{(318)} - 431$
6.05	6.4	1.120	0.286	$63_{(318)} - 429$
6.45	5.8	1.058	0.275	$63_{(318)} - 427$
6.85	5.2	1.003	0.267	$63_{(318)} - 427$
7.25	4.6	0.953	0.255	$63_{(318)} - 426$
7.65	4.2	0.907	0.243	$63_{(318)} - 424$
8.05	3.7	0.865	0.227	$63_{(318)} - 423$
8.45	3.3	0.827	0.208	$63_{(318)} - 421$
8.85	3.0	0.792	0.188	$63_{(318)} - 419$
9	2.8	0.600	0.180	$63_3 - 418$

Table 4.1: Blade geometry.

horizontal-axis turbine. A comparison is thus presented with the results of Gretton and Ingram [174] to cross-check that the turbine geometry, the inflow conditions, and the operating conditions are implemented correctly for the scenario considered in Chapter 5. Then, the unsteady load prediction capabilities are validated against experimental and numerical results from the literature to justify the use of unsteady load model over a quasi-steady model, and finally the load-mitigating performance of the passive morphing blade are validated against numerical results to show that the model is capable of modelling a morphing blade.

The prediction of the turbine average loads are validated against the experimental results from NREL-NASA Unsteady Aerodynamic Experiment (UAE) phase 6. The purpose of the experimental test campaign was to ac-

	Blade section	
	$r = 0.5R$	$r = 0.75R$
Mean angle of attack $\overline{\alpha}$ [deg]	9.58	5.96
Twist angle β_0 [deg]	10.17	5.39
Chord c [m]	1.445	1.019
Foil type	NACA $63_{(318)}439$	NACA $63_{(318)}427$
Axial induction factor a [-]	0.1835	0.3112
Tangential induction factor a' [-]	0.0182	0.0164
Mean inflow speed $\overline{U}$ [m s^{-1}]	4.82	6.98
Blade length R [m]	9	
Far field flow speed U_{hub} [m s^{-1}]	2	
Hub height z_{hub} [m]	20	
Pitch axis position $\hat{x}_A/c$ [-]	0.1	
Rotational speed ω [rad s^{-1}]	1	
Blade shell thickness [mm]	56.5 (root) - 14.5 (tip)	
Blade shell density ρ_{s} [kg m^{-3}]	570 (root) - 660 (tip)	
Water density ρ_{w} [kg m^{-3}]	1025	

Table 4.2: Simulation parameters.

quire accurate aerodynamic and structural measurements on a wind turbine geometrically and dynamically representative of full-scale machine, and to exploit the data to validate and develop enhanced numerical turbine models. The experimental data was acquired in 1987 in the large wind tunnel at the NASA-Ames Research Center, using a 10 m diameter wind turbine instrumented to measure blade surface pressure at five different span locations. The wind turbine features two blades with linear taper, non-linear twist distribution, and uses the S809 airfoil from root to tip. Details of the blade geometry and of the aerodynamic load coefficients are publicly available from Hand et al. [176]. Blade loads were extrapolated from the surface pressure distribution, thrust and torque were integrated along the span of the blade and multiplied by the number of blades to give a rough estimate of loads applied to the entire rotor, and blade root bending moments were measured via strain gauges. Additional flow information was recorded by wind tunnel personnel using standard instrumentation. The measured data can be downloaded freely from NREL UAE 6 website [177].

The low-order code was initialised with the turbine geometry and pitch setting, and the operating conditions where determined using the wind speed measured upstream of the turbine, and the turbine rotational speed measurements. The low-order code predicted the turbine load for the turbine configuration adopted in test sequence H [176], where the turbine has zero cone angle and zero yaw angle, 3 deg pitch angle at the tip, and the pitch along the rest of the blade determined by the difference of the local twist angle to the tip geometric twist. The wind speed was varied between tests and kept constant throughout each test. The rotor speed was 72 rpm and constant in all tested conditions.

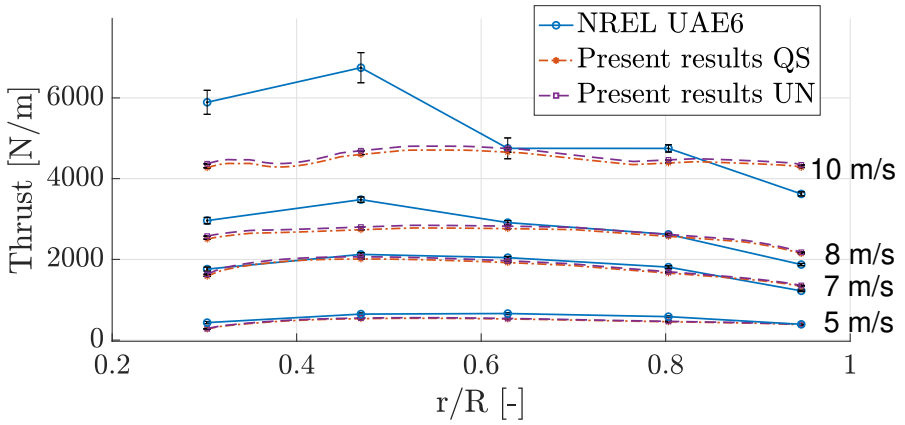

Figure 4.3: Spanwise thrust distribution. Comparison of sectional thrust predicted using quasi-steady and unsteady models with experimental results from NREL UAE VI, at four different wind speeds.

Figures 4.3, 4.4 show the thrust and torque spanwise distribution. Each figure shows four groups of curves corresponding to wind speeds 5 ms^{-1}, 7 ms^{-1}, 8 ms^{-1}, and 10 ms^{-1}. Each group shows three curves corresponding to the loads predicted by the quasi-steady model, the unsteady model, and the measured values respectively. For the experimental results, data is presented at locations 30%, 47%, 63%, 80%, and 95% of the blade span, where the sections where equipped with pressure transducers. Overall, the experimental and numerical results show a good match, especially at low

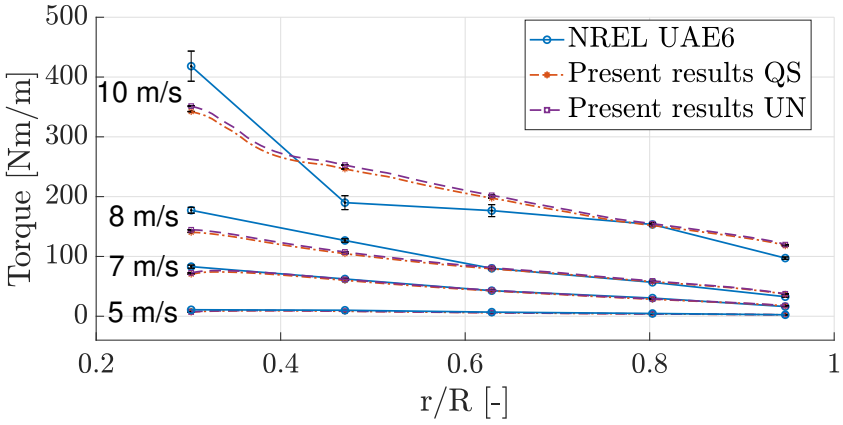

Figure 4.4: Spanwise torque distribution. Comparison of sectional torque predicted using quasi-steady and unsteady models with experimental results from NREL UAE VI, at four different wind speeds.

wind speed, where the TSR is high and the flow is attached. At wind speeds 8 ms^{-1} and 10 ms^{-1}, the results start to differ near the root, due to incipient separation, as shown by Sorensen et al. [178]. As expected, differences between average loads predicted by the quasi-steady model and by the unsteady model are negligible.

Figure 4.5 shows rotor thrust and torque, and the blade RBM for the same wind speeds. The loads are plotted against the TSR (bottom horizontal axis), and the corresponding wind speed is indicated on the additional axis on the top. The graphs show a good match of all loads in all conditions. The low-order code under-predicts thrust and torque, except at 10 ms^{-1} where the torque is slightly over-predicted. Instead, the computed RBM is higher than the measured value at all speeds except at 5 ms^{-1} despite the computed thrust being consistently lower. In fact, near the blade tip, the computed thrust is larger and it provides a greater contribution to the RBM than inboard sections, where the thrust is lower. The difference between computed and measured loads is always within 21% for thrust, 18% for torque, and 10% for RBM. Simms et al. [179] used the NREL-NASA UAE 6 data for a blind comparison with numerical models of varying complexity. A major finding

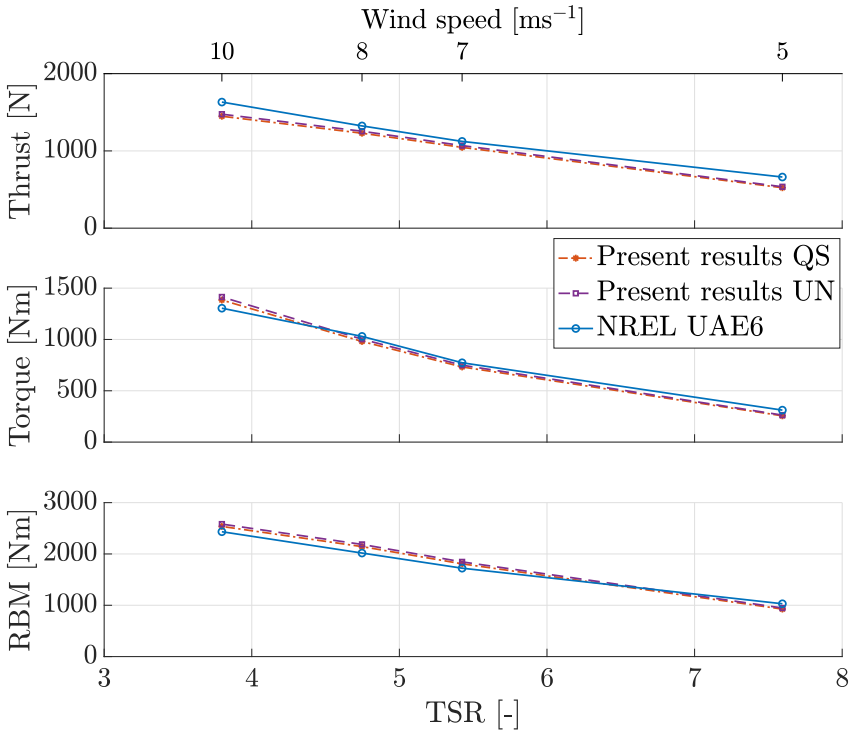

Figure 4.5: Thrust, torque and RBM at different wind speeds/TSR. The horizontal axis on the bottom indicates the TSR, whereas the horizontal axis on the top indicates the corresponding wind speed.

was that even at flow speed 7 ms^{-1}, where the flow is completely attached, the comparison showed a differences between experiments and models ranging $25 - 175\%$ for the power, and $85 - 150\%$ for the RBM. Discrepancies substantially increased above 10 ms^{-1} for all numerical models due to different degrees of separation, especially for BEMT-based models. Most models tended to over-predict blade bending moments even at lower wind speeds.

The present low-order code compared well in all tested conditions, including at flow speeds where separation starts to occur. In particular, spanwise loads show the inability of the code to model the flow near the root when separation occurs, but this seems to affect the rotor loads only marginally. Thrust, torque, and RBM differences are smaller than those observed for

other models with similar degree of complexity, confirming that the low-order code described in this thesis is capable of simulating the loads on a turbine with reasonable accuracy as long as no separation occurs on the blade, or the extent of the separation is confined to a small region near the root.

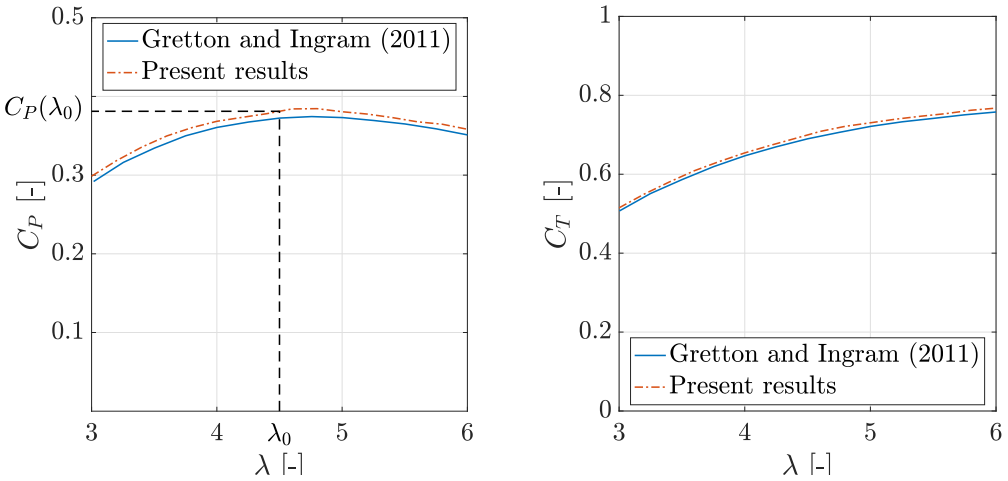

(a) Power coefficient **(b)** Thrust coefficient

Figure 4.6: Comparison of the BEMT results of this study and the CFD results from Gretton and Ingram [174] using $U_{\text{hub}} = 2$ m s^{-1}. C_P and C_T refer to the entire turbine.

The accuracy of the low-order code is thus assessed for a tidal turbine subjected to steady flow conditions, against the data from Gretton and Ingram [174]. This data was produced in the frame of the Performance Assessment of Wave and Tidal Array Systems (PerAWaT) project, launched in 2009 by the Energy Technologies Institute (ETI), a public-private partnership between engineering companies and the UK government. The aim of the project was to develop software tools for accurate predictions of energy yields from wave and tidal arrays, to inform arrays development and reduce commercial risk. These tools were thoroughly validated against scale model testing. In particular, Gretton and Ingram [174] realised the CFD model of the full-scale prototype turbine from TGL whose geometry I used throughout

my work, and studied it's behaviour at different tip speed ratio λ, where the free stream velocity is uniform with $U_\infty(z) = U_{\text{hub}}$ and $U_x = U_\infty(1-a)$. I compare the thrust and power coefficients in Fig. 4.6 with the results from the quasi-steady model. The difference of the computed power coefficient with the CFD data from Gretton and Ingram [174] is always smaller than 3%, whereas the thrust differs by less than 2% over the considered range $\lambda \in [3, 6]$, including the optimal operating point $\lambda_0 = 4.5$ where I study the performance of the morphing blade. This comparison shows once more that the code can reliably model the average loads on a horizontal-axis turbine across different operating conditions, and it indicates that the code inputs were setup correctly.

Next, I consider the accuracy of the model at predicting loads fluctuations when the turbine is subjected to unsteady flow. This part of the validation aims to show that the unsteady model produces more accurate load values than a quasi-steady model when a blade section experiences fluctuating inflow, and that it is thus better suited to model unsteady flow phenomena experienced by a turbine blade. Since the low-order model considers the flow over a section nominally 2D (i.e. independent from the flow on nearby sections), the unsteady model is compared against 2D data from the literature.

Figure 4.7 compares the lift coefficient history on an oscillating airfoil NACA 0012 with numerical (Lin et al. [180], Motta et al. [181]) and experimental data (Halfman [182]) from the literature. The airfoil was pitched harmonically with mean angle of attack $\overline{\alpha} = 0$ deg, fluctuations $\alpha = \overline{\alpha} \pm 6.7$ deg, at a reduced frequency $\overline{\kappa} = 0.4$. As the airfoil undergoes periodic oscillations, the lift value is affected by transient circulatory and non-circulatory phenomena which have a different impact on the loads depending on the frequency of the oscillations. At low reduced frequencies ($\overline{\kappa} < 0.1$), accelerations are low, hence inertial, non-circulatory effects (i.e. added mass) are small compared to circulatory effects. Due to the time needed to build-up more circulation when the angle of attack increases, the unsteady lift is lower than its quasi-steady value, the lift history shows hysteresis in the form of an oval-shape swept counterclockwise. For $\overline{\kappa} > 0.1$, like in Fig. 4.7, the foil acceleration

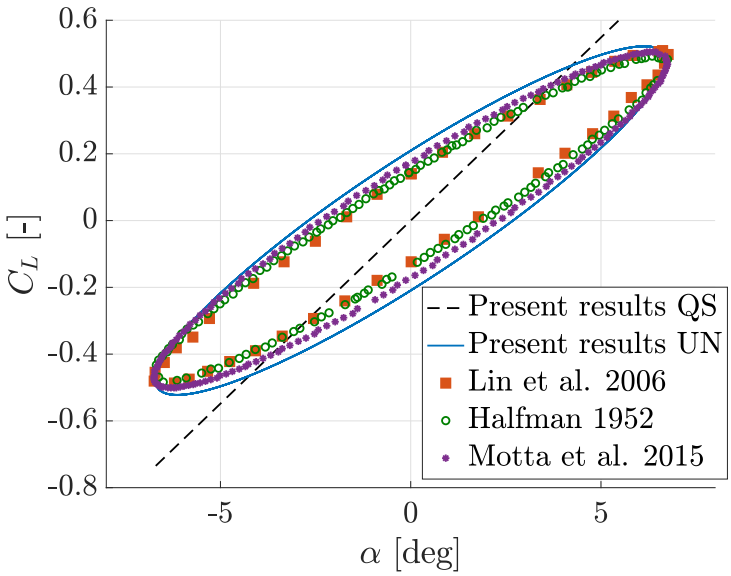

Figure 4.7: Lift coefficient on an oscillating foil NACA0012, with reduced frequency $\overline{\kappa} = 0.4$, $\overline{\alpha} = 0$ deg, $\alpha = \overline{\alpha} \pm 6.7$ deg. Present results are compared to numerical and experimental data.

is greater, inertial effects dominate over circulatory effects, and they cause the lift to anticipate the quasi-steady value, drawing a clockwise oval where the unsteady lift is higher than the quasi-steady lift for increasing angles and lower for decreasing angles. As reported by Motta et al. [181], Theodorsen's model slightly over-predicts the lift, however, the unsteady model compares better than the quasi-steady model to both numerical and experimental data from the literature. Although a zero average angle of attack is not representative of the conditions on a turbine blade, a non-zero average angle of attack only adds a steady contribution and it does not influence the unsteady behaviour as long the angle of attack oscillates below the static stall angle. The reduced frequency used in this comparison is representative of the unsteady phenomena experienced by the turbine blades (see Chapter 1). The comparison in Fig. 4.7 thus shows that the unsteady model is better suited to model unsteady blade loads than a quasi-steady model.

There is no experimental data for a turbine with a morphing concept such as that discussed in this thesis. Hence, the load predictions are validated for a

rigid blade and cannot be validated for the morphing blade. However, Dai et al. [183] performed a two-dimensional CFD investigation of the performance of a passively pitching NACA 63-427, which corresponds to the airfoil at $r/R = 0.75$ of the turbine blade used in the current study. They considered a rigid and an airfoil pitching passively around the axis at $\hat{x}_A = 0.1c$ and subjected to a periodically varying inflow speed representing a blade rotating in shear flow. The passive pitch was modelled with an akin mass-damper-spring system to that in this paper. The CFD predicted a reduction of the amplitude of the load fluctuations within 7% of the predictions of the present low-order model (Fig. 4.8).

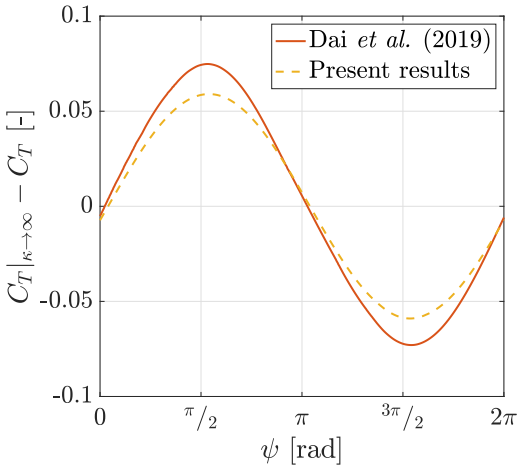

Figure 4.8: Comparison of CFD and analytical results showing the difference of C_T between rigid and morphing blades.

For the case of a turbine rotating in shear flow, whose performance are presented in Chapter 5, I validated the blade loads with the blade resolved CFD simulations performed by Dai in his PhD thesis [184]. The CFD simulations featured a structured mesh of about 23 million cells, where the turbine and hub are represented in a circular domain rotating within a larger cuboid domain. The two domains were coupled by a sliding internal interface. The larger, stationary domain spanned 17 turbine diameter in length, 11 diameters in width and 2 diameters in depth. A weakly-coupled fluid-structure interaction model was used to compute the passive-pitching of the blade,

where the mesh was morphed in response to the pitch dynamics determined by the structural solver. The fluid dynamic solution was obtained running a realizable $\kappa - \epsilon$ turbulence models to solve unsteady RANS equations. More details can be found in Dai [184].

The results of the low-order model are corrected by a bypass blocked flow factor τ_f as proposed by Whelan et al. [6]. They suggested that the turbine and its wake cause significant blockage due to the proximity of the surface and of the seabed. The external flow is sped up and the turbine loads are increased. The bypass blocked flow factor τ_f is the ratio of the bypass flow velocity (i.e. the velocity deflected past the rotor disc) and the far upstream velocity U_∞. The thrust coefficients is corrected as

$$C_T = C_T \tau_f^2. \tag{4.1}$$

Dai predicted a velocity ratio $\tau_f = 1.067$. Figure 4.9 compares the blade thrust coefficient C_T for the CFD and the unsteady results of the corrected low-order model. Morphing blades results are presented in both cases for a spring with non-dimensional stiffness $C_\kappa = 0.01$. The thrust coefficient predicted by the low-order model is within 0.2% of the CFD values at all times for the rigid blade, and within 0.4% for the morphing blade model. The tangential force coefficient predictions, indicative of the torque, differ less than 1% from the CFD results in the rigid case and also in the morphing case.

The low-order code presented in this thesis were validated against different experimental and numerical data to prove that the results presented in Chapter 5 are accurate and representative of the physics involved. In particular, the load-predicting capabilities where compared against experimental data from the NASA-NREL UAE 6 project [176], showing that the code can predict blade spanwise load distributions and rotor loads with an accuracy greater than similar codes, as long as the extent of flow separation at the root is limited. The code was then adapted to model the turbine and the flow

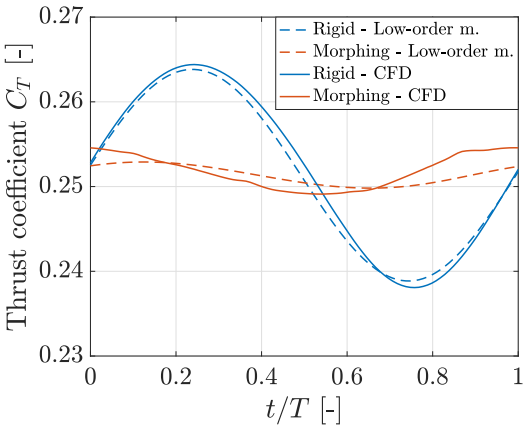

Figure 4.9: Comparison of CFD and analytical results showing the difference of C_T between rigid and morphing blades. Continuous lines represent the CFD results, dashed lines represent low-order model results (blue - rigid, red - morphing).

conditions used to for the assessment of the morphing blade load-mitigation performance in the next chapter. Comparing the results with numerical data [174] shows that the average loads can be correctly predicted. The unsteady load prediction where thus compared to experimental and numerical data from the literature [181], showing that for the flow unsteadiness experienced by a tidal turbine blade, the unsteady model employed in this work is better suited than a quasi-steady model to predict fluctuating loads. Finally, the load experienced by a morphing blade were compared to numerical results [183, 184], to further validate the capabilities of the code to model the loads on a passive, morphing blade. Overall, the code compared well in all the steps of the validation process, hence the code accuracy is appropriate for the purpose of this investigation, within the limits presented above.

5

Numerical results

5.1 Quasi-steady Analysis of a Morphing foil

The results for the passive pitch control applied to a 2D foil are presented here. Figure 5.1 shows the evolution of $\alpha(t)$ and $C_T^{2D}(t)$ for the foil at $r = 0.5R$ over the azimuthal coordinate ψ (Fig. 3.1), whereas Fig. 5.2 refers to the blade section at $r = 0.75R$. Both cases show the fluctuations over one revolution of the foils equipped with springs that are optimised to mitigate the thrust fluctuations for the respective flow conditions (Table 5.1). The non-dimensional stiffness Γ is defined as the ratio between spring stiffness κ and the hydrostatic stiffness $\rho_w c^2 \overline{U}^2$ (Eq. 3.27), and Γ_0 is the optimal value. On both blade sections, the thrust fluctuations are almost perfectly cancelled.

Similar performance can be achieved for any blade section as long as the stiffness and preload are optimised for the flow condition that the section experiences. Therefore, if each section can be equipped with the optimal stiffness and can deflect independently of the neighbouring sections, perfect unsteady load cancellation is possible also for the full blade.

Such optimal behaviour is possible thanks to the angle of attacks that varies in opposition to the fluctuations of the inflow angle. In fact when the inflow angle ϕ reaches a peak value, α is at a minimum, as observed by Shen et al. [37].

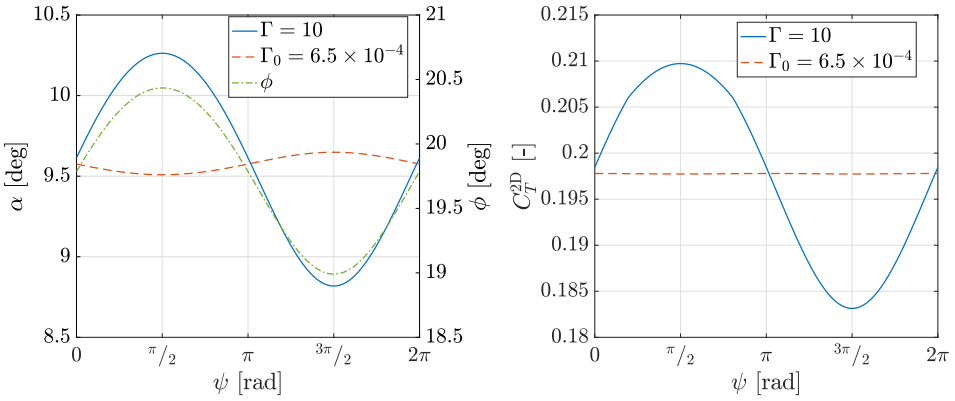

(a) **(b)**

Figure 5.1: Section at $r = 0.5R$: evolution of angle of attack (a) and thrust coefficient (b).

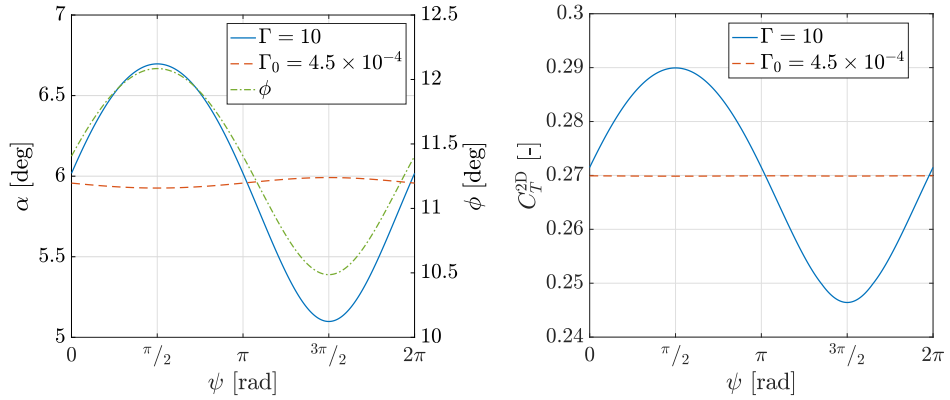

(a) **(b)**

Figure 5.2: Section at $r = 0.75R$: evolution of angle of attack (a) and thrust coefficient (b).

	Optimal spring properties		Thrust fluctuations ΔC_T^{2D}	
Blade section	Γ_0 [-]	θ_0 [deg]	% mean C_T^{2D}	% reduction
$r = 0.5R$	6.5×10^{-4}	132	0.03 (13.46)	99.74
$r = 0.75R$	4.5×10^{-4}	233	0.02 (16.12)	99.85

Table 5.1: Minimum load fluctuations using optimal springs for two blade sections. The number in parenthesis refer to the respective rigid blade sections.

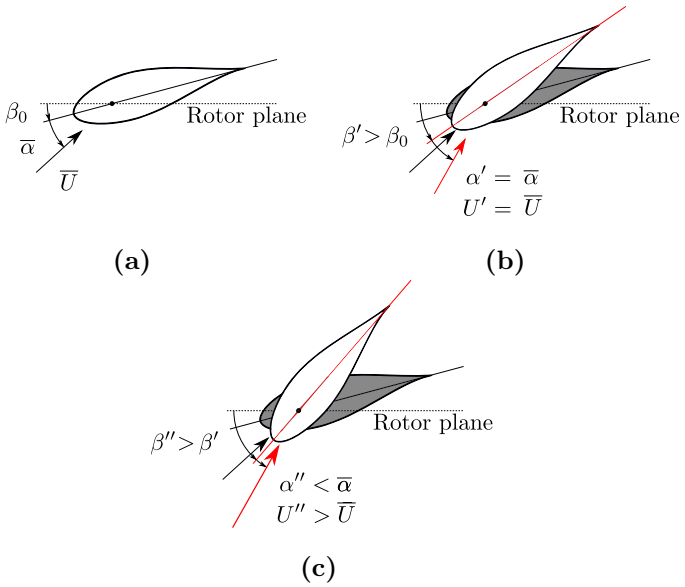

Figure 5.3: Reaction of the morphing foil to an increase of angle of attack and flow speed; (a) reference condition; (b) effect of the angle of attack only and (c) combined effect of the increase of both the angle of attack and flow speed.

This behaviour is explained in Fig. 5.3. The loads on the foil change because of the changes in the angle of attack but also in the flow velocity. When the blade is in the upper position, the foil pitches in order to compensate the incidence increase, such that both α and C_T^{2D} are restored to their initial values (Fig. 5.3b). However, the inflow speed increases as well causing higher hydrostatic moments which further pitch the foil (Fig. 5.3c). Essentially, the angle of attack is reduced to a value which is lower than its initial value to compensate the increase in the inflow speed. Similarly, when the blade is in the lower position, the foil pitches to a higher incidence in order to cancel the effect of the reduction in the incoming flow speed. Therefore, the spring that minimises the fluctuations of C_T^{2D} is different from the one that minimises the oscillations of α. In particular, Fig. 5.4 shows the amplitude of the fluctuations of C_T^{2D} (top) and α (bottom) for the blade section at $r = 0.75R$, for a range of values of Γ. It's shown that a spring that minimises the fluctuations

of α is stiffer than the spring that minimises the fluctuations of C_T^{2D}.

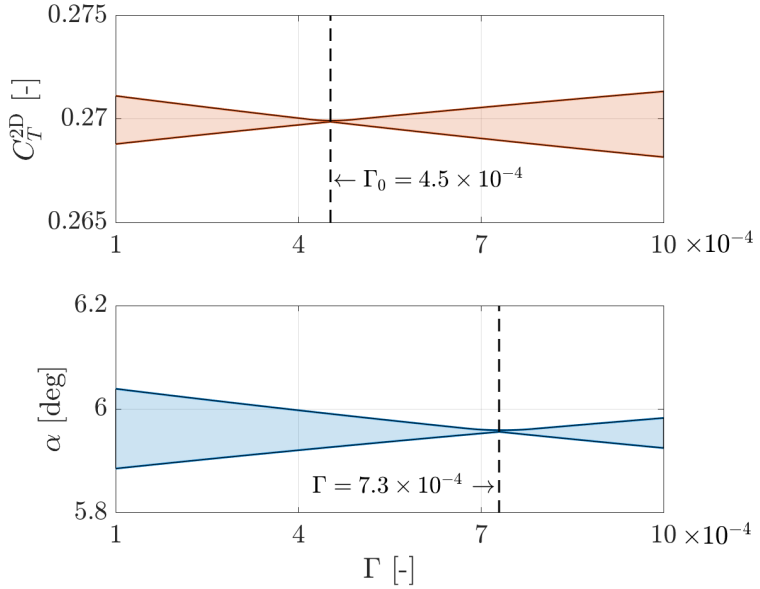

Figure 5.4: Fluctuations of C_T^{2D} (top) and α (bottom) for the section at $r = 0.75R$, for a range of values of Γ.

The results for 2D sections are summarised in Fig. 5.5, which shows the evolution of C_T^{2D} and C_P^{2D} during the revolution of the blade section at $r = 0.75R$ for different values of the non-dimensional stiffness Γ. The dotted lines on Fig. 5.5a show the blade azimuthal position. The maximum value $\Gamma = 10$ represents the condition of a rigid foil, where the spring becomes too stiff to bend and the loads on the section are not effectively alleviated.

In Fig. 5.5b, the range of Γ is narrowed to focus the reader attention around the optimal value $\Gamma_0 = 4.5 \times 10^{-4}$ which is highlighted by the dotted line. The optimal stiffness is represented by a slightly curved line. Therefore, the C_T^{2D} still exhibits small fluctuations throughout each revolution, although these fluctuations are negligible compared to the mean value and compared to fluctuations experienced by the rigid foil. The quasi-steady analysis shows that, for very low stiffness values, the variations of the thrust coefficient is

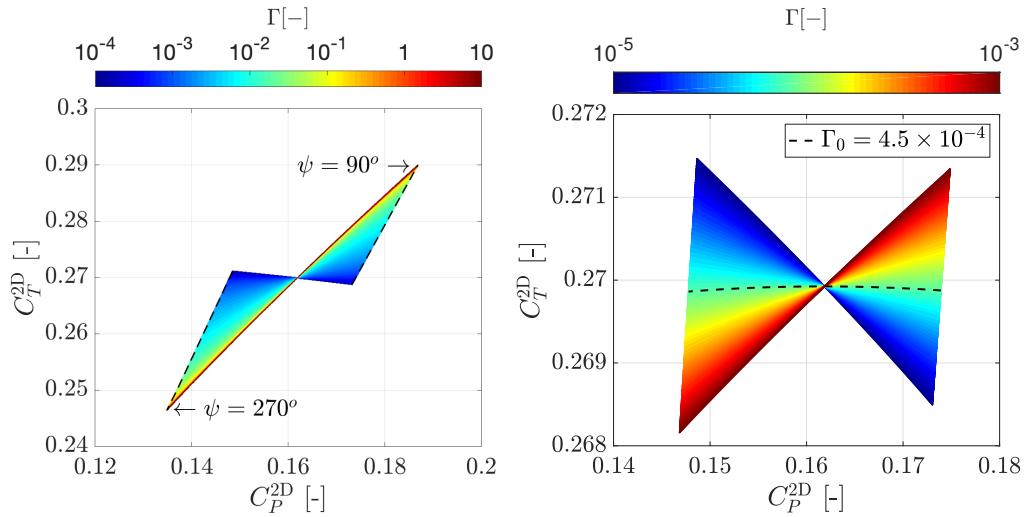

Figure 5.5: Variations of the power and thrust coefficients as the inflow angle varies through the rotation of the blade, (a) for a large range of values $\Gamma \in [10^{-5}, 10]$ and (b) around $\Gamma_0 = 4.5 \times 10^{-4}$.

reversed. The preload θ_0 is inversely proportional to Γ (Eq. 3.23), which means that the lower the value of Γ the higher needs to be the preload in order to balance the hydrostatic moment. Therefore, reducing the stiffness of the spring leads to high values of θ_0. C_P^{2D} always oscillates around the same value whilst the amplitude of the oscillations is slightly reduced.

5.2 Quasi-steady Analysis of the 3D Morphing Blade

The analysis presented in Section 5.1 is extended to the entire blade. A spring with quasi-steady non-dimensional stiffness (Eq. 3.49) $C_\kappa^{qs} = 6.0 \times 10^{-3}$ and quasi-steady preload angle $\theta_0^{qs} = 313$ deg leads to variations of the thrust coefficient at each section that are negligible, whilst the mean power generated in one revolution is unaffected. Figure 5.6 shows the angle of attack fluctuations over the area swept by the blade for a rigid (Fig. 5.6a) and a morphing blade (Fig. 5.6b). For each blade section, the values are normalised by the average angle of attack on that section. This representation allows to bet-

ter visualise fluctuations in the outward half of the blade since the sections operate at lower incidence, focusing on the blade area that contributes the most to the loads especially the root bending moment. Green regions show where the blade is operating at the average angle of attack, whereas red and blue regions indicate that the blade angle of attack is fluctuating above and below the average incidence respectively. The rigid case (Fig. 5.6a) shows an extended red region when the blade is between $0 - \pi$ (upper half), an extended blue region between $\pi - 0$ (bottom half), and a green region when the blade is horizontal at hub height, indicative of angle of attack and loads fluctuations. Conversely, the morphing blade (Fig. 5.6b) shows an extended green region across the entire rotor disk, indicating that the angle of attack is kept almost constant throughout the entire blade rotation along the entire blade span. At the very tip, the red/blue regions are inverted compared to the rigid case as noted and explained in Section 5.1 for the 2D analysis, and the fluctuations are not mitigated. This happens because the loads are very small due to the tip vortex, they contribute very little to the rotor thrust and the blade bending moment, hence they have very little importance in the blade optimisation process. The angle of attack inversion can be noted not only at the tip, but also at the blade root. Those sections are close to the hub, they have a short arm and they thus contribute very little to the RBM.

Figure 5.7 shows the thrust fluctuations over the area swept by the blade for a rigid (Fig. 5.7a) and a morphing blade (Fig. 5.7b). In particular, I plot the thrust coefficient of the rigid blade $C_T^{2\mathrm{D}}|_{\kappa\to\infty}$ and of the optimal morphing blade $C_T^{2\mathrm{D}}$ divided by the maximum sectional thrust of the rigid blade. The load is concentrated in the outer half of the blade and it drops at the tips and towards the hub. The high thrust experienced by the blade when $\psi = 90$ deg (Fig. 5.7a) is reduced thanks to the blade flexibility, whereas the lower thrust at $\psi = 270$ deg is increased.

The effectiveness of the blade flexibility is finally checked for the flapwise blade root bending moment shown in Fig. 5.8. Since the changes in the

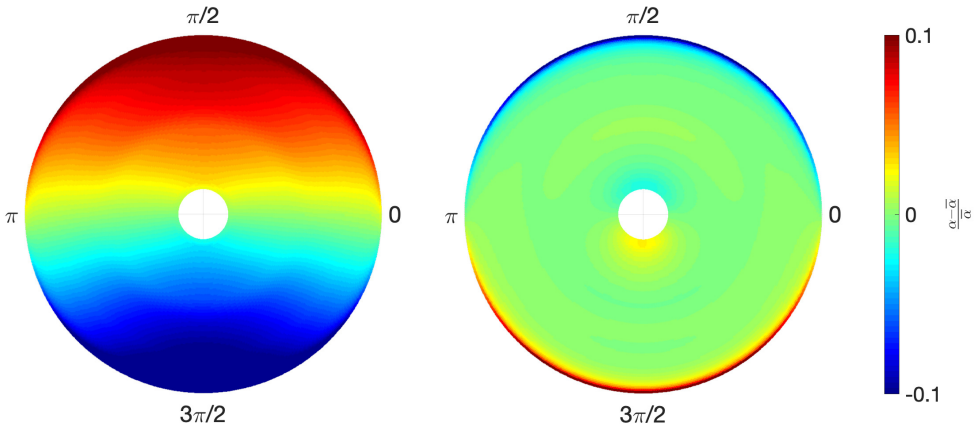

Figure 5.6: Map of the angle of attack fluctuations over the rotor disc for (a) a rigid blade and (b) a morphing blade. For each blade section, the values are normalised by the average angle of attack on that section.

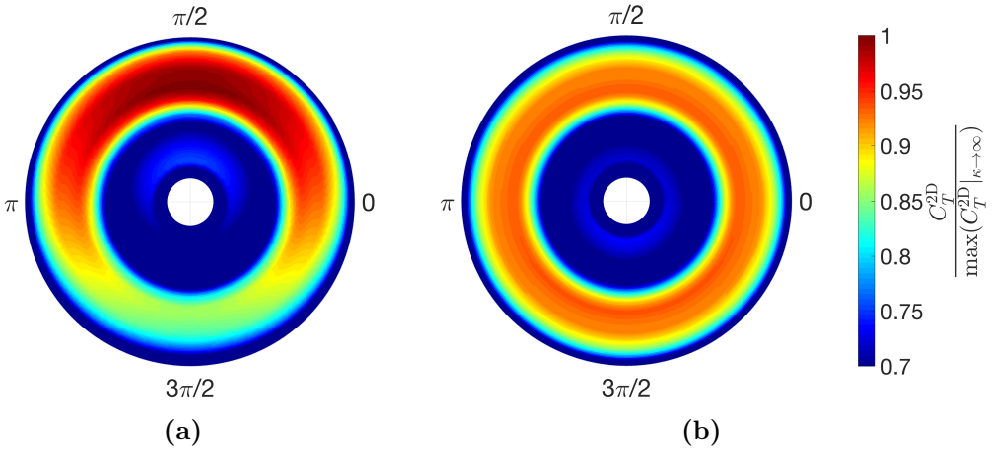

Figure 5.7: Map of the thrust coefficient over the rotor disc for (a) a rigid blade and (b) a morphing blade.

amplitude of the thrust fluctuations for the blade in the upward/downward positions are of opposite sign, the bending moment is kept nearly constant over each revolution. The results for the optimised system are resumed in Table 5.2,

	Optimal spring		RBM fluctuations ΔC_{RBM}	
	C_κ^{qs} [-]	θ_0^{qs} [deg]	% mean C_{RBM}	% reduction
Rigid	–	–	18	–
Morphing	6.0×10^{-3}	313	< 0.5	98

Table 5.2: Optimal quasi-steady results for the morphing blade model.

Compared to the 2D analysis, the performance is slightly lower. Each section experiences a different load fluctuation amplitude that requires a different blade deflection. As the morphing blade is optimised in a global fashion, it affects mainly the sections that experience stronger load fluctuations, and it is thus sub-optimal for the sections that contribute the least to the blade loads causing a performance reduction.

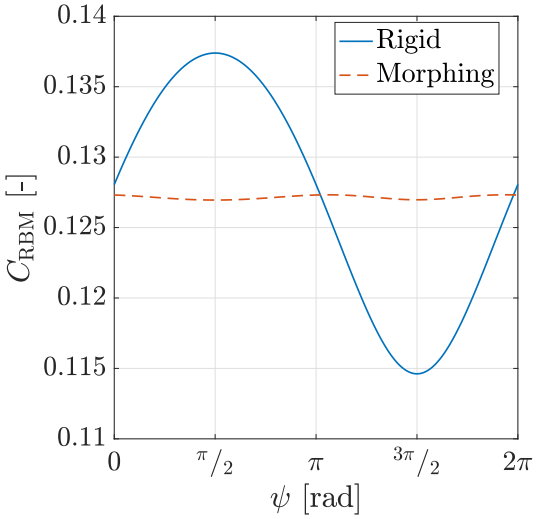

Figure 5.8: Quasi-steady analysis of the flapwise one-blade root bending moment C_{RBM}. The blade is equipped with a spring with $C_\kappa^{\mathrm{qs}} = 6.0 \times 10^{-3}$ and $\theta_0^{\mathrm{qs}} = 313$ deg.

5.3 Dynamic Analysis of the 3D Morphing Blade

I study to what extent the dynamics of the blade and the unsteadiness of the fluid loads affect the performances of the passive control system. From Eq. 3.45, I consider the centrifugal moment M_{c}, the hydrodynamic moment M_{dy} and that due to the mechanical damping of the blade $\mu\dot{\theta}$. The blade non-dimensional damping is initially set to $C_{\mu} = 10^{-4}$ (Eq. 3.49), which represents a negligible value. Its effect will be discussed in Section 5.4. Figure 5.9 shows that the effectiveness of the morphing blade in reducing the RBM oscillations is only marginally affected by the blade inertia and the unsteadiness of the flow. Figure 5.10 shows that the blade inertia and the fluid-induced damping have a small effect on the system effectiveness.

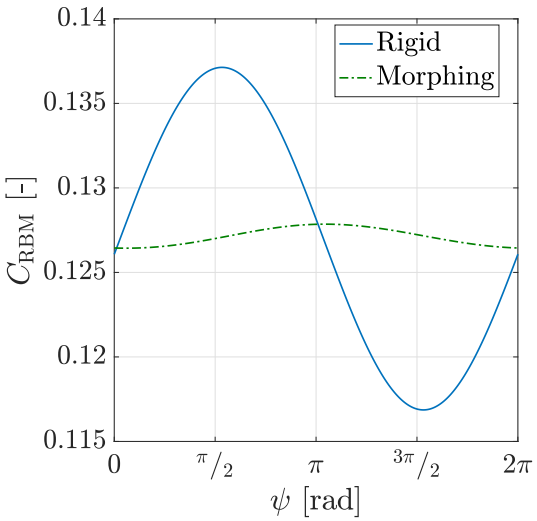

Figure 5.9: Dynamic analysis of the evolution of C_{RBM}. The blade is equipped with a spring with $C_{\kappa}^{\mathrm{dy}} = 1.1 \times 10^{-2}$ and $\theta_0^{dy} = 171$ deg.

Accounting for the additional moments, I find that the optimal non-dimensional stiffness and preload are $C_{\kappa}^{\mathrm{dy}} = 1.1 \times 10^{-2}$ and $\theta_0^{\mathrm{dy}} = 171$ deg. The optimal spring is stiffer than the one in the previous section because of the presence of unsteady loads. Table 5.3 shows the reduction in the

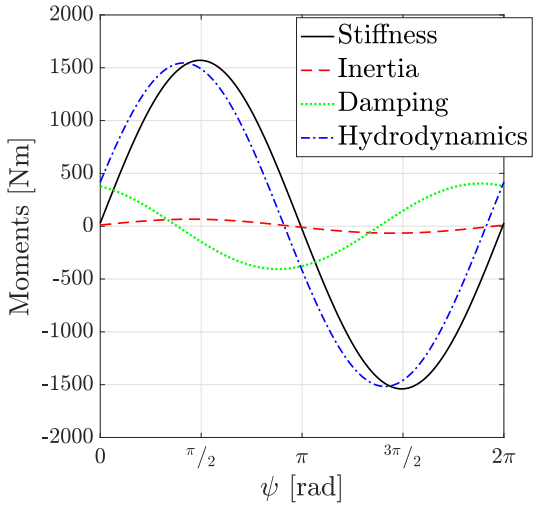

Figure 5.10: Dynamic contributions to the moment equilibrium of the blade, for $C_\kappa^{\mathrm{dy}} = 1.1 \times 10^{-2}$ and $\theta_0^{dy} = 171$ deg.

bending moment fluctuations.

As the optimal spring for the dynamic case is different than the optimal spring obtained for the quasi-steady model in Table 5.2, it is difficult to understand whether the difference in the performance are due to a different spring or to dynamic effects. For ease of comparison, in Table 5.3 I display two sets of results for the dynamic model and for the quasi-steady one (in parenthesis), both using the same spring optimised for the dynamic model. The performance estimated with the quasi-steady model is slightly lower than before as the spring is suboptimal. The system dynamics affect the blade performance only marginally, as the reduction of RBM fluctuations is only 5% lower compared to the best quasi-steady performance previously shown.

It must be noted that the mean power generated is the same as for the rigid blade.

	Optimal spring		RBM fluctuations ΔC_{RBM}	
	C_κ^{dy} [-]	θ_0^{dy} [deg]	% mean C_{RBM}	% reduction
Rigid	–	–	16(18)	–
Morphing	1.1×10^{-2}	171 (177)	2.6 (< 1)	93 (96)

Table 5.3: Optimal dynamic results for the morphing blade model. The numbers within the parenthesis refer to the quasi-steady analysis that employed the spring optimised for the dynamic case.

5.4 Effect of Blade Mechanical Damping

In this section, I consider the effects of the mechanical damping μ. Figure 5.11 shows the reduction of the fluctuations of the bending moment coefficient for a range of values of the stiffness coefficient C_κ and of the damping coefficient C_μ. In particular, the amplitude of the bending moment fluctuation ΔC_{RBM} is divided by the amplitude of the fluctuations for the rigid blade $\Delta C_{\mathrm{RBM}}|_{\kappa\to\infty}$.

The optimal working point for each curve is their minimum. When C_μ is large compared to the hydrodynamic damping, the efficacy of the morphing blade is poor. Conversely, for $C_\mu = 10^{-1}$ the system performance improves considerably, and the fluctuations of the blade root bending moment are reduced by 98%. Increasing the damping, the lowest point of each curve moves to higher values of C_κ, hence the optimal performance of the passive control system is achieved with stiffer springs. For high values of C_κ, all the curves in Fig. 5.11 collapse and converge asymptotically to 1. The system is not very sensitive to small changes in the spring stiffness, as the reduction in the ΔC_{RBM} does not vary significantly near the optimum.

The blade does not experience any resonance phenomena, and, even for negligible mechanical damping C_μ, the fluid acts as a damper, the motion of the blade is effectively damped. In fact, by considering the blade damping as a lumped parameter, it is possible to define a damping ratio as

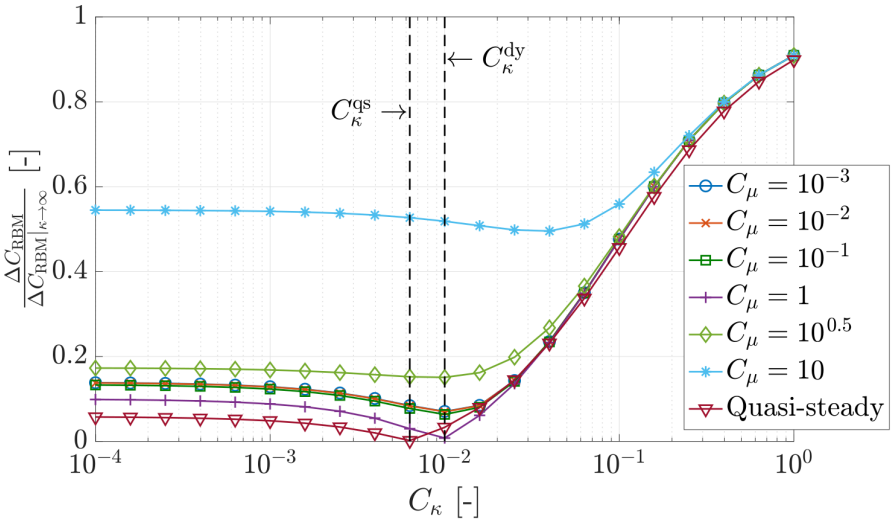

Figure 5.11: Normalised amplitude of the root bending moment for a range of values of C_κ and C_μ.

$$\zeta = \frac{C_{\mathrm{tot}}}{2\sqrt{J_{\mathrm{tot}} K_{\mathrm{tot}}}}, \tag{5.1}$$

where J_{tot}, C_{tot} and K_{tot} represent the inertia, the damping and the stiffness of the system respectively. In particular, J_{tot} is the sum of all the inertial terms in Eq. 3.46, C_{tot} is the sum of all the terms that multiply $\dot{\delta\theta}$ and K_{tot} is the sum of the terms that multiply $\delta\theta$, the damping ratio describes the coupled mechanical-hydrodynamic system. Similarly, I define the natural frequency of such system as

$$\Omega_N = \sqrt{\frac{K_{\mathrm{tot}}}{J_{\mathrm{tot}}}}. \tag{5.2}$$

For the range of values of C_κ considered, the natural frequency of the coupled system is always greater than 2.8 rad s^{-1}. Since the frequency of the load fluctuations is $\omega = 1$ rad s^{-1}, the blades are likely to experience no resonance. The damping ratio ζ changes with the spring stiffness, and at the minimum of each curve, it always takes values greater than 0.4. Therefore, the hydrodynamic contribution alone dampens the motion of the blade sub-

stantially. The effect of the damping can be observed in Fig. 5.12, which shows the blade motion amplitude $\Delta\theta$ over the same range of C_κ and C_μ. All curves converge for stiff springs, for which $\Delta\theta$ tends to zero. For very flexible springs, $\Delta\theta$ is never higher than 2 deg and it decreases for increasing damping values. On the other hand, the preload θ_0 is inversely proportional to the spring stiffness and increases rapidly from zero to more than 10^4 deg for $C_\kappa < 10^{-4}$.

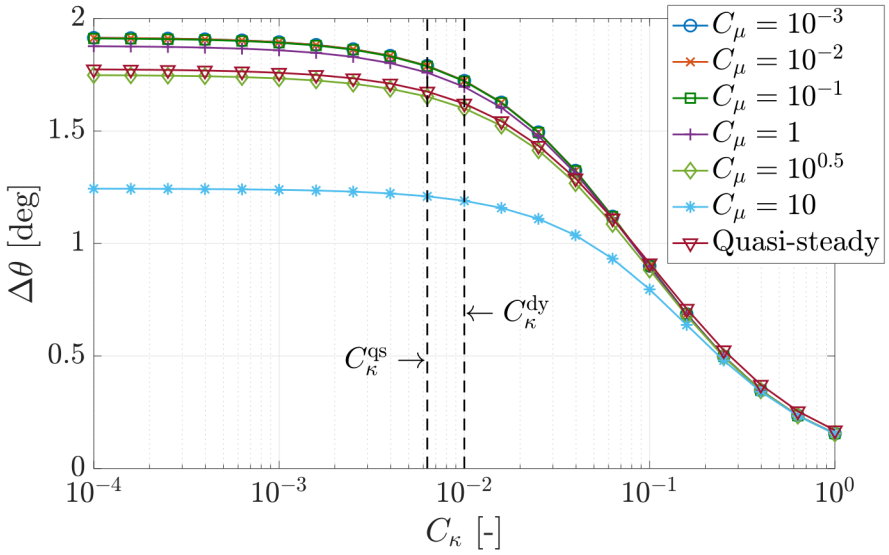

Figure 5.12: Evolution of $\Delta\theta$ for a range of values of C_κ and C_μ.

5.5 Morphing blade performance in real flow conditions

The performance of morphing blades is estimated again, this time using realistic inflow conditions, measured during a flood tide at the EMEC tidal testing site on 22 November 2014. Figure 5.13 shows the root bending moment coefficient C_{RBM} over 10 rotational periods, for a rigid blade and a morphing blade that has been optimised to minimise the fluctuation of C_{RBM}. Using a spring with quasi-steady non-dimensional stiffness $C_\kappa^{\mathrm{qs}} = 5.1 \times 10^{-2}$, and

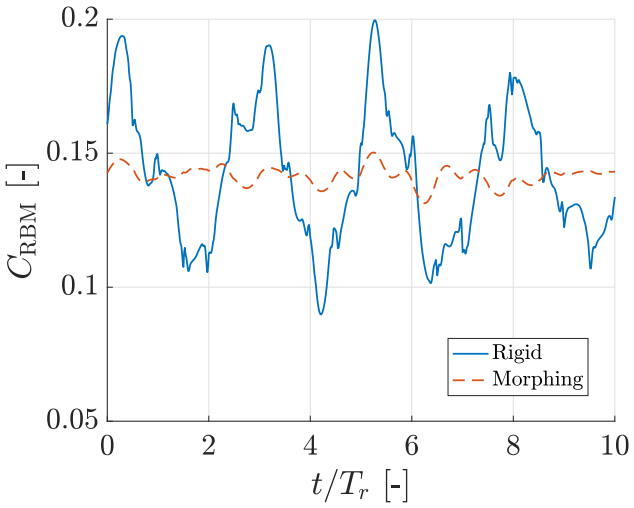

Figure 5.13: Root bending moment under real flow conditions from quasi-steady analysis of a rigid blade (blue line) and a morphing blade (red dashed line).

quasi-steady preload angle $\theta_0^{\mathrm{qs}} = 32$ deg, the fluctuations of the root bending moment are reduced by 82%, whilst the average power coefficient has decreased by 2%. Results are resumed in Table 5.4.

	Optimal spring		RBM fluctuations ΔC_{RBM}	
	C_κ^{qs} [-]	θ_0^{qs} [deg]	% mean C_{RBM}	% reduction
Rigid	–	–	104	–
Morphing	5.1×10^{-2}	32	13	87

Table 5.4: Optimal morphing blade when subjected to real flow conditions (quasi-steady analysis).

Figure 5.14 shows the root bending moment coefficient for a blade obtained from the dynamic analysis using the same spring, preload $\theta_0^{\mathrm{dy}} = 33$ deg, and inflow conditions approximated by Fourier series made of 100 components. The dynamic simulation predicts a reduction of the root bending moment fluctuations of 66% while the average power coefficient is 2% lower compared

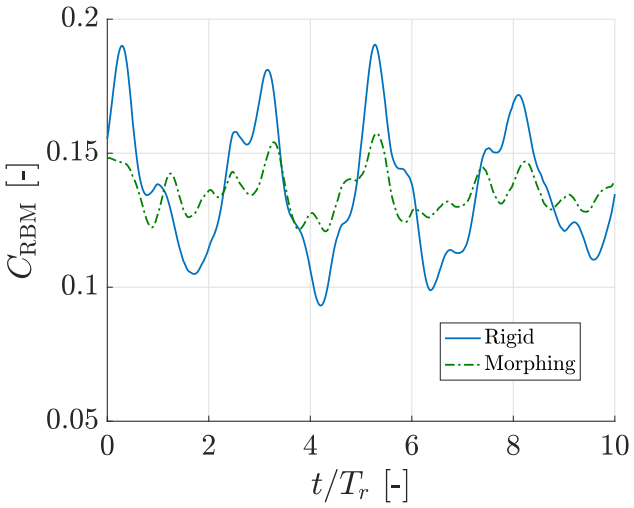

Figure 5.14: Root bending moment under real flow conditions from the dynamic analysis of a rigid blade (blue line) and a morphing blade (green dash-dot line).

	Optimal spring		RBM fluctuations ΔC_{RBM}	
	C_κ^{qs} [-]	θ_0^{dy} [deg]	% mean C_{RBM}	% reduction
Rigid	–	–	97 (99)	–
Morphing	5.1×10^{-2}	33	32 (17)	66 (82)

Table 5.5: Optimal morphing blade when subjected to real flow conditions (dynamic analysis). The numbers in parenthesis show the results obtained for a quasi-steady analysis when the inflow is Fourier-approximated as for the dynamic analysis.

to the rigid blade. Results are reported in Table 5.5.

The efficacy of the morphing blade to mitigate the fluctuations induced by real inflow conditions is slightly lower than that shown in Sections 5.2 and 5.3 for a modelled shear flow. The shear flow induces periodic fluctuations at the blade rotational frequency, whereas the real flow conditions induce load fluctuations over a wide range of frequencies. Since the load fluctuations are dominated by the high-amplitude, low-frequency waves, the optimal morphing blade is tuned to operate around that frequency. Therefore, the system is not as effective at alleviating the high-frequency, low-amplitude fluctuations,

as shown in Fig. 5.13. The unsteady simulations predict rigid blade fluctuations with lower magnitude due in part to the inflow which is approximated using 100 Fourier components, but mostly due to unsteady hydrodynamic effects, as already seen for the case of shear flow (see Table 5.3). The numbers in parenthesis in Table 5.5 are the quasi-steady results obtained using the Fourier-approximated inflow as for the dynamic analysis. They confirm that the performance of the morphing blade are affected mostly by unsteadiness of the flow, and that approximating the inflow signal with 100 Fourier components does not introduce significant error.

I have shown that morphing blades are capable of alleviating unsteady load fluctuations caused by shear flow and large waves. In my model, flow fluctuations are experienced by the blade as oscillations of the inflow speed and of the angle of attack, and a morphing blade mitigates the loads by inverting the sign of the angle of attack variations. The system reacts to inflow fluctuations regardless of the flow conditions that caused them. Hence, I believe that similar performance can be achieved for a wide range of unsteady flow conditions, including turbulence, yaw misalignment, wakes of upstream turbines, and the proximity of other devices. As the frequency of the fluctuation increases, such as for small-scale turbulence, the inertia of the blade leads to a reduction of the system efficiency. Moreover, the low-order model is not capable to consider the effect of high-frequency flow fluctuations with a period of the order of $c/(\omega R)$, such that the flow cannot be considered uniform along the chord. In such cases, a more sophisticated model should be used.

6

Experimental method

Given the promising prediction of the low-order code, I decided to perform proof of concept experiments using a 1:15 scale model turbine available at the FloWave Ocean Energy Research Facility (in short FloWave).

I originally envisaged the passive-pitch system as an analytical simplification of morphing blades (see Section 3). In its essence, the system provides a degree of flexibility to the blade which can bend to mitigate onset flow fluctuations. The analytical, low-order model is based on several assumptions that allow to strip the model down to the essential physical phenomena. The beauty of this approach is that it avoids unnecessary complexities and that results can be extended to different scenarios, as long as they share the same underlying physics. However, if the difference between a passively pitching blade and a morphing blade is negligible from an analytical standpoint, it becomes substantial when it comes to experimenting with physical models. Experiments cannot be deprived of all the complexities of real world physics, and the significance of test results is often limited to the investigated case. Although a passive-pitch system is still indicative of the potential of morphing blades, ad-hoc experiments shall be performed to validate this claim. To stress the philosophical difference between analytical and experimental methods, in this chapter I will refer to the system exclusively as "passive-pitch" rather than "morphing".

The objective of the experiments is to prove that the passive-pitch system allows to reduce the fluctuations of the thrust and of the root bending moment.

In the following paragraphs, I will describe the facility where I conducted the experiments, the design of the blade model and of the novel passive-pitch system, some issues that arose when assembling the model and how I solved them, the test programme, and experimental issues encountered while testing.

6.1 The FloWave facility

FloWave, previously known as FloWave TT, allows combined wave and current testing in any relative direction. The facility was inspired by an original design by Salter [185], it was built using funds from the UK Engineering and Physical Sciences Research Council (EPSRC) and it was ultimated in November 2013 [103].

Figures 6.1 show the tank that features a 25 m diameter basin, 2 meter working water depth, and a liftable floor to allow for installation of models. There are 28 bidirectional impellers that can generate current speeds upwards of 1.6 m s^{-1} [163]. The tank, which is optimised for waves of around 2 s period, is equipped with 168 wave makers that generate waves from any relative directions. The facility offers the the ability to model metocean conditions at a typical scale between 1:15 and 1:40 [103]. The tank features a sheared velocity profile that corresponds to a 1/15 power law for any input velocity [163].

6.2 Turbine model

FloWave made available a 1:15 scale tidal turbine which had been developed to acquire experimental data to validate numerical models and to make predictions of turbines' performances. The turbine has a standard design and is representative of many full-scale prototypes [186]. It's a bottom-mounted device with three blades on a horizontal axis rotor. The turbine has 1.2 m rotor diameter (1:15 geometric scale) with 0.12 m hub diameter and effective blade length of 0.54 m. The turbine features a direct-drive transmission,

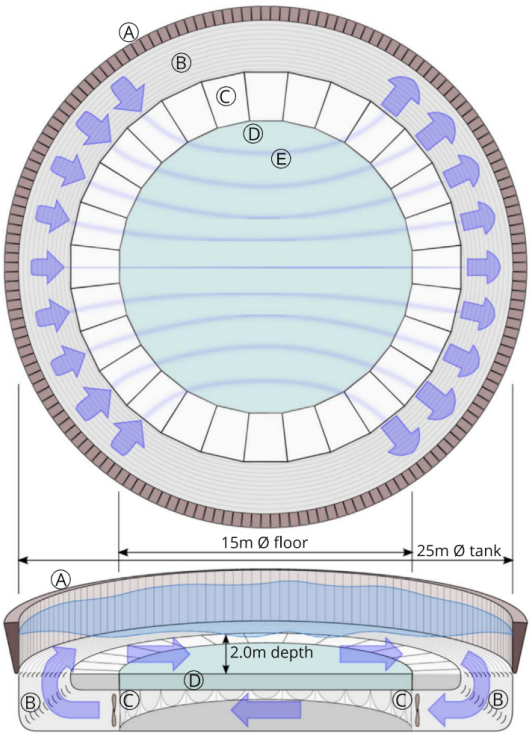

Figure 6.1: Schematic of FloWave in plan and oblique section showing: (A) Wavemaker paddles around circumference (168 Nr) (B) Turning vanes and flow conditioning filters (C) Current drive impeller units (28 Nr) (D) Buoyant raisable floor (15 mØ) below test area (E) Idealised streamlines of flow across tank floor. (Noble et al. [163])

and a brushless permanent magnets servo generator, which can be operated as a motor and that can be speed-controlled or torque-controlled, meaning that the control system will keep either constant rotational speed or constant torque. Details of the instrumentation of the turbine are reported below, in Section 6.5. More details can be found in Payne et al. [187].

6.3 Passive-pitch blade model design

Since the turbine was available in FloWave, I designed the blade and the passive pitch system using Autodesk Fusion360. Figure 6.2 shows a comparison of the blade system CAD model (hub and tower models provided by FloWave staff) and the finalised experimental model installed on tank floor. While the passive-pitch system represent a novelty and it is designed from scratch, the blade is adapted from the design of the Tidal Generation Ltd. (now Alstom) 1 MW turbine [174] (see Section 3). The passive-pitch system is a load control mechanism added to a conventional, rigid blade to represent the blade flexibility. Therefore, I will describe the blade and the passive-pitch system separately to highlight the novelty that lies in the latter. Since I use an existing turbine model, additional constraints are set on the size of the blades and of the passive-pitch system. The blades are attached to the hub through the metal flexures that serve also as bending moment transducer. These represent the interface between the existing turbine and the passively-pitching blades.

6.3.1 Blade design

Conventional blade design typically encompasses the selection of airfoil family, the optimisation of the chord and twist distribution, and the determination of the minimum thickness-to-chord ratio to withstand the estimated loads [104]. Since I adopted an existing design, all the blade parameters were predetermined except the relative position of each section with respect to the pitch axis. In particular, for each section, the pitch axis was placed at a distance from the leading edge equal to 10% of the local chord value (Fig. 6.3).

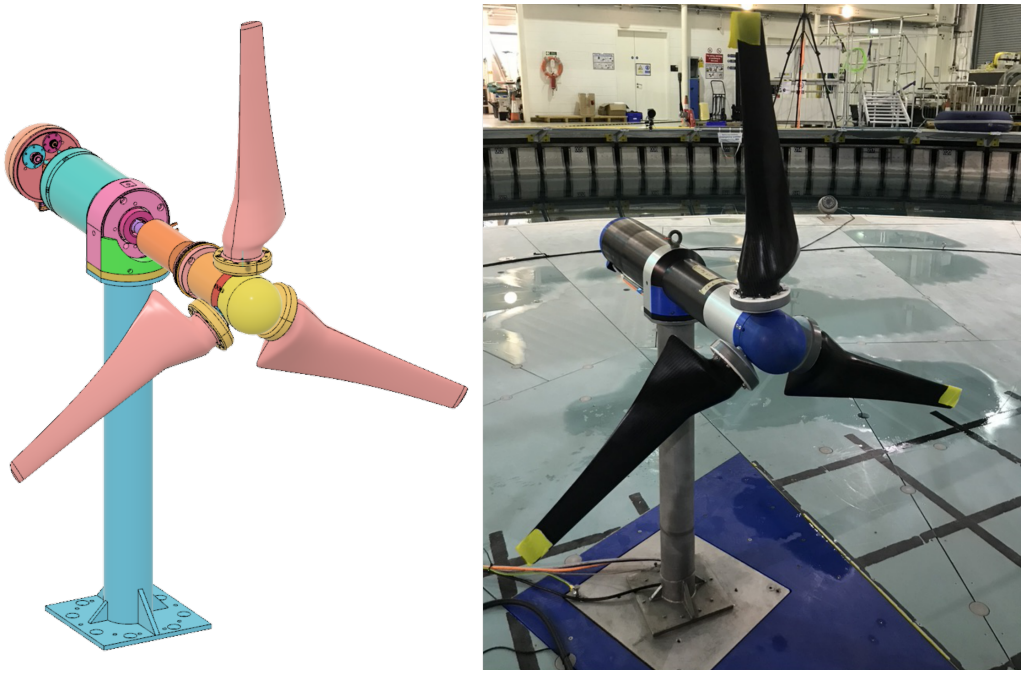

Figure 6.2: Passive-pitch blade design (left) and realised model on the tank floor (right).

Hence, all sections where shifted backwards from the conventional quarter-chord position, except near the root, where the sections were shifted forward to make space for the passive-pitch centred on the pitch axis.

The shape and relative position of the blade sections were informed by the low-order code, the data thus imported in Fusion360 and the blade was extruded through the sections following traced guidelines. The objective was to obtain a smooth blade shape, with no sharp edges and no creases along the blade span to prevent spanwise flow separation. If the 3D-blade showed an irregular shape, the size and the relative position of the sections was modified in Matlab and the process was repeated. This iterative process allowed to generate a smooth blade with enough space to embed the passive pitch system near the root, but also to keep an accurate record of the blade geometry. Figure 6.3 shows the final blade design, obtained after a few design iterations. I summarised the blade dimensions in Figure 6.3, indicating for each section the distance of the pitch axis from the leading edge.

section	radius [m]	chord [mm]	pitch axis position [%]
20	0.60	40	0.1
19	0.59	53	0.1
18	0.56	55	0.1
17	0.54	58	0.1
16	0.51	60	0.1
15	0.48	63	0.1
14	0.47	67	0.1
13	0.43	70	0.1
12	0.40	75	0.1
11	0.38	79	0.1
10	0.35	84	0.1
9	0.32	90	0.1
8	0.30	96	0.1
7	0.27	104	0.1
6	0.24	112	0.1
5	0.22	121	0.1
4	0.19	137	0.15
3	0.16	155	0.20
2	0.14	171	0.23
1	0.11	107	0.50

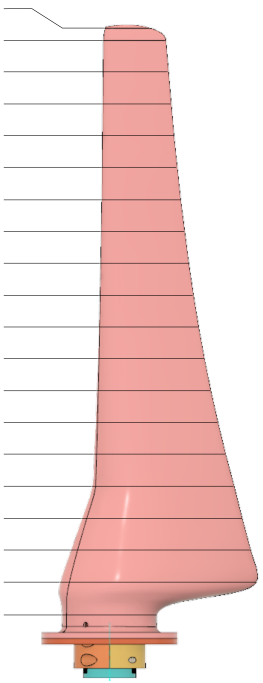

Figure 6.3: Blade dimensions. Each section is numbered from 1 (root) to 20 (tip) and is described by the position along the blade span, or radius, the chord length and the position of the pitch axis with respect to the leading edge as a percentage of the chord.

Near the root, the aerodynamic profile blended into a cylindrical shape, where the passive-pitch system was then lodged, and it featured a flat flange with 6 mm holes to attach the passive-pitch system and align it to the blade.

The model turbine at FloWave was originally equipped with full, aluminium blades. Tidal turbines typically feature blades made of composite materials for considerable savings in cost and weight. Composite materials are shaped into thin shells rather than full volumes. This allows the blade to be filled with water to reduce the periodic loads experienced by the blades due to buoyancy and their own weight [172]. Since the weight and material cost scale with the volume of the blade (for full metal blades) or the surface area (for shell-like blades), at 1:15 scale, the choice of material is not crucial because the potential cost and weight savings for a one-off production of blade prototypes are small. Moreover, the inertia of the blade scales with the 4-th power of the geometric scale, and the model blade dynamics will differ from the full-scale device regardless of the blade material that has thus little impact on the final blade design. I decided to make empty-shell carbon fibre blades that can be filled with water to minimise the effect of gravitational and buoyancy loads, as for full-scale devices.

To manufacture the blades, I contracted Piran Advanced Composites, a company based in WadeBridge (Cornwall, UK) specialised in the manufacturing of composite aerodynamic components for the aerospace industries, including UAV airframes and propeller blades. The blades were manufactured using a female epoxy mould to accurately recreate the external blade geometry and to ensure smooth surface finish. The shell thickness was 3 mm thick, obtained by overlaying $+45/-45$ degree carbon fiber fabric to a core made of unidirectional fibers extending along the blade span. This layup granted significant bending strength, which typically constitutes the main structural limitation, but also great torsional strength. The flange at the root was made 5 mm thick and it featured 12 holes to bolt the blade to the passive-pitch system. Figure 6.4 shows the manufactured blades.

Figure 6.4: Overview of the blade pressure side (left) and of the trailing edge (right). The bottom of both pictures shows the perforated flange used to bolt the blade shell to the passive-pitch system.

6.3.2 Passive-pitch system design

The passive-pitch system is made of several parts realised in different materials. Figure 6.5 shows all the different parts of the system. The mechanism is based on a torsional spring wound on a shaft which controls the pitch angular position and motion of the blade relative to the hub.

The system is attached to the blade through a cone-shaped part that has a matching flange. The shaft is glued inside the narrow tip of the cone. The rotation of the shaft, of the cone and of the blade, is allowed by two sets of bearings held inside a split casing which is bolted to a thin disk called the "angular plate". The whole system is connected to the turbine through the angular plate that is bolted onto the bending moment flexures on the hub. Blade, cone and shaft can rotate with respect to the casing and the angular plate which are fixed. The spring legs are inserted into holes on the cone and on the casing, thus controlling the relative motion. The cone was manufactured in carbon fiber by Piran Advanced composites.

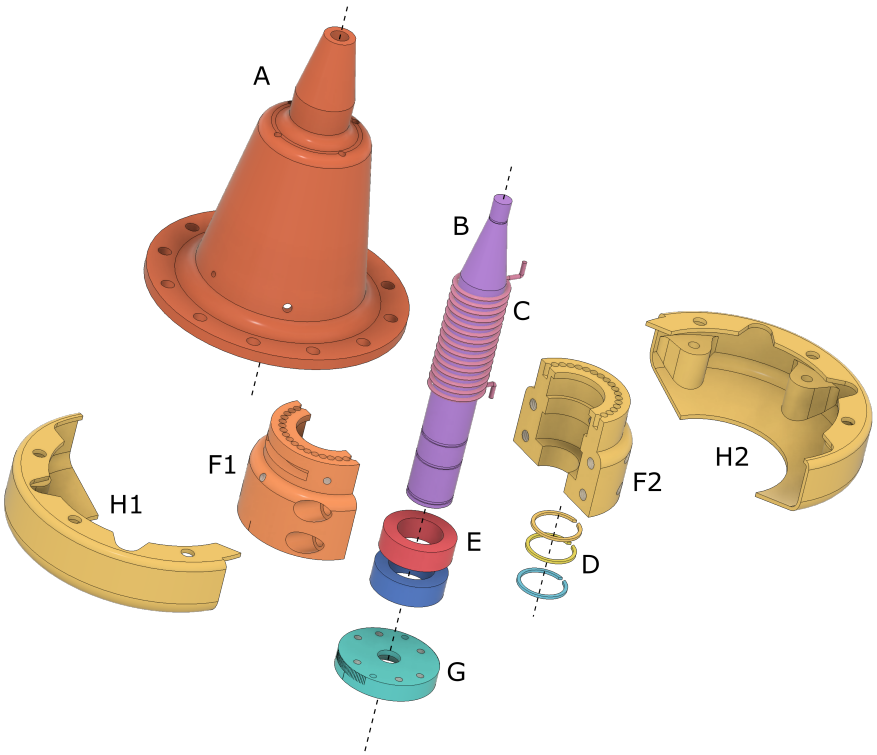

Figure 6.5: Passive-pitch system components: A) flanged cone; B) shaft; C) torsional spring; D) circlips to retain E) bearings; F1, F2) casing halves; G) angular plate; H1, H2) fairing.

The angular plate, the casing and the shaft were machined out of high-strength T9-6026 aluminium (yield strength $\sigma_{\mathrm{Al}} = 330$ MPa, Young modulus $E_{\mathrm{Al}} = 69$ GPa) within the School facilities. I bought off-the-shelf rubber sealed double-row ball bearings from Simply Bearings Ltd, and the torsional spring was a custom design commissioned to The Active Spring Company Ltd and made of galvanised carbon steel. A plastic fairing was 3D-printed within the School laboratories to improve the aerodynamics of the system where the flanges and the passive-pitch system are exposed to the flow.

6.3.3 Torsional spring design

As a spring stiffness is optimal only for a specific flow condition, I commissioned several springs with stiffnesses in the range $3.27 - 36.76$ Nmm deg^{-1} to have more freedom in the design of the experimental conditions. I de-

termined the required spring properties using the low-order model. I simulated the scaled model turbine operating at $\lambda = 7$ and a nominal flow speed $U_\infty = 0.8$ ms^{-1}, and I performed a parametric study of the performance of the passive-pitch system.

I used the spring with stiffness 4.2 Nmm deg^{-1}. The predicted preload at $\lambda = 7$ and a nominal flow speed $U_\infty = 0.8$ m s^{-1} was 450 deg. I chose this spring because the preload is not too high with the risk of deforming the spring or getting a strongly non-linear response, but high enough that any error during the installation would cause very little change in its moment reaction. During the first day of testing, I noticed that the spring legs slipped out of placed effectively reducing the preload angle to 275 deg. Before the following tests with preloads 450 deg and 550 deg, I pulled the spring coils apart to increase the axial length such that once installed it would be slightly compressed and the legs would be held in their sockets. This strategy was successful to prevent the spring legs from slipping out, however, the springs resulted slightly bent along their axis, causing friction against the shaft. In the result section, I will discuss the effect of friction on the performance of the passive-pitch system.

6.3.4 Model assembly and operating principle

Since the torsional spring needs to be changed depending on the flow condition, I designed the system to be modular to be taken apart. With reference to Fig. 6.5, the system is assembled as follows. The spring (C) is slid onto the shaft (B) and its upper leg is inserted into a hole on the cone (A). A circlip (D) is fixed in a groove on the shaft, to constrain the first bearings set (E). A second circlip is applied after the bearings, a second bearings set is inserted on the shaft and a third circlip locks it on the shaft. The casing halves (F1, F2) are inserted in the cavity between the cone and the shaft, and they are thus pushed onto the bearings. While inserting the first half-casing, the bottom leg of the spring is inserted in a hole on the casing. Four bolts are inserted from the side of the casing to pull the two halves shut. The angular plate (G) is bolted to the casing, and the cone is bolted to the blade. The whole system can thus be installed on the turbine hub. The fairing (H1,

H2) is the last part to be installed, its two halves are slid on the blade-cone flange and bolted to it. Figure 6.6 shows the assembled system.

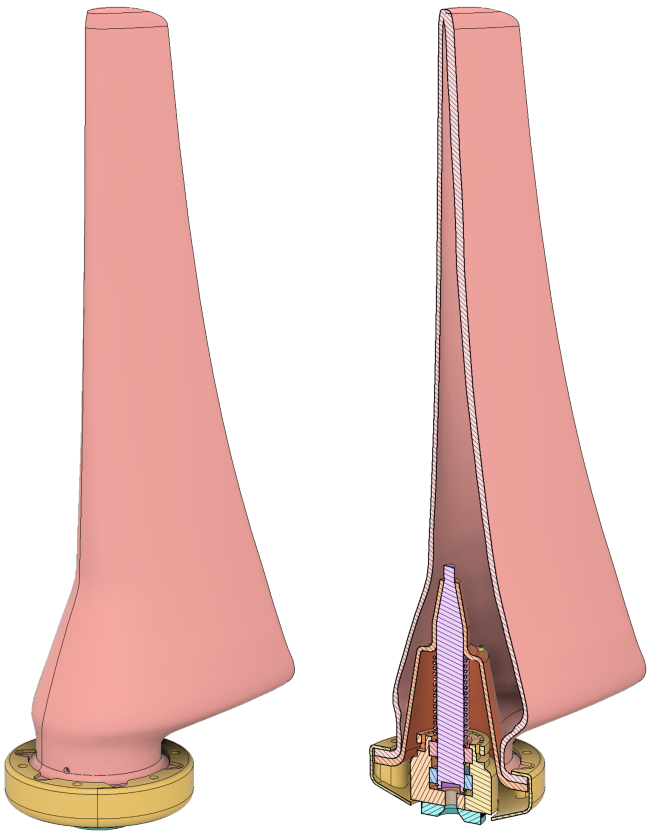

Figure 6.6: Blade and passive-pitch system assembled (left) and section of the assembly (right).

The spring preload is the spring deflection required to balance the average fluid moment for a given flow condition. The spring is preloaded in two ways. A rough adjustment is obtained by inserting the top leg of the spring in one of the holes in the carbon fibre cone, which are at 45 deg distance. A fine tuning is obtained by inserting the bottom leg of the spring in one of the holes on top of the casing. The holes are placed at an angular distance of 10 deg which grants an accuracy of 5 deg. It was not possible to achieve a higher degree of accuracy as the holes would have merged together. However, by using more

flexible springs, higher preloads are required to balance the fluid moments (Section refch2, Eq. 3.28), hence, the relative error on the preload angle is reduced. For instance, a preload of 400 deg allows can be achieved with less than 2% uncertainty. The torsional spring is preloaded before installing the system on the turbine, by manually twisting the casing with respect to the blade. At reaching the desired number of turns, a pin is inserted through the blade wall, which is lodged in a slot on the casing. The slot is 80 deg wide, to allow oscillations of the blade up to 40 deg during the turbine operations, but at the same time it prevents the preloaded spring from unwinding. After insertion of the pin, since there is no hydrodynamic moment to balance the spring reaction, the blade turns slightly until the pin hits the side of the slot. Instead, during the turbine operation, the average hydrodynamic moment balances the spring preload and it keeps the pin at the centre of the slot. The blade is thus free to oscillate passively in both directions in response to flow fluctuations. To test a rigid, conventional blade, a screw is inserted through an additional hole locking the blade to the casing, thus preventing any rotation around the pitch axis.

6.4 Structural considerations on the passive-pitch system

To verify the structural robustness of the blade and passive-pitch system, I performed the analysis outlined in Fig. 6.7. The procedure was performed for all load-carrying components before commissioning. Details of the analysis for each component are presented below.

6.4.1 Harshest flow condition and maximum design loads

The blade experiences the highest operating loads at $\lambda = 8$, at a nominal flow speed $U_\infty = 0.9$ m s^{-1} and no waves (see Section 6.6). However, in case the turbine generator would loose connection to the grid, the turbine would accelerate up to $\lambda = 9.5$, where the turbine would be free-spinning,

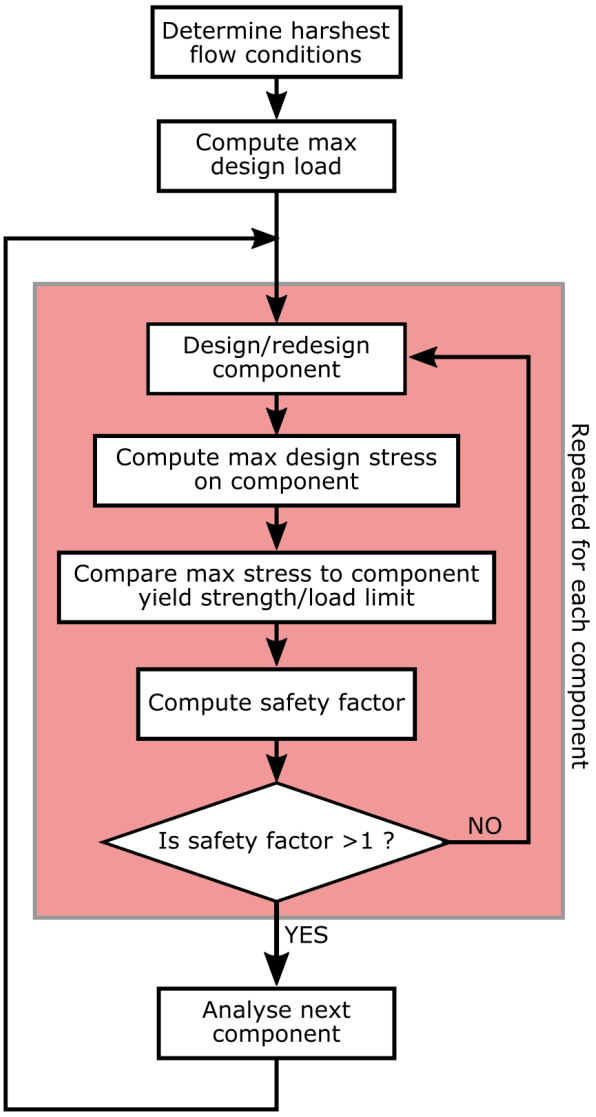

Figure 6.7: Outline of structural analysis of blade and passive-pitch system.

generating zero torque. I estimated the loads on the blade using the low-order model, and I used the loads generated at $U_\infty = 0.9$ m s^{-1}, $\lambda = 9.5$ and no waves as the maximum design loads for the blade and the passive-pitch system. The maximum root bending moment was the primary driver of the structural design.

Figure 6.8 shows the distribution of the bending moment along the blade span computed for a range of tip speed ratios, at $U_\infty = 0.9$ m s^{-1}. The bending moment increases rapidly near the tip, where the load F_N normal to the rotor is concentrated, and it increases linearly near the root as those sections contribute very little. The maximum bending moment at the blade root is $M_{\mathrm{RB,max}} = 42.4$ Nm.

6.4.2 Blade and composite components

Structural blade design is typically performed using beam theory as a first, rough indication of the structural requirements, whereas the final design is validated using more sophisticated methods, such as Finite Element Analysis (FEA). However, given the time constraints of the project, I determined the blade structural design using beam theory and conservative safety factors. The method is fast and well suited for multiple design iterations. Since the cost of one-off batch of blades was limited, the additional costs from using more materials were negligible and the manufacturing process was faster, as small defects were compensated by conservative safety factors.

The stresses induced by the bending moment are determined by the diameter of the root section and the thickness of the blade shell. Knowing that the root section has a circular shape, the bending stress experienced by the blade material is computed as

$$\sigma_{\mathrm{B}} = \frac{M_{\mathrm{RB}}\, y}{I_y}, \tag{6.1}$$

where I_y is the second moment of area with respect to a reference system

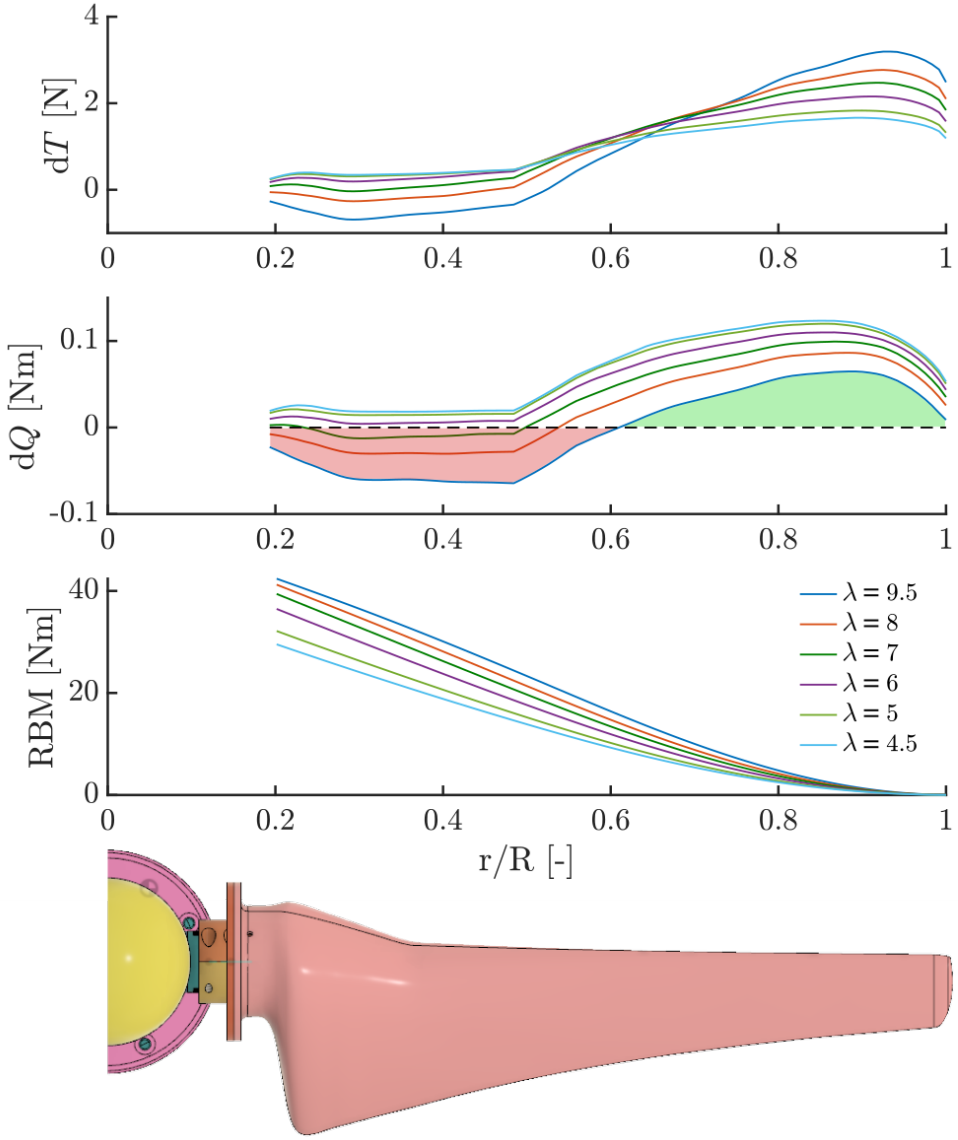

Figure 6.8: Estimated blade loads at $U_\infty = 0.9$ m s^{-1} over a range of tip speed ratios λ. From the top, showing the distribution of thrust (dT) and torque (dQ) along the blade span, and the bending moment (RBM). At $\lambda = 9.5$, the blade experiences the highest bending moment and zero torque: the positive torque contributions (green-shaded) are cancelled by the negative contributions (red-shaded).

centred with the circular section, and y is the radial distance of the blade shell from the centre of the section. The second moment of area is computed as

$$I_y = \frac{\pi}{4}(y_{\text{ext}}^4 - y_{\text{int}}^4) \tag{6.2}$$

with y_{ext} and y_{int} the distances of the outer and inner surface of the blade shell from the centre of the section respectively, and their difference being the thickness t_h of the blade shell. The blade structural parameters are reported in Table 6.1 assuming a wall thickness of 3 mm.

y_{ext} [mm]	40
y_{int} [mm]	37
t_h [mm]	3
y [mm]	38.5
I_y [mm^4]	5.4×10^5
$\sigma_{\text{B,max}}$ [MPa]	3.0

Table 6.1: Structural parameters of the blade root section.

The maximum bending stress $\sigma_{\text{B,max}} = 3.0$ MPa is then compared with the maximum stress admissible in a 3 mm thick carbon fibre sheet to determine if it's thick enough to sustain such loads. As opposed to metals, carbon fiber composites have structural properties that depend greatly on the orientation of the fibers of each sheet and the resin used. Single, unidirectional fibers have a tensile strength of over 2000 Mpa, whereas a plain weave carbon fibre fabric embedded in epoxy resin can sustain stresses greater than 460 Mpa [188]. In all cases, the tensile strength for the suggested 3 mm thick blade shell is 150 times higher than the maximum bending stress, providing a very large safety factor.

A similar calculation was performed for the bottom section of the carbon fiber cone, since it is slightly smaller than blade root section but it transfers the same loads. The maximum bending stress in this case is $\sigma_{\text{B,max}} = 3.9$ MPa which is also much lower than the tensile strength of the part.

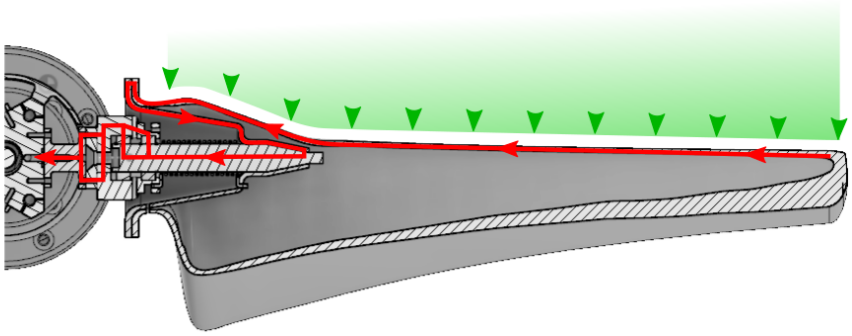

Figure 6.9: Load path from the blade to the hub. The hydrodynamic pressure (green arrows) loads the blade which transfers the stresses (red arrow-path) to the inner cone. The stresses climb up the cone and are transferred to the shaft, they pass through the bearings and the casing and are finally transferred to the hub.

6.4.3 Shaft and casing

The loads are transferred from the blade to the cone through the bolted flange. Through the glued joint they pass to the shaft, then through the bearings to the casing, and eventually to the hub flexures where they are measured and transferred to the drivetrain. Figure 6.9 shows the load path.

The shaft represented the most critical components due to its 20 mm narrow section. Using the same approach as for the blade (Eq. 6.1), I computed the maximum stress $\sigma_{\mathrm{B,max}} = 63.0$ Mpa transferred through the shaft, and I verified that it was 5 times smaller than the yield strength of the aluminium alloy ($\sigma_{\mathrm{Al}} = 330$ MPa). The casing, made of the same material but having a much larger section, was not an issue. The ISO 4762 (DIN 912) steel bolts that held the two half of the casing together have a yield strength greater than 1000 MPa. The glued joint between the carbon fibre cone and the aluminium shaft has a circular section which is wider than the shaft alone, hence it structurally solid. Moreover, the joint is further away from the root, and it experiences lower bending moments and lower stresses. The joint itself could be a weak point if the glue gives way, but it was thoroughly reinforced to prevent any failure.

6.4.4 Bearings

The bearings had a declared static and dynamic radial load limit of 4850 N and 5800 N respectively[1]. To transfer the maximum estimated moment of 42.4 Nm, the bearings are placed at 18 mm distance from the respective mid-section, resulting in a maximum radial load of 2355 N, well within both static and dynamic ranges. The radial load due to the blade bending was the main loading mechanism on the bearings, with a small axial load contribution due to the centrifugal forces (the blade, once filled with water was neutrally buoyant hence the axial load due to gravity and buoyancy was negligible). The centrifugal force F_c is computed as

$$F_c = m\omega^2 r_{\mathrm{CG}}, \tag{6.3}$$

where m is the mass of the blade filled with water, ω the rotational speed and r_{CG} the spanwise position of the centre of mass of the blade. The blade mass is about $m = 1.7$ kg, and centre of mass is approximately at $r_{\mathrm{CG}} = 23.4$ cm from the rotor axis. At a nominal flow speed $U_\infty = 0.9$ m s^{-1} and tip-speed ratio $\lambda = 9.5$, the blade is rotating with $\omega = 14.25$ rad s^{-1} and the centrifugal force is thus $F_c = 80.7$ N. The manufacturer did not specify the axial load limit for the purchased bearings, but radial ball bearings can usually sustain axial loads as little as $25-50\%$ of the radial load range. Since the expected axial load is less than 2% of the static radial load limit, these bearings are safe to use. All blades and passive-pitch systems were assembled and strength-tested before the experiments to validate the strength of the system under the highest design loads.

For the present experiments, the blade and passive-pitch system are sufficiently robust, with the most critical parts being the bearings and the shaft, which present the smallest safety factors of two and five respectively. In the

[1]Ball bearings are typically used for dynamic applications at high rotational speed where each ball experiences the load periodically but for a very short time. The load is virtually distributed over all the balls and the entire rail granting a high load limit. Instead, a static load is applied always on the same balls and and the same part of the rail which can result in local deformation, or pitting, at loads lower than those it could sustain dynamically.

future, if the blades had to be tested in harsher flow conditions with higher loads (e.g. large waves), the shaft could be replaced with a high strength steel part, and the casing could be redesigned to allow a greater distance between the bearings to reduce the load.

6.5 Instrumentation

The turbine provides load measurements of the thrust and the torque of the rotor, and the root bending moment of each blade. The thrust and torque transducer was custom made by Applied Measurements Ltd. (www.appmeas.co.uk), and is placed very close to the rotor, upstream of water seals, to provide high quality data free from parasitic friction along the drivetrain. The transducer load rating was determined as twice the maximum loads predicted with a BEMT code, that correspond to 150 Nm torque and 1950 N thrust [187].

The bending moment transducers are embedded in the structural components that connect the blades to the hub. The transducers were designed and manufactured in-house, and then supplied to Applied Measurements Ltd. for strain gauging, waterproofing and calibration.

The blades angular position is measured providing both angular displacement and rotational speed of the blades. An encoder is fitted on the generator, and its signal is used both to record the angular position and the rotor speed with the data acquisition system, and as input for the speed control loop.

The flow velocity was measured using the Vectrino measurement system. The device measures all three velocity components using acoustic doppler velocimetry. The probe features a transmitter which generates a beam of acoustic waves at a fixed frequency. The waves are reflected by scattering material suspended in the water and three receiving transducers record the distorted frequency. The frequency shift between the transmitted and recorded waves can thus be converted into a velocity value. The probe was placed 1.37 m in front of the model, causing negligible interference with the

flow, at a 1.47 m from the seabed. The tests were started after the a stable current velocity had been reached, approximately five minutes from the moment the tank motors were started [163].

The data acquisition system is based on a National Instruments CompactDAQUSB chassis (cDAQ-9174). The encoder signal generated by the generator is logged using a digital I/O module (NI 9401). Thrust, torque and RBM are measured with strain gauge bridge amplifiers which generate a current signal logged with an analogue input module (NI 9203) [187].

6.6 Test programme and execution

I conducted the experimental campaign mid November 2020. The tests occupied three of the five days spent in FloWave, with the remaining time dedicated to installation and setup. The research hypotheses were that the passive-pitch system allows to reduce the fluctuations of the thrust and of the root bending moment for a turbine operating in shear flow, and that the low-order model can make reliable prediction of the loads.

I considered testing the model in current and large waves, to observe larger load fluctuations and potentially a greater mitigation of such loads, but I decided to test only with shear current for two reasons. First, the low-order model that I used to predict the turbine performance draws the blade lift and drag data from look-up tables (Section 3), and that data was limited. In particular, large waves can cause very wide fluctuations of the angle of attack that go beyond the range available in the tables. Hence, I couldn't reliably compute the load fluctuations on the blade and the required spring parameters. Second, good practice requires to measure and calibrate each simulated sea state in the tank before testing the model, and waves take much longer to be calibrated. The simplest way to calibrate a steady current is to take a point measurement without the turbine in the tank. The procedure is quick and can be done sequentially for the different flow velocities that will be tested. Instead, waves, beside requiring the installation of wave gauges, need to be calibrated through several tests, since the current affects the wave

height. If the current is following the waves, the wave height is reduced and the wave length is increased [189]. The opposite phenomena occur when the current opposes the waves. As a consequence, the waves differ from the desired spectrum, and an iterative procedure is needed to analyse the measured spectrum to then modify the original spectrum to obtain the desired waves. This procedure has to be repeated for all the different current velocities that one wants to test, and then again for all different wave spectra, requiring a considerable amount of time. Due to the limited amount of testing time, I decided to minimise the time for sea state calibration and to maximise the turbine testing time.

For the passive-pitch blade to work, I expected two significant results: the mean torque value is the same as for the rigid blade; that the thrust and RBM fluctuations are reduced. I have shown in Chapter 3 that the load fluctuations can be reduced with different springs, though to a different extent. So for any chosen spring, I would expect to see some load mitigation. Instead, the mean torque and thrust values are determined by the preload, which is specific to a certain spring and flow condition. Once a spring is installed, an error in the preload will cause a shift in the mean loads values.

To circumvent this limitation, I planned the tests over a range of different current velocities and turbine rotational speeds. The idea is that if the low-order code prediction of the preload is inaccurate, small changes in the flow and turbine speeds would allow to investigate around the design conditions and find a match between the mean loads of the rigid and passive-pitch blade.

The design conditions are a nominal current speed $U_\infty = 0.8$ m s^{-1}, and the rotor operated in speed control mode with a constant speed of $\omega =$ 89 rpm (9.32 rad s^{-1}), to keep a constant tip speed ratio $\lambda = 7$. The tank parameters are Froude-scaled from a full-scale flow conditions with $U_\infty =$ 3 m s^{-1} and a 18 m diameter turbine rotating at 23 rpm (2.4 rad s^{-1}). I tested at nominal flow speeds $U_\infty = 0.9, 0.8, 0.7$ m s^{-1} and tip speed ratios $\lambda = 8, 7, 6, 5, 4.5$ (turbine speed range $\omega = 115 - 50$ rpm). Results for flow speeds $U_\infty = 0.9, 0.7$ m s^{-1} will not be displayed. These conditions were used for testing Reynolds independence, to make sure that the design

current speed did not present unusual flow phenomena, and to allow more flexibility to match the ideal spring preload which was designed on estimated loads. After testing the rigid blade configuration at different flow speed, no substantial difference in the flow behaviour was noticed. Due to some issue with the setup of the spring preload, I decided to concentrate the passive-pitch test at the design flow speed $U_\infty = 0.8$ m s^{-1}. A few passive-pitch tests were performed at $U_\infty = 0.9$ m s^{-1}, showing little visible differences compared to the design conditions, hence these partial, out-of-design results are here omitted. The estimated preload for $U_\infty = 0.8$ m s^{-1} and $\lambda = 7$ is $\theta_0 = 450$ deg. Due to a torsional spring slipping out of place, I realised that one blade had been tested with a lower preload angle of 275 deg. Moreover, after postprocessing of the data after the first testing day, I thought it would be better to use a higher preload of 550 deg to get a better results during the following tests. Eventually, I collected data for three different preload angles: $275, 450$ and 550 deg. The passive-pitch tests could be conducted with only one blade pitching passively and the remaining two being rigid because of the limitations of the turbine control system, which could not manage the speed swings of the turbine caused by three pitching blades.

6.7 Data analysis

Before the analysis of experimental data, the measured time series are processed. The turbine loads, including thrust, torque, and root bending moment, and the rotational speed from the generator encoder are filtered using a Hampel filter to remove outliers. The filter identifies as outlier any datapoint outside of 2.5 standard deviations from the median value of itself and three datapoints before and after, and it replaces it with the median value. Flow velocity measurements are filtered using an inbuilt Matlab function called "filloutliers" that identifies a datapoint as outlier if it lies more than three standards deviations from the signal average value. Outliers are replaced by linear interpolation of non-outlying datapoints.

The performance of the passive-pitch is assessed in two steps. First, I compute the load average values and standard deviations to assess the capability

of the preloaded spring to balance the average pitching moment and generate the same torque, thus the same average power as the rigid blade. Second, the load mitigation capabilities of the passive-pitch system are assessed from the percent reduction of the load fluctuations. Given the stochastic nature of experimental data, the load fluctuations are better represented by their standard deviations rather than the effective amplitude of the oscillations. Therefore, as opposed to the numerical part, the experimental results will be presented as the reduction of the loads standard deviation compared to the rigid case. Moreover, I will also analyse the power spectra of the loads and of the turbine rotational speed.

The power spectrum is obtained from the Fourier transform of the measured signal.

Similar to what I showed in Section 5.5, a time series $Q(t)$ can be described by its Fourier series as

$$Q(t) = Q_0 + \sum_{k=1}^{N_k} Q_k \exp(j2\pi f_k t + \chi_k), \tag{6.4}$$

where Q_0 is the average value, $Q_k = \Delta Q_k/2$ are the amplitudes of the N_k harmonic components describing the signal, f_k and χ_k are the frequency and phase values respectively. The period of the slowest component $\hat{T}_0$ corresponds to the length of the time series $\hat{T}_s$, and the frequency f_{N_k} of the fastest component is equal to the Nyquist frequency, or half the sampling frequency f_s. The length of the time series determines also the resolution of the Fourier series $\Delta f_k = 1/\hat{T}_s$ (i.e. the distance between two consecutive harmonic components). In this case, each test lasted 7.5 minutes, corresponding to a frequency resolution $\Delta f_k = 0.002$ Hz and the slowest harmonic $f_1 = 0.002$ Hz, and the sampling rate was $f_s = 256$ Hz, allowing to capture phenomena up to $f_{N_k} = 128$ Hz, for a total of $N_k = 5818$ Fourier components.

At each frequency f_k, the power spectrum is computed from the coefficients Q_k of the Fourier series as

$$S_Q(f_k) = \frac{Q_k^2}{2\Delta f_k}. \tag{6.5}$$

Since the energy of a signal by definition is

$$E_Q = \int_0^{\hat{T}_s} Q(t)^2 dt \simeq \sum_{k=1}^{N_k} {Q_k}^2, \tag{6.6}$$

it can be computed also from the power spectrum as

$$E_Q = \sum_{k=1}^{N_k} 2S_Q(f_k)\Delta f_k. \tag{6.7}$$

Therefore, the power spectrum S_Q represents the energy associated a certain frequency, and integration over the entire frequency range yields the energy of the signal. Moreover, the variance of the signal is related to the power spectrum as

$$\text{var} = \sum_{k=1}^{N_k} S_Q(f_k)\Delta f_k, \tag{6.8}$$

hence, integrating the power spectrum of a load signal between two frequency values provides the energy associated to that frequency interval, and it indicates also how much those frequencies contribute to the overall load fluctuation.

6.8 Uncertainty analysis

Experimental results are subject to error due to calibrations, environmental effects, equipment set-up and human factors. The results, however, are expected to remain within an interval around each measurement point. The uncertainty of an experiment is determined for a number of measurements and represents the possible value that the error might have, within a given confidence interval. The confidence interval is defined as the percentage chance that all of the values measured will lie within the specified range of the error. This value can be obtained statistically if the variable of interest has been measured directly, or via sensitivity analysis if the variable of interest is obtained as a function that relates different measured quantities.

In the results (Chapter 7), I will present the thrust and torque values measured directly from the load cell in the hub, and the root bending moment measured directly from the strain-gauged flexure at the blade root. Therefore, the uncertainty associated to the loads is the uncertainty associated to

their direct measurement. Both the loads cell and the the bending moment transducers had been calibrated by FloWave staff who found that the drift of calibration coefficients over time is negligible, hence the calibration coefficients were given. At the beginning of each day of testing, all loads were recorded with no flow and parked turbine to acquire the zero reference values.

Installing the blade with the correct geometric pitch is quite a challenge, and a misalignment as small as 1 mm, a that scale, can cause a change in the angle of attack of 1.5 deg which can cause a considerable load imbalance. Since the lift depends linearly with the angle of attack, near the blade tip, were the angle of attack is small, this uncertainty can cause considerable changes in the lift value. For instance, As shown in Chapter 5, the average angle of attack at $r/R = 0.75$ of the blade span is about 6 deg. The uncertainty associated to the blade installation angle translates to about 25% of the lift value. In the worst scenario, where a blade is installed at -1.5 deg from the nominal geometric pitch, and another blade is installed at 1.5 deg, the difference in the generated lift could be as high as 50%. I will show that this uncertainty caused a discrepancy between the measured root bending moments. Since the installation angle was not changed throughout all tests, the uncertainty does not affect a comparison between the rigid blade and the passively-pitching blade as long as it's the same blade. However, the installation angle determines the average loads on the blade, including the pitching moment and, hence, the spring preload that balances it. Hence, I'm expecting different average loads on the pitching blade compared to the rigid one, even at the design conditions (i.e. $\lambda = 7$, $U_\infty = 0.8$ m s^{-1}, preload 450 deg). This issue will be partially mitigated by testing different preloads, which will allow to tune the average spring moment.

The torsional spring properties were verified through bench tests. I devised a small test rig where the blade was attached to a fixed beam and it was turned by certain angles to load the spring. A smaller beam was connected to the blade flange perpendicular to the blade axis, and was allowed to hit a scale to measure the force exerted by the loaded spring. The force was thus converted into the spring reaction moment by multiplying the force

by the distance between the blade pitch axis and the impact point on the beam. Figure 6.10 shows the spring moment computed for each spring at different preload values, and the theoretical moment according to the nominal spring stiffness provided by the manufacturer. All the springs behave linearly across the entire range considered, with slope similar to the nominal value, but the reaction moments are different from the theoretical one. These differences will affect the capability of the preloaded springs to balance the average fluid moment. However, since the the difference generated by adopting different preloads is greater than the difference between the measured springs moments to the theoretical value, testing the springs with different preloads will provide some insight on the effect of the preload.

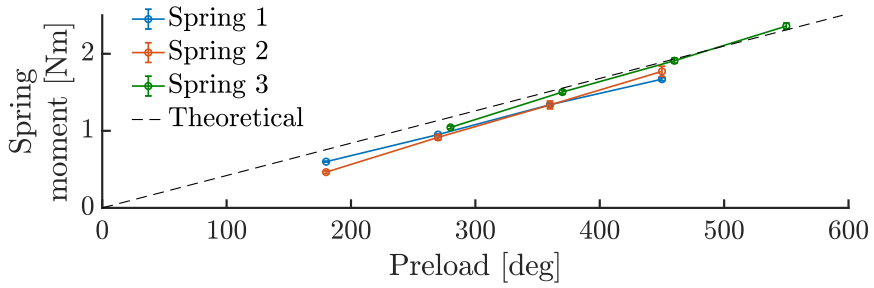

Figure 6.10: Measured spring moments. Each curve represents a different spring and each measurement point feature a one-standard deviation errorbar.

The spring is preloaded in two ways, as mentioned in Section 6.3.4. The series of holes on the top of the casing and in the carbon fibre cone allow to adjust the preload with an accuracy of 5 deg. This represents also the maximum uncertainty associated to the preload. For the tested preload values of 275 deg, 450 deg, and 550 deg, the uncertainty associated to the preload translate to an uncertainty associated to the spring moment which is less than 2% in all cases.

7

Experimental results

In this chapter, I present the results from the experimental campaign conducted at FloWave Ocean Energy Research Facility on 16th-23rd November.

I will assess the effectiveness of the passive-pitch system with respects to two aspects: the load mitigation performance, and the average load generated. The former will prove the effectiveness of the passive-pitch system and it will also indicate the goodness of the spring stiffness value estimated by the low-order code. The latter will show if the spring preload was correctly estimated to balance the hydrodynamic loads.

7.1 Benchmark case: the rigid blade

Figure 7.1 shows the rotor torque Q and thrust T, and the rigid blade bending moment RBM for all the tested tip speed ratios λ at the nominal flow speed $U_\infty = 0.8$ m s^{-1}. The graphs show the average values and the errorbars represent one standard deviation of the load fluctuations. The RBM is shown only for two blades because the third blade had a faulty transducer which broke during the installation of the turbine on the tank floor. The thrust and RBM show a similar trend, with the average values increasing at higher λ due to higher dynamic pressure. The RBM of blade no. 2 are shifted to higher values compared to blade no. 1, due to inaccurate mounting of the blades which caused higher geometric pitch, as discussed in Section 6.8. The average torque generated increases as λ decreases from 8 to 4.5, which is the optimal tip speed ratio for the TGL blade design. The amplitude of

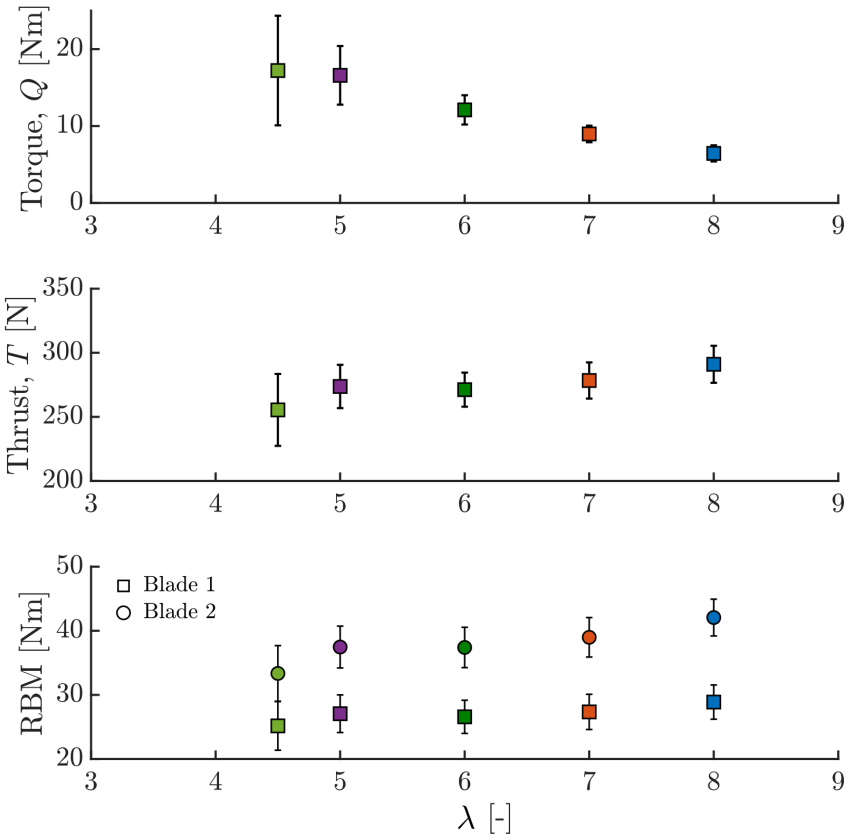

Figure 7.1: Average values of rotor torque Q, thrust T and rigid blade root bending moment RBM at flow speed $U_\infty = 0.8$ m s^{-1}. The load fluctuations are represented by one standard deviation errorbars.

the torque fluctuations also increases significantly at low λ. I will show that these fluctuations are mostly due to the turbine instability at low speeds.

Figure 7.2 shows the torque power spectra, with the frequency values on the horizontal axis normalised by the average rotor speed. Vertical, dashed lines indicate the main load components. For $\lambda = 4.5$, 5 and 6, there is a dominant periodic load at 3P (i.e. three times the rotor period) due to each blade rotating in the shear flow, from high-speed regions (top position) to low-speed regions (bottom position), and the presence of the tower 486 mm downstream of the rotor, which deviates the upstream flow. The area under the spectrum represents the energy content of the fluctuations and the variance of the

signal, and it indicates that the 3P broad peak strongly contributes to the torque fluctuations. The 3P peaks are not visible at $\lambda = 7$ and $\lambda = 8$. Sharp peaks are present in all cases at 6, 12 and 24 times the rotor frequency. The 12P and 24P peaks have been previously identified as motor cogging effects introduced by the 12-pole motor used in the turbine [20]. Since the amplitude of the peaks decreases at the higher frequencies, it suggests that the 6P is the base frequency and the 12P and 24P are its second and third harmonic. By inspecting the spectra close to the y-axis, let's note that at $\lambda = 4.5$ the torque has a low-frequency contribution which is one order of magnitude higher than at $\lambda = 8$. The signal intensity decreases with increasing λ, indicating that at low tip speed ratio the torque experiences wide fluctuations at a frequency lower than 1P, and that the amplitude of these fluctuations decreases at higher tip speed ratios. It is not known what is the source of this low frequency fluctuation. The red circle in Fig. 7.2, highlights a very strong and narrow peak which appears only at $\lambda = 4.5$ and $\lambda = 5$. Moreover, such peak does not scale with the rotational regime of the turbine. The significance of this phenomenon will be discussed later.

Similar considerations are drawn for the thrust power spectra shown in Fig. 7.3. In this case the 3P peak is visible for all tip speed ratios, and the higher harmonics at 6P and 9P are also visible despite the lower intensity. The motor cogging effects do not affect the thrust as much as the torque, in fact, the 12P and 24P peaks are not visible. The flat peak at 1P is most likely due to drive-train misalignment and to load imbalance between the blades, as explained in Section 6.8. A secondary peak at 2P is also noticed. Also in this case, the red circles indicate sharp peaks at low tip speed ratios that don't scale with the turbine frequency.

Figure 7.4 shows the RBM power spectra. The broadest peak happens at 1P, which is consistent with the 3P loads in the thrust and torque spectra. Higher harmonics can be seen at 2P and 3P, and at high λ also at 4P and 5P. These harmonics are not clearly identifiable at low tip speed ratios since the signal is dominated by the sharp peaks indicated by the red circles. Only

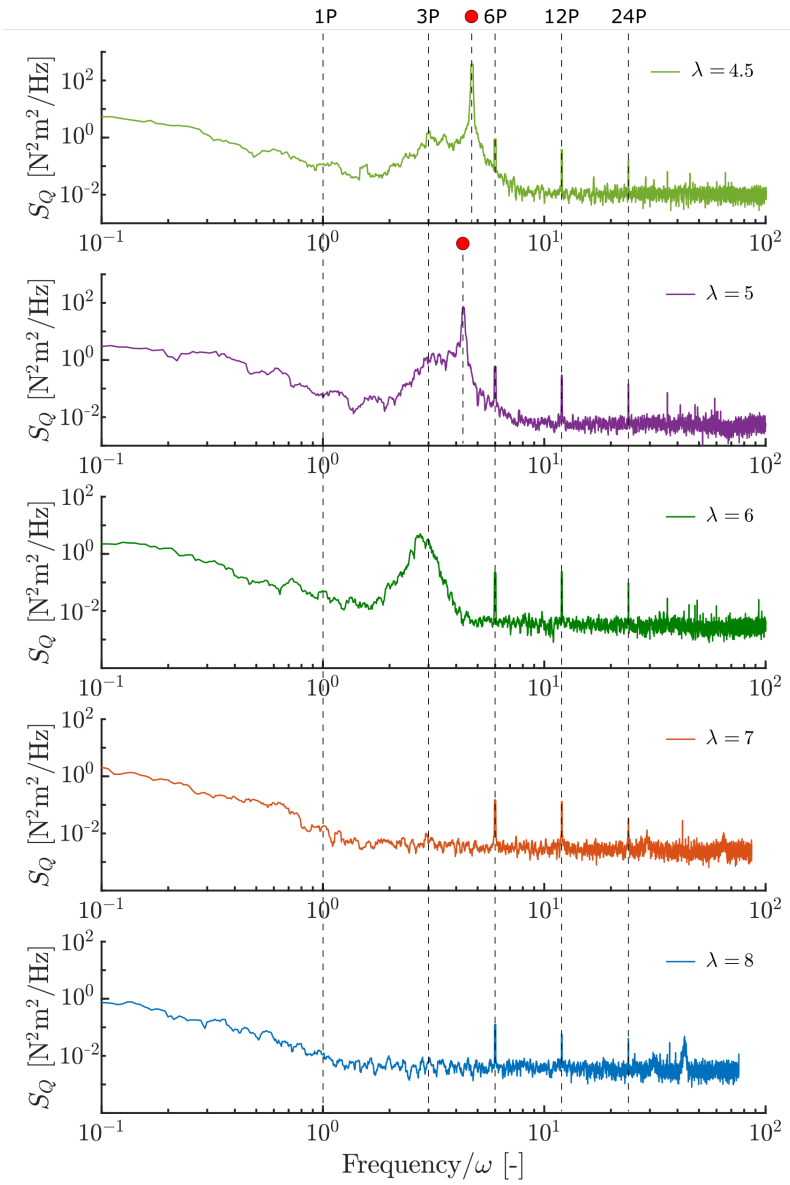

Figure 7.2: Torque power spectra at different tip speed ratios λ, $U_\infty = 0.8$ m s^{-1}. The dashed, vertical lines identify the frequency of relevant load harmonics.

minor differences are noted between the two blades.

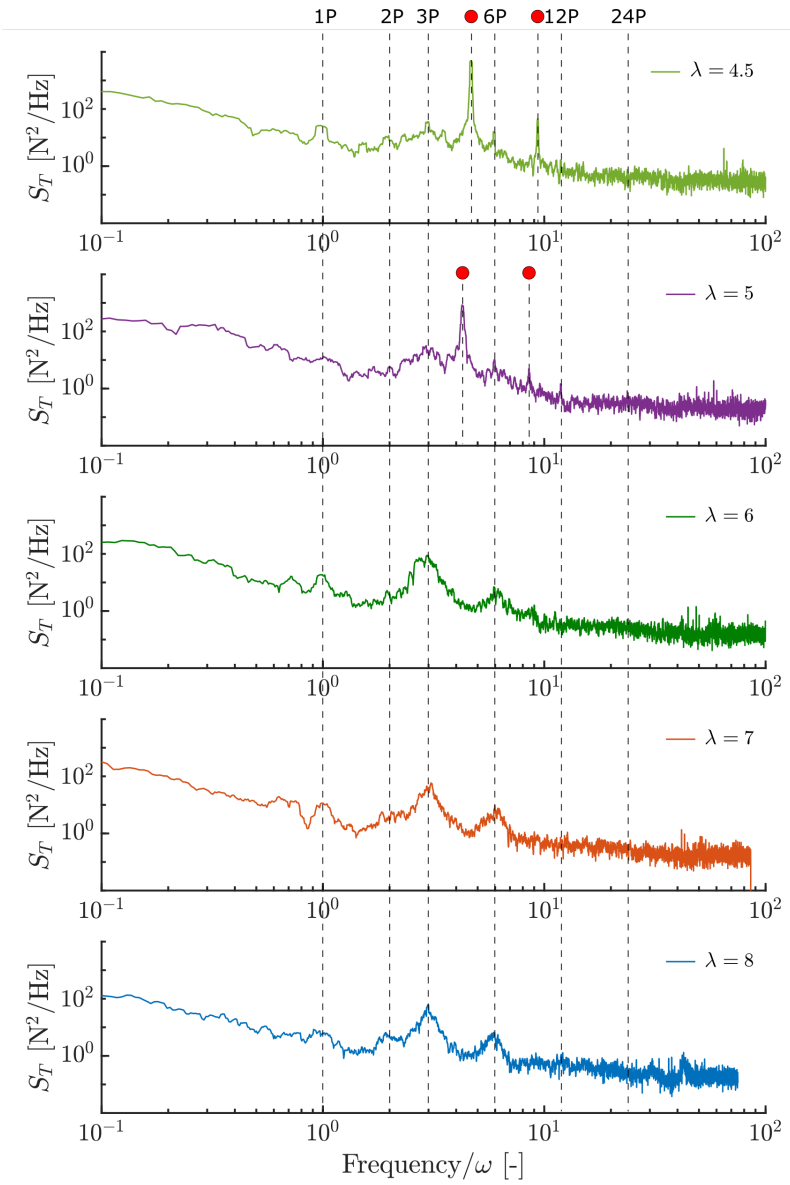

Figure 7.3: Thrust power spectra at different tip speed ratios λ, $U_\infty = 0.8$ m s^{-1}. The dashed, vertical lines identify the frequency of relevant load harmonics.The red circles identify a periodic load that happens at a fixed frequency and does not depend on the rotational speed of the turbine.

7.1.1 Turbine instability

The peaks identified by red circles in Figs. 7.2, 7.3 7.4 can be better understood by plotting the spectra over the dimensional frequency values as shown

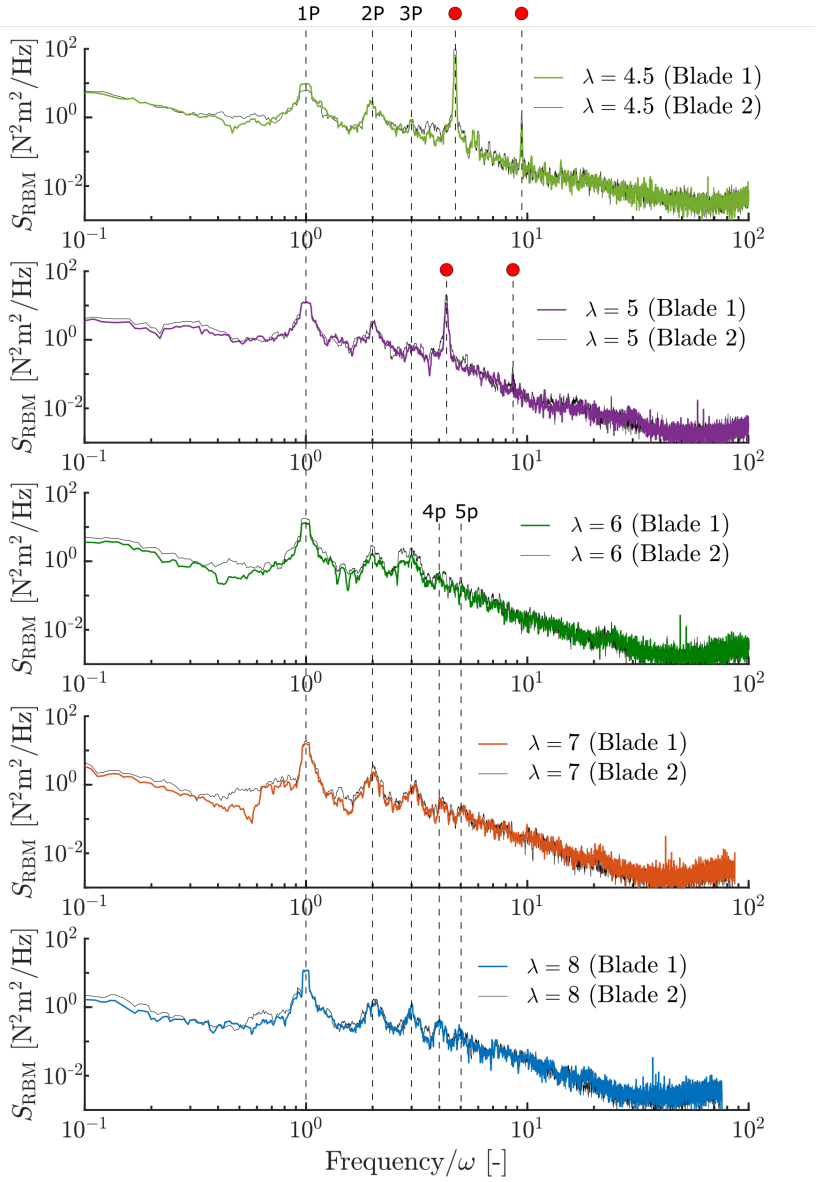

Figure 7.4: RBM power spectra at different tip speed ratios λ, at $U_\infty = 0.8$ m s^{-1}. The dashed, vertical lines identify the frequency of relevant load harmonics. The red circles identify a periodic load that happens at a fixed frequency and does not depend on the rotational speed of the turbine.

in Fig. 7.5. The vertical, dashed lines indicate the frequencies of such peaks. The highest peak happens at a frequency of about 4.5 Hz, with a secondary peak shown at twice that frequency, at 9 Hz. Both peaks are clearly visible

in the thrust spectra S_T and the spectra of the turbine rotational speed S_ω, whereas the torque spectra S_Q shows only the first peak, and the flow velocity spectra S_{Ux} show none. The peaks frequencies coincide at $\lambda = 4.5$ and $\lambda = 5$, confirming that the phenomenon does not depend on the speed of the turbine. The peaks are about two orders of magnitude more intense than the underlying signal at 4.5 Hz. The peaks are apparent also at $\lambda = 7$, however, 4.5 Hz and 9 Hz correspond to the 3P and 6P frequencies respectively, and the peaks are thus expected. The fixed-frequency phenomenon is not due to flow speed fluctuations since there is no relevant flow phenomenon at 4.5 Hz in the flow speed spectra S_{Ux}. Instead, it's a phenomenon due to the turbine, and it is manifested only at low tip speed ratios as shown by the spectra S_ω. Since the peaks are not visible when the turbine rotates in the absence of current (see S_ω - no flow, Fig. 7.5), the phenomena is likely an instability in the turbine rotational speed that happens for specific combinations of flow and rotational speeds, as first noted by Payne et al. [187].

7.2 Passive-pitch system effectiveness

Tests with the passive-pitch system were conducted with one blade passively pitching at a time, to overcome the limitations of the turbine speed control system. I tested three different setups for the passive-pitch system. In the first two, blade no. 1 was allowed to pitch and it had preload angles of 275 deg and 450 deg, respectively. In the third setup, blade no. 2 had a preload angle of 550 deg.

7.2.1 Effect of preload angle

The passively pitching blades were not capable of generating the same average loads as the rigid blades. Figure 7.6 compares torque Q, thrust T and root bending moment RBM of the rigid blade with the respective quantities measured with a passively-pitching blade. Since the RBM values for the rigid blade showed different mean values between blade no. 1 and blade no. 2, the comparison with the passive-pitch blade is shown separately.

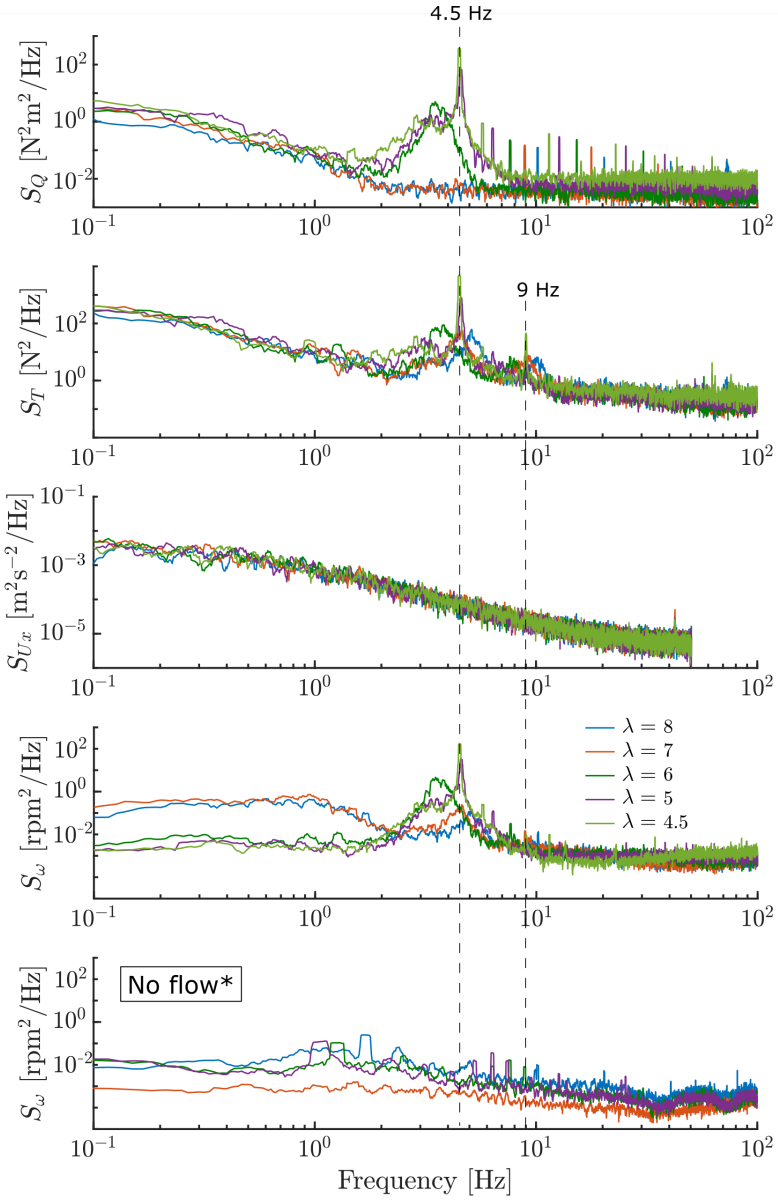

Figure 7.5: Spectra at different tip speed ratios λ, at $U_\infty = 0.8$ m s^{-1}. Starting from the top, the graphs show the torque spectra, thrust spectra, the spectra of the point-measured flow velocities, and the spectra of the rotational speed of the turbine at $U_\infty = 0.8$ m s^{-1} and in the absence of flow. (*λ for the "no flow" condition represent the turbine rotational speed and are computed using a flow speed of 0.8 m s^{-1})

Let's note that, compared to the rigid case, the average torque of the pas-

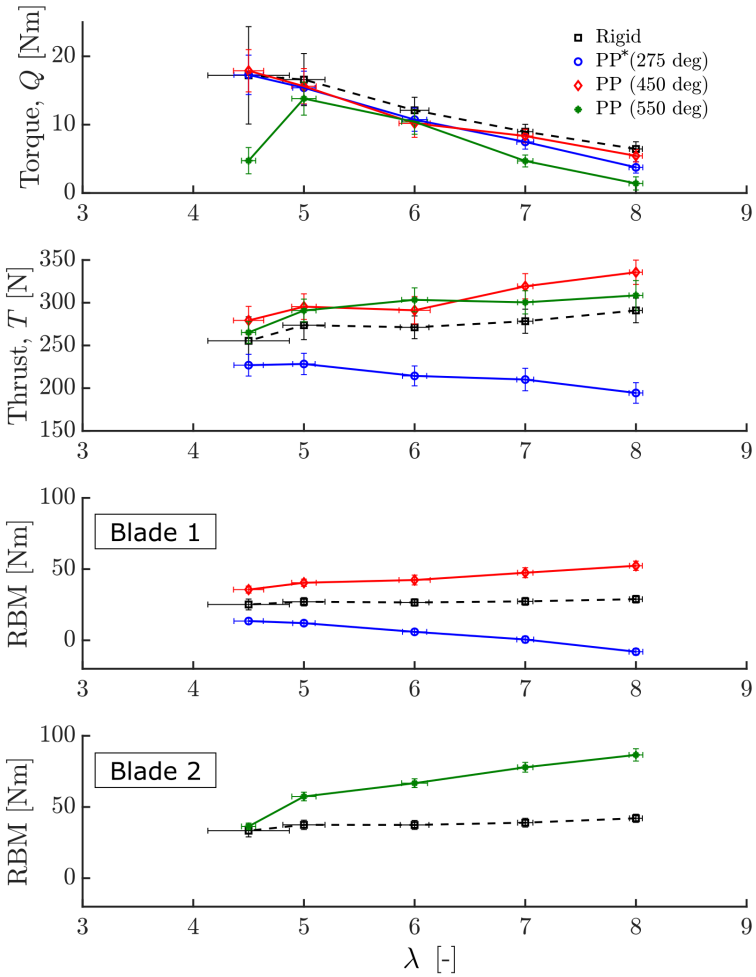

Figure 7.6: Average values of rotor torque Q, thrust T and root bending moment RBM for the rotor with one passively pitching blade, at flow speed $U_\infty = 0.8$ m s^{-1}. The fluctuations of loads and λ are represented by vertical and horizontal one standard deviation errorbars respectively. The rigid blade loads are shown as dashed black lines. (*Passive Pitch, preload angle is indicated in parenthesis)

sive pitch system is lower at all tip speed ratios and for all preloads. Instead, the average thrust and bending moments are lower for preload 275 deg but higher for preloads 450 deg and 550 deg. This behaviour is readily explained. A preload of 275 deg is too low to generate a spring moment that balances the average fluid pitching moment at the design incidence, the blade pitches nose-down and the incidence is reduced to a value where the spring preload can balance the fluid moment. In this condition, the blade generates less lift,

and it experiences lower torque, thrust, and bending moment. In particular, at $\lambda = 8$, the high rotational speed reduces the inflow angle such that the blade experiences negative angles of attack and the lift acts in the opposite direction (i.e. it points upstream and backwards instead of downstream and in the direction of the blade motion). In fact, the bending moment becomes negative, whereas thrust and torque remain positive since they consider also the contributions of the other two blades[1].

Conversely, for preloads 450 deg and 550 deg, the pitching blade operates at higher incidence, generating greater lift but also greater drag, resulting in lower torque, higher thrust, and higher bending moment. This effect is amplified at incidences close to the static stall angle, where increasing the angle of attack generates a small lift increase and a substantial drag increase. In extreme cases, at low tip speed ratios, the angle of attack might become so high that separation occurs. The fluid loading would thus be determined mainly by drag, due to the loss of lift, and the blade would generate a net negative torque contribution, whilst the thrust and bending moment would be lower but still positive. I believe separation occurred for $\lambda = 4.5$ and preload 550 deg. In fact, the rotor torque in Fig. 7.6 shows a substantial decrease, whereas thrust and bending moment are less affected.

From the results shown in Fig. 7.6, it is evident that a preload of 275 deg is too low, that 450 deg and 550 deg are too high, and that the right preload (i.e. the preload that allows the same average loads as for the rigid blade) lies in between, at all tip speed ratios.

To further interpret these results, let's consider that the design preload angle was 450 deg, and it was computed for $U_\infty = 0.8$ m s^{-1} and $\lambda = 7$. Experiments showed that preloads 450 deg and 550 deg are too high, and 275 deg is too low. For higher preloads, the blade experiences higher angles

[1]The negative RBM is caused by the sections near the blade tip, which experience negative incidence and generate higher loads than the root sections. Instead, the pitching moment is determined mainly by the sections near the root due to the greater moment arm. Since the root sections have a higher geometric twist their incidence remains positive, they balance the spring moment, and they keep the blade stable whilst generating a negative RBM.

of attack along its entire span compared to design conditions, whereas for the lower preload, the incidence is lower. When operating at higher tip speed ratio, the RBM changes according to two competing effects, namely dynamic pressure increase and reduction of the angle of attack. The former intensifies the average RBM, the latter reduces it. Both the dynamic pressure and the incidence change equally on each blade, regardless of the spring preload, however, the effect on the RBM is different. Let's consider the lift in Eq. 3.6 for a blade section, where the lift coefficient is approximated as $2\pi\alpha$. The lift is

$$L = \frac{1}{2}\rho_w c U_7^2 2\pi\alpha_7, \tag{7.1}$$

where the pedix "7" indicates the conditions at $\lambda = 7$. At $\lambda = 8$, the inflow speed increases by ΔU and the incidence decreases by $\Delta\alpha$, which are independent of the preload and hence equal for each blade. In first approximation, the change in the lift can be described as

$$\Delta L = \left(\frac{\partial L}{\partial U}\right)_7 |\Delta U| - \left(\frac{\partial L}{\partial \alpha}\right)_7 |\Delta\alpha|, \tag{7.2}$$

where

$$\begin{aligned} \left(\frac{\partial L}{\partial U}\right)_7 &= \rho_w c 2\pi U_7 \alpha_7, \\ \left(\frac{\partial L}{\partial \alpha}\right)_7 &= \frac{1}{2}\rho_w c 2\pi U_7^2. \end{aligned} \tag{7.3}$$

For any preload, the change of the angle of attack causes the same reduction in the lift. Instead, the increase of dynamic pressure causes a greater lift if the incidence was higher to begin with. I believe that for preloads 450 deg and 550 deg, since the blade operated at a higher incidence, the increase in the dynamic pressure had a greater effect on the loads than the reduction of the angle of attack. Hence, the RBM increases together with the tip speed ratio. Conversely, at preload 275 deg, the angle of attack is lower, and its

reduction dominates over the dynamic pressure increase. Hence, the RBM decreases as the tip speed ratio increases. In fact, Fig. 7.6 shows that the blade with spring preload 275 deg experiences lower RBM as the tip speed ratio increases, whereas blades with preload 450 deg and 550 deg show and increasing RBM.

7.2.2 Effect of friction on the system performance

The capabilities of the passive-pitch system to mitigate the load fluctuations will be presented only for the blade with preload 275 deg, since in the other two cases friction prevented the system from working correctly. Although the spring can generate enough torque to balance the average loads (about 2 Nm for preload 450 deg), the system mitigates load fluctuations which are one order of magnitude smaller than the average loads, hence, as much as 0.1 Nm friction torque can deteriorate the system performance considerably. The two sources of friction are the bearings and the contact between the shaft and the spring wound around it.

Bearings friction

The bearings friction was not not specified by the manufacturer and it is difficult to measure due to the small scale of the loads and the complexity of the measurement [190]. However, it's possible to estimate the impact of the bearing friction on the effectiveness of the passive-pitch system. Bearings friction are typically estimated with empirical formulas. Ball bearings present four sources of friction: rolling motion, sliding motion, the presence of seals, and the drag from churning and splashing of the lubricant within the bearings [191]. The rolling, sliding, and drag friction depend on the rotational speed and they are not relevant in this case because the pitch motion of the blade is intermittent and limited to a few degrees about the average angular position. Moreover, frictional losses from the seals may exceed the other losses in the bearings, making them the main contributor to friction. The frictional moment from the seals M_{seal} can be estimated in Nmm as

$$M_{\text{seal}} = K_{\text{S1}} d_{SS}^{\beta} + K_{\text{S2}}, \tag{7.4}$$

where d_S is the seal counterface diameter, which is 30 mm, whereas K_{S1}, K_{S2}, and β_S are empirical constants. For angular contact ball bearings, like those that I used, the empirical constants indicated by bearing manufacturer SKF are $K_{\text{S1}} = 0.014$, $K_{\text{S2}} = 10$ and $\beta_S = 2$ [191]. The estimated frictional moment of the seals is 0.023 Nm, which is about 1% of the average pitching moment or 10% of the amplitude of the moment oscillations. Although the friction caused by the bearings does not stop the passive-pitch system, it reduces in part its effectiveness.

Contact friction between spring and shaft

The friction due to contact between the spring and the shaft is more difficult to estimate due to the unique and uneven contact pattern between the parts. As the spring is preloaded, it tightens around the shaft reducing the clearance and increasing the chance of contact. As shown in Fig. 7.7, the spring has a nominal inner diameter[2] $d_{in} = 22.65$ mm, $N_c = 16$ coil turns at rest, the wire is $t_w = 2.34$ mm thick, and the length of the wire $L_w = N_c \pi (d_{in} + t_w/2)$ is thus known and equal to 1256.10 mm. Table 7.1 summarises the changes of the spring inner diameter d_{in}, the clearance c_w from the shaft which has 20 mm nominal diameter, and the number of coils N_c when applying different preloads.

The spring with preload 275 deg has a clearance from the shaft which is 1.8 times bigger than the spring with preload 450 deg, and 3.3 times bigger than the spring with preload 550 deg. Moreover, I estimated that the spring would lock on the shaft when it reaches an angle of 683 deg due to excessive tightening of the coils. Bench tests showed that the spring locks onto the shaft after almost two full turns, confirming the estimate accuracy. Since the springs with preloads 450 deg and 550 deg exhibited

[2]The nominal dimensions of the springs are provided by the supplier and they were confirmed by measurements.

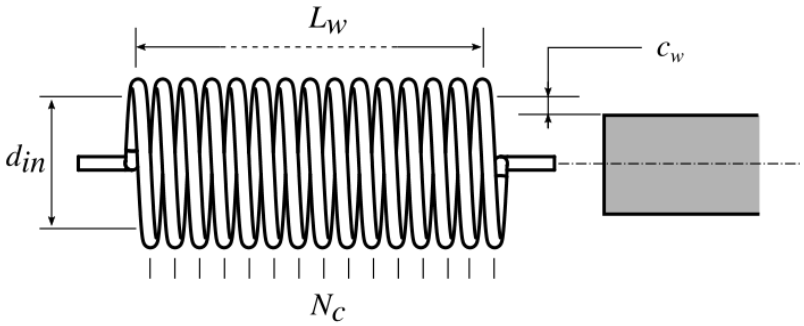

Figure 7.7: Spring dimension and clearance from shaft.

Preload [deg]	No. coils N_c [-]	Spring diameter d_{in} [mm]	Clearance c_w [mm]
0 (rest)	16	22.65	1.32
275	16.76	21.52	0.76
450	17.25	20.83	0.41
550	17.53	20.46	0.23

Table 7.1: Change in spring dimension and clearance from shaft due to preloading.

a slight bend along their axis, I believe that these springs generated more friction compared to the spring with preload 275 deg, and that the load mitigating capability was compromised. Hence, in the next section, I will assess the load mitigating capabilities only for the tests performed using the spring preloaded at 275 deg.

7.2.3 Load mitigation

The passive-pitch system was capable of mitigating the load fluctuations at all tip speed ratios, as shown in Fig. 7.8. Starting from the top, the graphs show the change in the fluctuations amplitude of torque, thrust, RBM, and rotational speed. The fluctuations amplitude is represented by the standard deviation, and amplitude change is shown in percentage with respect to the rigid rotor case. Results are shown for the passively pitching blade installed with preload angle 275 deg and they are in green when the fluctuations

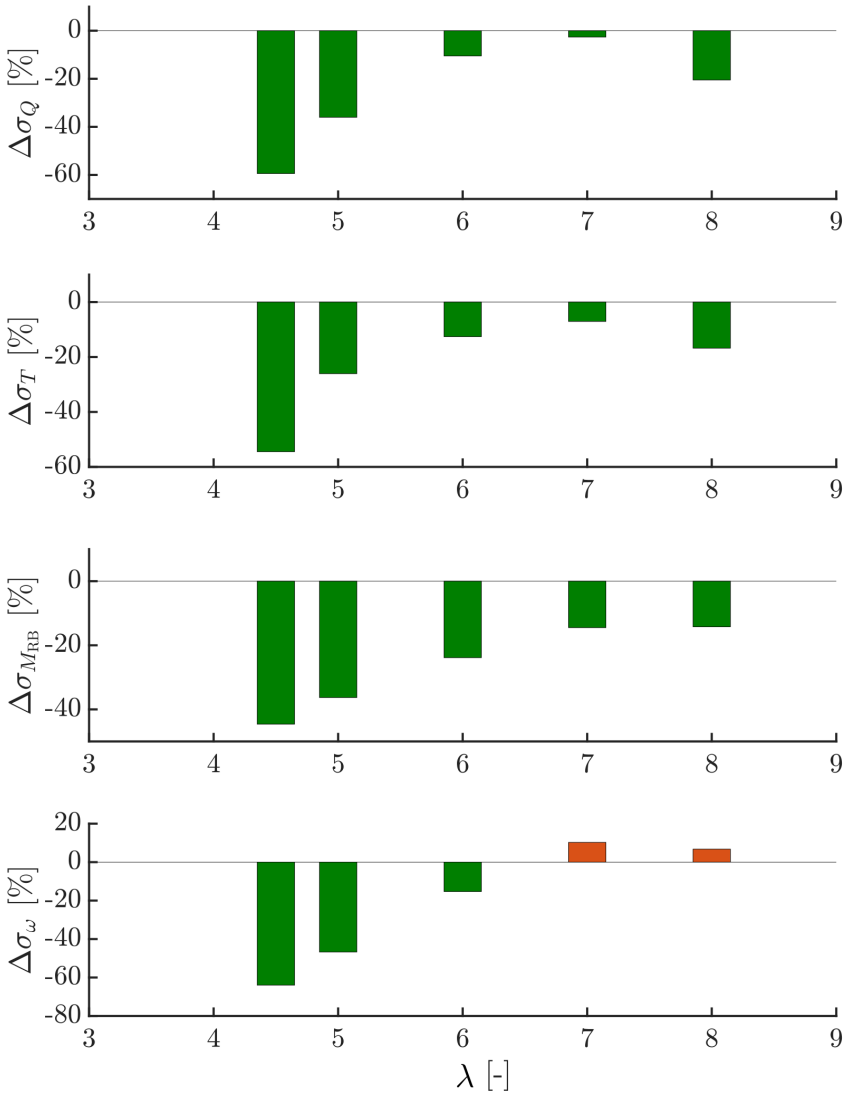

Figure 7.8: Mitigation of the amplitude of torque Q, thrust T, root bending moment M_{RB}, and rotational speed ω fluctuations with respect to the fully-rigid rotor. The amplitudes are represented by the respective standard deviations. Green bars indicate a reduction of the amplitude, red bars indicate an increase.

amplitude decreases, and in red when the fluctuations amplitude increases.

In all cases considered, all the loads have consistently been reduced. Peak performance can be observed at $\lambda = 4.5$, where fluctuations of thrust are mitigated by 55%, RBM fluctuations by 45%, and torque fluctuations by

60%. The poorest performance is observed at $\lambda = 7$, where fluctuations of thrust, RBM, and torque are reduced by 7%, 14%, and 2% respectively.

Let's note that the passive pitch performance is consistent with the changes of the turbine speed fluctuations shown in Fig. 7.8, as load fluctuations are due to oscillations of the blade incidence but also to fluctuations of the dynamic pressure which is determined mainly by the turbine speed. In particular, at low tip speed ratio ($\lambda = 4.5,\ 5,\ 6$) the oscillations of the loads and of the turbine speed are both alleviated. Since the passive-pitch system mitigates the loads by changing the blade pitch angle, it affects directly the blade incidence but not the turbine speed, which instead is determined by a more complex interaction between the rotor, the drivetrain, and the control system. It is thus not possible to establish if the load mitigation was due to the change of the turbine speed or to the passive-pitch system. Conversely, at high tip speed ratio ($\lambda = 7,\ 8$), the loads are alleviated despite the increase in amplitude of the turbine speed fluctuations, proving that the system worked as intended.

In the following sections, I will show that the passive-pitch system worked in all cases. In particular, at low tip speed ratio, I will prove that the load alleviation was due to the combination of the passive-pitch system effectiveness and the reduction of the turbine speed fluctuations. Instead, at high tip speed ratio, the load mitigation was due only to the passive-pitch system, further confirming the system effectiveness.

Mitigation of load fluctuations at low tip speed ratio

Let's consider the power spectra in Fig. 7.9. The graphs compare the frequency content of the loads at $\lambda = 4.5$ for the rigid and the passively-pitching systems. The amplitude of the fluctuations is determined by the height and the width of the peak at a given frequency (see Section 6.7), and a lower or narrower peak corresponds to reduced fluctuations amplitude.

The intensity of the highest peak at 4.5 Hz (i.e. due to turbine instability - Section 7.1) is reduced by at least one order of magnitude for all loads.

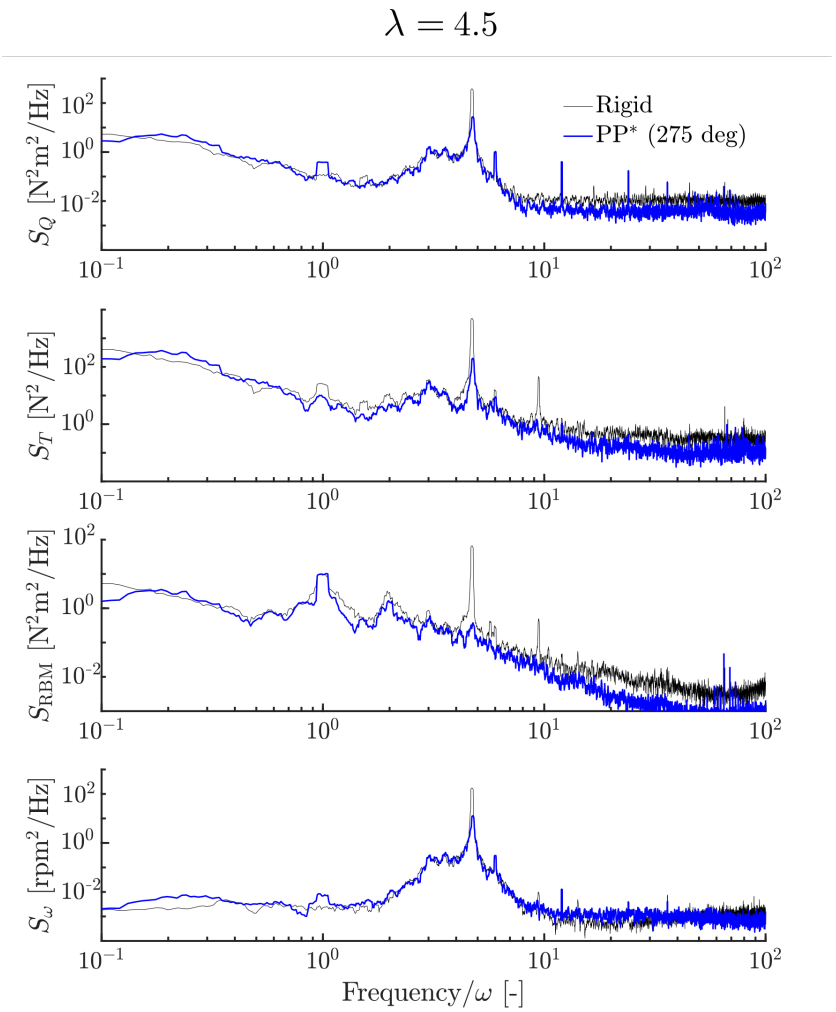

Figure 7.9: Power spectra of torque Q, thrust T, root bending moment M_{RB} and rotor speed ω at $\lambda = 4.5$. Each graph compares the spectra of the rigid and the passive pitch systems. (*Passive Pitch, preload angle is indicated in parenthesis)

In the case of the RBM, the peak is reduced by two orders of magnitude, it nearly disappears, and the second load harmonic at 9 Hz also disappears. However, the spectrum of the turbine speed shows a comparable mitigation of the same peak, suggesting that the load alleviation is due to a more stable speed rather than the passive-pitch system. The turbine speed presents also a higher peak at 1P, which can be noted also in the torque spectrum, caused by the rotor imbalance due to the passively pitching blade that experiences different loads compared to the other two blades. Similar considerations

apply also to the spectra at $\lambda = 5$ and $\lambda = 6$, shown in Fig. 7.10. Beside the above observations, the differences between the spectra of the passive-pitch case and those of the rigid case are quite small, which makes it difficult to judge the effectiveness of the passive-pitch system across the entire spectrum.

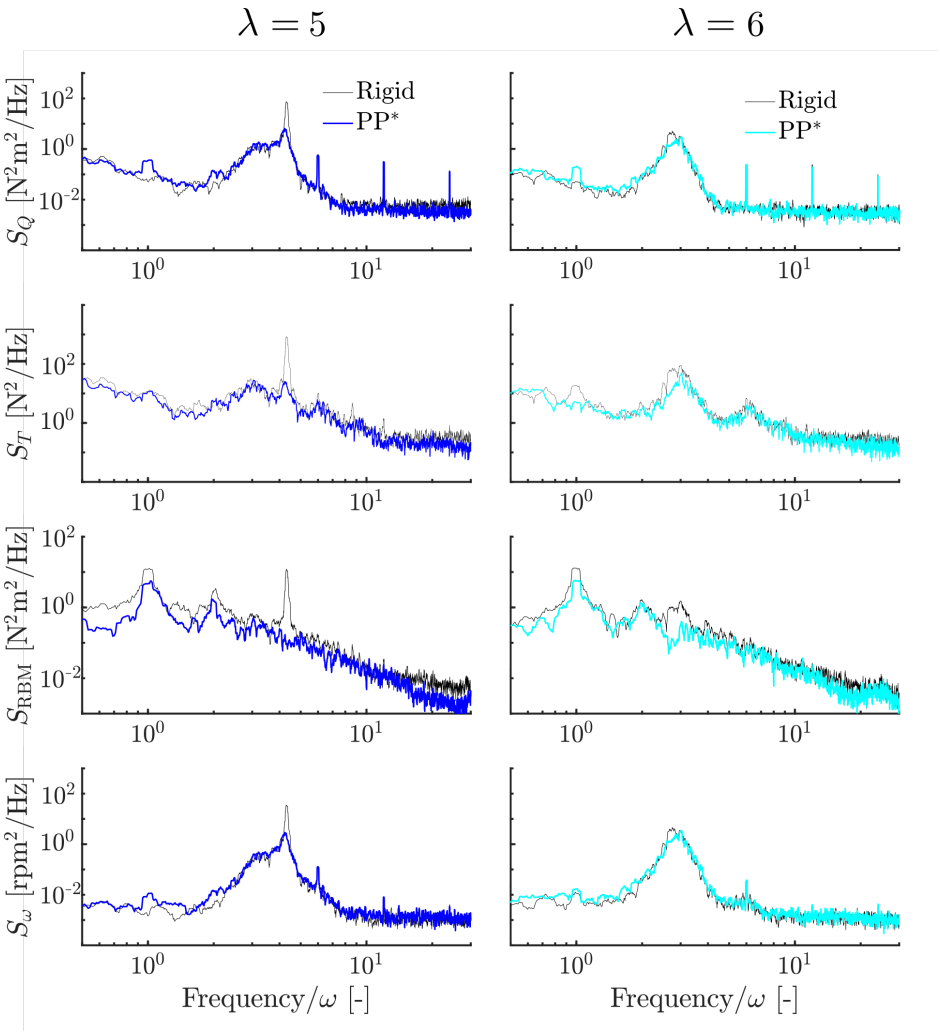

Figure 7.10: Power spectra of torque Q, thrust T, root bending moment M_{RB} and rotor speed ω at $\lambda = 5$ (left) and $\lambda = 6$ (right). Each graph compares the spectra of the rigid (black) and the passive pitch systems (blue and cyan). (*Passive Pitch)

Tables 7.2, 7.3 show the ratio of the variance associated to a certain frequency range between the passive-pitch case and the rigid case. This analysis allows to identify all the frequencies affected by the passive-pitch system, and

to better quantify its effectiveness. If a number is smaller than one, the fluctuations associated to a certain frequency band are mitigated, if greater than one, they are amplified.

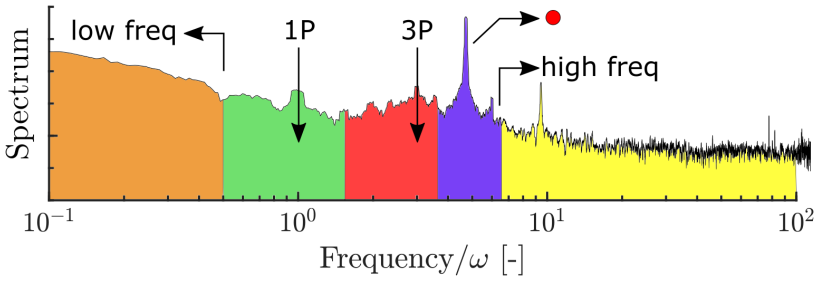

	frequency	low	1P	3P	●	high
var ratio torque [-]	$\lambda = 4.5$	0.95	1.20	0.99	0.12	0.48
	$\lambda = 5$	1.27	1.26	1.15	0.25	0.67
	$\lambda = 6$	1.07	1.59	0.66		0.95*
var ratio thrust [-]	$\lambda = 4.5$	0.86	0.73	0.82	0.07	0.37
	$\lambda = 5$	1.05	0.72	0.88	0.13	0.57
	$\lambda = 6$	0.92	0.76	0.44		0.78*
var ratio speed [-]	$\lambda = 4.5$	1.67	1.52	1.07	0.12	0.80
	$\lambda = 5$	1.26	1.77	1.20	0.23	0.84
	$\lambda = 6$	1.35	1.58	0.69		1.12*

Table 7.2: Mitigation of loads variance across different frequency components and tip speed ratio. The values represent the variance of the passively pitching blade loads as a fraction of the variance of the rigid blade loads. Values smaller than one indicate a reduction of the variance associated to that frequency component. (* For $\lambda = 6$, only one frequency band is considered above the 3P band, since there is no load peak at 4.5 Hz)

The turbine speed fluctuations are mitigated at high frequencies, but amplified at low frequencies, as shown in Table 7.2. In particular, for $\lambda = 4.5$ and $\lambda = 5$, the mitigation of the peak at 4.5 Hz is so great that the turbine speed fluctuations are overall reduced. For $\lambda = 6$, there is not distinct peak at 4.5 Hz, but the turbine experiences intense speed fluctuations close to the 3P frequency, which are reduced in the passive-pitch case. The torque spectra

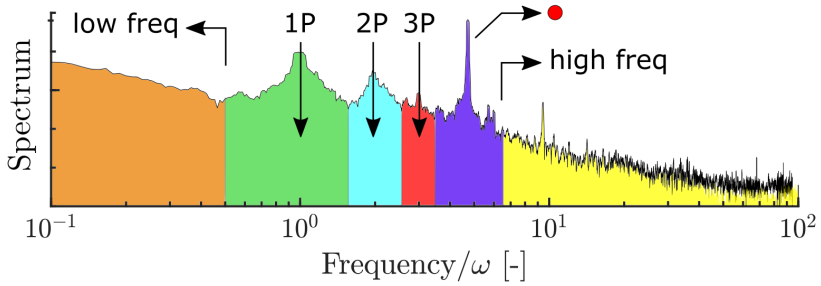

	frequency	low	1P	2P	3P	●	high
var ratio RBM [-]	$\lambda = 4.5$	0.77	0.83	0.63	0.69	0.04	0.30
	$\lambda = 5$	0.54	0.46	0.48	0.60	0.14	0.55
	$\lambda = 6$	0.72	0.51	0.84	0.23	0.69*	

Table 7.3: Mitigation of RBM variance across different frequency components and tip speed ratios. The values represent the variance of the passively pitching blade loads as a fraction of the variance of the rigid blade loads. Values smaller than one indicate a reduction of the variance associated to that frequency component. (* For $\lambda = 6$, only one frequency band is considered above the 3P band, since there is no load peak at 4.5 Hz)

are consistent with the speed spectra, with greater mitigation experienced around the peak at 4.5 Hz, but more intense fluctuations at lower frequencies, particularly around 1P peak. Instead, the thrust and the RBM are mitigated consistently across the entire spectrum, including 1P, 2P, and 3P frequencies, despite more intense speed fluctuations. The effects are larger for the RBM, since it considers only the passively-pitching blade and is therefore more representative of the effectiveness of the passive-pitch system.

The mitigation of the load fluctuations is thus due in part to the reduction of the turbine speed fluctuations, and in part to the passive-pitch system. Most importantly, I showed that the RBM fluctuations at 1P, 2P, and 3P frequencies is mitigated by the passive-pitch system, despite greater speed oscillations. Since the system was designed to alleviate load fluctuations at those frequencies (i.e. oscillations due to shear flow), these results confirm the load-mitigating capabilities of the passive-pitch system.

Mitigation of load fluctuations at high tip speed ratio

Figures 7.11, 7.12 show the loads and turbine speed spectra for a turbine operating with one passively-pitching blade, at $\lambda = 7$ and $\lambda = 8$ respectively. Similar to the rigid case, there is no distinct peak caused by the turbine instability, as shown by the smooth torque spectra. As opposed to lower tip speed ratios, there is no obvious peak reduction, and the turbine speed is dominated by low frequency fluctuations. In particular, the turbine speed spectra shows a more intense 1P peak due to blade imbalance. Overall, the differences between the spectra for the passive-pitch case and those for the rigid case are small.

Tables 7.5, 7.4 compare the variance associated to different frequency bands between the passive-pitch case and the rigid case. A variance ratio smaller than one indicates mitigation of the fluctuations, if the number is greater than one the fluctuations are amplified. As for lower tip speed ratios, the turbine speed fluctuations are mitigated at high frequencies (i.e. frequencies >3P) and amplified at low frequencies. However, at $\lambda = 7$ and $\lambda = 8$, the speed fluctuations are dominated by low frequency components, particularly 1P and lower frequencies, which cause an overall increase of the amplitude of the turbine speed oscillations (Fig. 7.8). All the loads experience a near uniform mitigation across the entire spectrum. In particular, RBM fluctuations are attenuated at the peak frequencies 1P, 2P, and 3P. Therefore, the load mitigation is due to the alleviation of the oscillations of the blade incidence, despite greater oscillations of the dynamic pressure, confirming that the passive-pitch system worked as intended.

7.3 Discussion

The proof-of-concept experiments I performed in FloWave showed that the passive-pitch system can mitigate the load fluctuations in all the tested conditions, but it was not capable of generating the same average loads as the

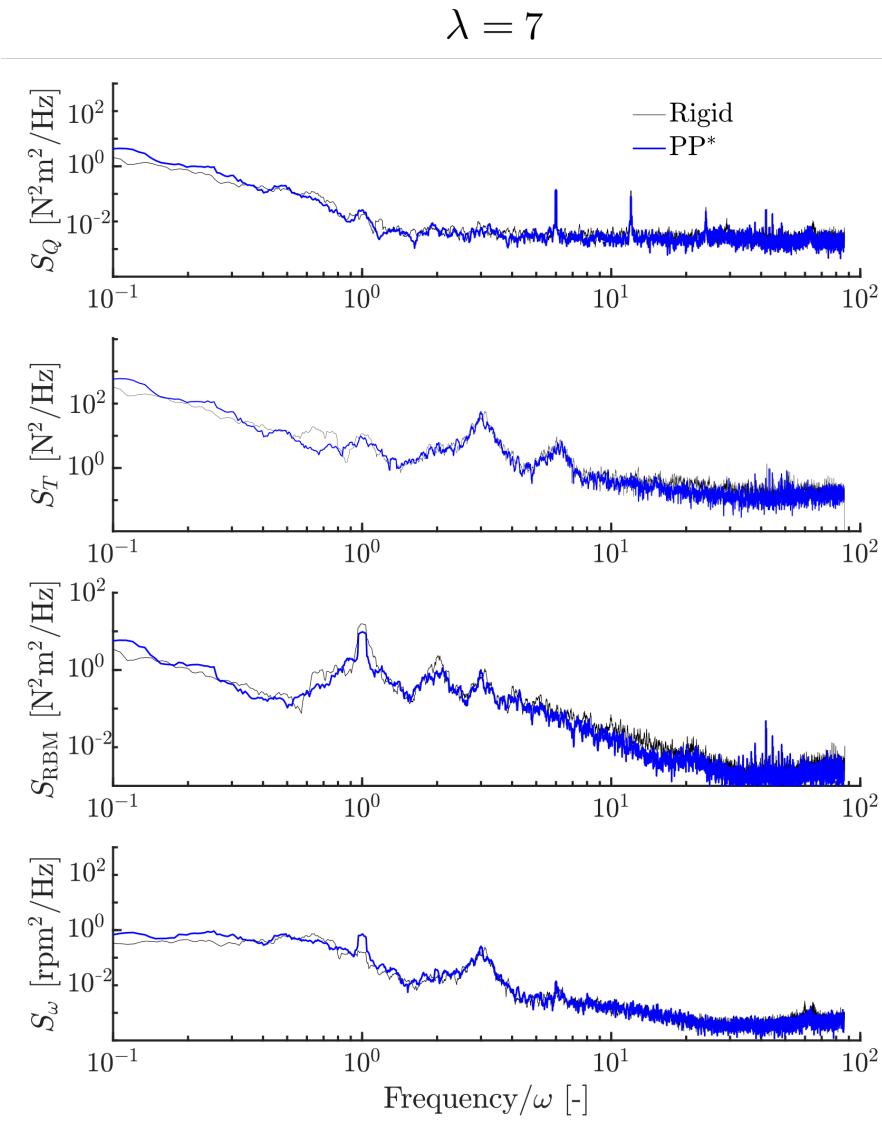

Figure 7.11: Power spectra of torque Q, thrust T, root bending moment M_{RB} and rotor speed ω at $\lambda = 7$. Each graph compares the spectra of the rigid and the passive pitch systems. (*Passive Pitch)

rigid system.

The average loads were affected by uncertainty in the installation angle of the blades and by too high/low average spring moments. The installation angle of the blade affects the average fluid loading, including the pitch moment, and it thus affects the ideal spring preload. On top of that, the uncertainty

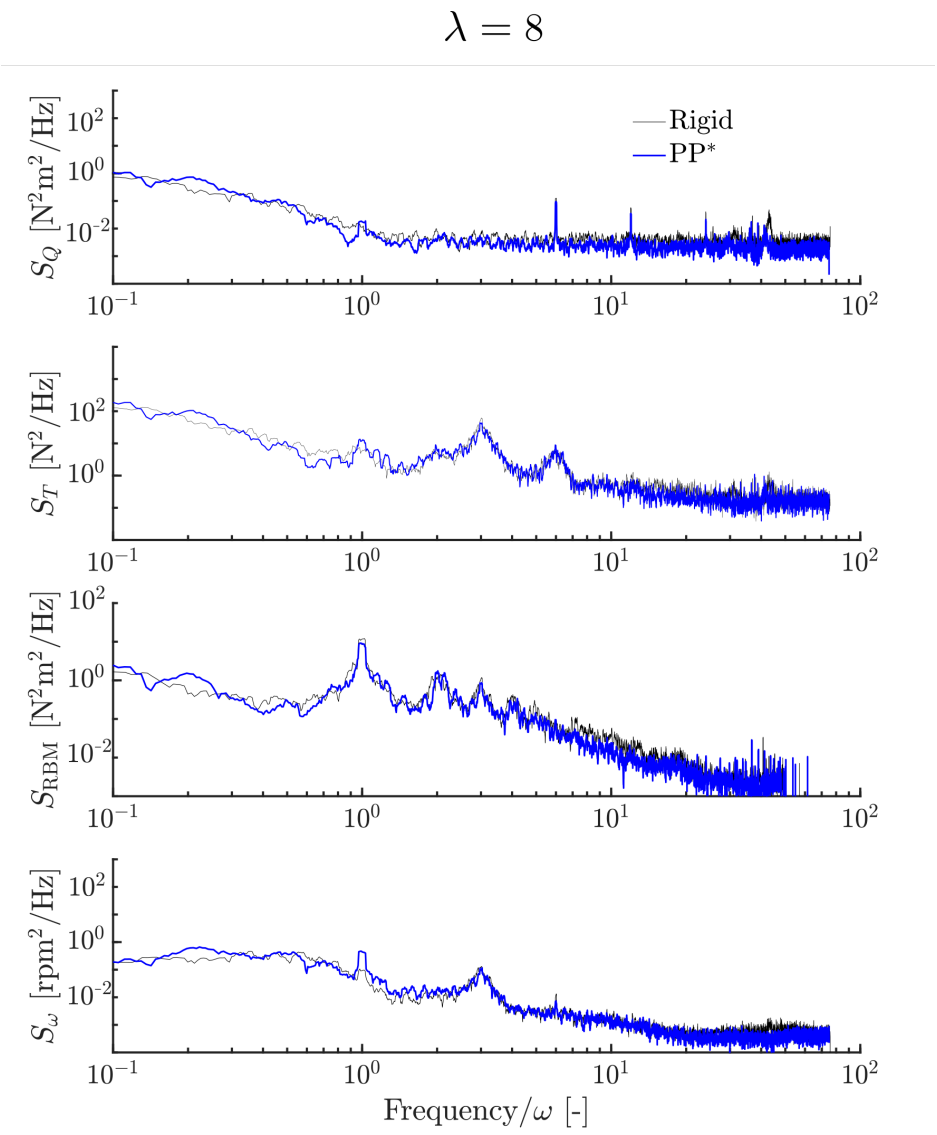

Figure 7.12: Power spectra of torque Q, thrust T, root bending moment M_{RB} and rotor speed ω at $\lambda = 8$. Each graph compares the spectra of the rigid and the passive pitch systems. (*Passive Pitch)

associated to the spring stiffness and with the prediction of the ideal preload also affected the reaction moment considerably. Therefore, the different average loads were likely caused by a combination of these factors. Nonetheless, in the absence of the preloaded spring, the blade would have pitched nose-down to a position of zero net moment, where load generation would have

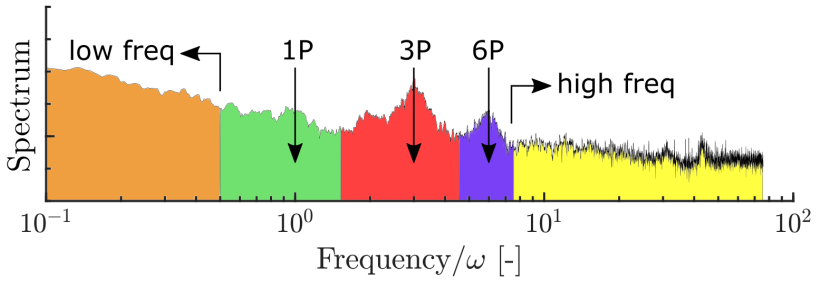

	frequency	low	1P	3P	6P	high
var r. torque [-]	$\lambda = 7$	1.03	0.80	0.84	0.89	0.81
	$\lambda = 8$	0.85	0.74	0.73	0.69	0.54
var r. thrust [-]	$\lambda = 7$	0.93	0.65	0.88	0.80	0.72
	$\lambda = 8$	0.75	0.95	0.87	1.04	0.75
var r. speed [-]	$\lambda = 7$	1.50	1.11	1.05	0.98	0.85
	$\lambda = 8$	1.32	1.18	0.95	0.91	0.71

Table 7.4: Mitigation of loads variance across different frequency components and tip speed raios. The values represent the variance of the passively pitching blade loads as a fraction of the variance of the rigid blade loads. Values smaller than one indicate a reduction of the variance associated to that frequency component.

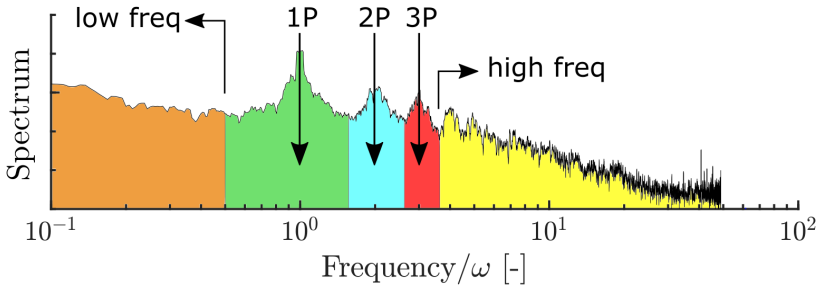

	frequency	low	1P	2P	3P	high
var r. RBM [-]	$\lambda = 7$	0.90	0.67	0.70	0.80	0.71
	$\lambda = 8$	0.65	0.83	0.98	0.77	0.71

Table 7.5: Mitigation of RBM variance across different frequency components and tip speed ratios. The values represent the variance of the passively pitching blade loads as a fraction of the variance of the rigid blade loads. Values smaller than one indicate a reduction of the variance associated to that frequency component.

been minimised. Instead, the blade reached an equilibrium position where it was generating power, confirming that the passive-pitch system behaved as expected, although performance was suboptimal. Moreover, tests with different preload angles indicated that the optimal preload is found between 275 deg and 450 deg, a value in line with the low-order code prediction.

The load fluctuations were mitigated in all the tested conditions. The fluctuations of the turbine speed contributed significantly to the performance of the system, but even in those cases where the turbine speed fluctuated more, the loads were effectively mitigated. These test highlighted the limitations of the turbine control system in two conditions. First, a rigid turbine becomes unstable when operating at low tip speed ratios and low flow speed, causing large fluctuations of the turbine speed and, hence, of the loads. Second, when operating passively-pitching blades, constant changes in the pitch angle affect the loads, particularly the torque, which affects the rotational speed and requires greater control capabilities that the control system fails to provide. Even if the passive-pitch system mitigates the first kind of instability, the self-induced instability where managed only by allowing only one blade to passively-pitch at a time.

These experiments highlighted the biggest issues that should be sorted in order to further develop the passive-pitch technology, but I believe they also provided a compelling proof that the passive-pitch system works, and that passive mitigation of load fluctuations on tidal turbine blades is a viable technology.

7.4 Differences between experiments and low-order model

The comparison between the experiments and the low-order code would be a definitive proof of the prediction capabilities of the model, and that it could be used as a reliable prediction tool to further develop the passive-pitch system technology. However, such comparison is not feasible. There are two main reasons why such comparison cannot be done: the uncertainty

in the spring preload angle and the presence of friction in the experimental model.

The spring preload was affected by several aspects. First, as discussed in Section 7.3, the uncertainty in the blade mounting angle affected the incidence of the blade, the loads, and thus the average fluid moment that had to be balanced by the spring. Hence, the blade pitched to a new angular position where the actual spring preload is unknown. Also, the springs stiffness is different from the nominal value, causing the springs to apply a different moment for a given preload angle. In summary, the actual spring preload is not known and cannot be used as input for the low-order code, and the uncertainty associated to the spring stiffness is such that even if the spring preload were known, the simulated spring moment would not be accurate.

In Section 7.2.2, I discussed the different sources of friction that affected the mitigation of the blade loads. Although I estimated the bearings friction, its effect combined to the friction between the spring and the shaft cannot be quantified. Therefore, it's not possible to model the reduction of the load mitigation capabilities of the passive-pitch system in the low-order code.

Moreover, there are other minor reasons that would affect the quality of a comparison between experiments and simulations. For instance, I developed the low-order code to capture first order phenomena that define the working principle of the passive-pitch system. However, experiments are subjected to all sorts of physical phenomena. Higher order phenomena do not define the underlying mechanics of load alleviation by morphing blade, in fact, they did not undermine the system effectiveness. However, they might affect the performance of the system. Since these phenomena are not modelled in the low-order code, they just add to the differences with the experiments.

In conclusion, it is not possible to replicate the experimental conditions using the low-order code with a degree of confidence that a comparison between experimental results and numerical simulations would be meaningful. In particular, it would not be possible to compare the performance of the passive-pitch system in its two functions, namely generation of the same

average loads as the rigid system and mitigation of the load fluctuations.

8

Conclusions

I discussed the underlying mechanism by which morphing blades can mitigate unsteady load fluctuations on tidal turbines. I considered a blade whose trailing edge can passively deflect under the effect of the hydrodynamic loads. When a gust occurs, the trailing edge deflects shedding the additional load. To investigate the governing physics, I developed a low-order model where the blade flexibility is modelled by a mass-damper-spring system. The model does not consider the exact blade shape variations but only the effect that this has on the angle of attack. Hence, it can equally represent a blade with distributed chordwise flexibility, as well as a rigid blade that passively pitches.

By neglecting mass and damping effects, and by further assuming independent blade sections at any spanwise location, I showed that a morphing blade can completely cancel the thrust fluctuations experienced by rotating in a sheared current ($> 99\%$ reduction) without affecting the mean torque and thus the energy harvested. This is possible because, when a gust occurs, the increased flow speed makes the blade to pitch and this result in a reduction in the angle of attack. The optimum blade flexibility is such that the load increase due to the higher flow speed is cancelled by the load reduction due to the lower angle of attack.

The condition that each blade section deflects independently of those at other spanwise locations is not critical for the effectiveness of the system. The opposite limiting condition is when all blade sections must pitch by the same amount, which is saying that the blade is rigid and has a passive pitching

mechanism at the root. In this case, I found that the root bending moment fluctuations are decreased by more than 98% for a 18 m diameter, 1 MW turbine in a sheared tidal current operating at a tip speed ratio of 4.5.

The effectiveness of the system is partially decreased by both the mass and damping of the system. I modelled the hydrodynamic inertia and damping with Theodorsen unsteady aerodynamic theory. I estimated the inertia of a realistic 9 m span blade, and I undertook a parameter study of the mechanical damping.

Accounting for the unsteady hydrodynamics effects and the blade inertia, the root bending moment fluctuations were reduced by more than 93%. Their effect, however, depends on the onset flow conditions. Hence, I also modelled the morphing blade in the tidal flow conditions measured at the EMEC site with more than 4 m significant wave height with a period of 10 s. In these conditions, the quasi-steady analysis predicted a reduction of the root bending moment fluctuations of 87%, with virtually no reduction of the power generated. For the dynamic analysis, the chaotic inflow conditions were approximated using a Fourier representation which allowed to apply Theodorsen theory. The morphing blade performance was lower, showing a reduction of the root bending moment fluctuations of 66%. Hence, I infer that the unsteady hydrodynamic effects and the blade inertia are important factors, but do not undermine the general effectiveness of the morphing blades.

On the other hand, a high mechanical damping can undermine the ability to mitigate unsteady loads. The damping depends on the design of the morphing blade and can be due to the viscous dissipation of the flexible material, or on the mechanical damping of a passive pitch mechanism. Our parameter study can be used in the future to estimate the unsteady load mitigation of different blade design concepts.

I validated the morphing blade idea by performing proof-of-concept experiments in FloWave, using a 1:15 scale model turbine. To maintain the closest resemblance to the low-order model, I designed a blade that could

passively-pitch but could also operate at a fixed pitch angle. Using the low-order model, I created the mechanical and hydrodynamic design, and estimated the required spring stiffness and preload. The blade were tested in a 0.8 m s^{-1} current, equivalent to a full-scale flow of 3 m s^{-1}, five different tip speed ratios, and experienced flow fluctuations due to turbulence and shear flow. The passive-pitch tests were repeated for three different preload values.

Results show that the passive-pitch system reduced the fluctuations of root bending moment, thrust and torque in all tested conditions. In all cases, the root bending moment standard deviation was reduced by more than 14%, with peak performance at tip speed ratio $\lambda = 4.5$ where fluctuations were reduced by 44.6%. The greatest performance were achieved at low tip speed ratios, as the passive-pitch system mitigated not only the fluctuations of the angle of attack but also the oscillations of the turbine rotational speed which the controller failed to maintain constant. Analysis of the power spectra revealed that high performance of the passive pitch system at low tip speed ratios are due to the mitigation of low-speed instability due to the turbine speed controller and reported also by other authors. The passive-pitch system performed well also at high tip speed ratios, where no instability occurred, mitigating load fluctuations across the whole spectrum, and giving the definitive proof of its effectiveness.

Passively-pitching blades generated different average loads compared to rigid blades. The low-order model predicted a spring preload that did not bring the desired effect. However, this issue is not due to the inaccuracy of the low-order model which, in fact, showed great agreement with more sophisticated CFD models. Differences between the experimental model and the low-order model are such that the numerical predictions are not representative of the experimental setup. In particular, the blade alignment was severely affected by uncertainty in the mounting angle, which affected the average loads and, in turn the spring preload. Moreover, bearing friction and contact friction between the shaft and the spring degraded the performance of the system. In the two cases with the highest preload, results were deemed not representative due to excessive friction between the spring and the shaft.

Both numerical and experimental models confirmed the effectiveness of a passive-pitch system to mitigate unsteady load fluctuations on tidal turbine blades to extend their lifespan and reduce the overall cost of the project. This work provided insights on the parameters affecting the performance of a morphing blade, showing that the system dynamics and the unsteady hydrodynamics can have considerable effects on the performance of the system.

8.1 Future work

Now that the physics underlying load alleviation by morphing blades has been established and that the concept has been verified experimentally, I think it is worth investigating further with focus on the choice of material for the realisation of a blade with a flexible trailing edge, and the detailed analysis of higher-order phenomena that could affect the performance of the system but could also be exploited for optimisation.

Before this technology can be adopted by the industry, more research is needed to address the need for a new structural design, to identify the materials that can be adopted, and the associated manufacturing and the supply chain. Since tidal turbine blades are typically made of a composite structure reinforced with a boxspar, the use of a novel structure and materials will require extensive testing and characterisation to guarantee reliability and survivability of the blade. Overall this paper contributes by providing insights on the underlying mechanism of morphing blades and the blade behaviour that future designs need to achieve. I believe one of the greatest challenges is to find a strategy that allows to preload the material to sustain the average loads, similarly to turning the torsional spring and locking it in a loaded configuration.

A virtue of low-order numerical models is that they reproduce only first-order phenomena and are thus representative of different practical solutions. I showed that my model can represent a blade with a flexible trailing edge as well as a passively-pitching system. The limit is that I cannot draw conclusions about higher-order phenomena and their effects on the system perfor-

mance. For instance, a continuous deformation of the blade in the chordwise direction could interact with dynamic stall vortices differently than the sharp bend of a rigid trailing edge. I believe understanding this phenomena would improve the performances of morphing blades and make them an even more attractive solution for the industry.

References

[1] Donagh Cagney, Remi Gruet, and Ocean_Energy_Europe. *Powering Homes Today, Powering Nations Tomorrow*. Tech. rep. ETIP Ocean, 2019.

[2] Atlantis Resources Ltd. *AR1500 Tidal Turbine*.

[3] Orbital Marine Power. *Orbital O2 2MW*.

[4] Ian A Milne et al. "Characteristics of the turbulence in the flow at a tidal stream power site". In: *Philosophical Transactions of the Royal Society A: Mathematical, Physical and Engineering Sciences* 371.1985 (2013), p. 20120196.

[5] Thomas AA Adcock et al. "The fluid mechanics of tidal stream energy conversion". In: *Annu. Rev. Fluid Mech* 53.1 (2021), pp. 287–310.

[6] Jo I Whelan, JMR Graham, and J Peiro. "A free-surface and blockage correction for tidal turbines". In: *Journal of Fluid Mechanics* 624 (2009), pp. 281–291.

[7] Carl L Sequeira and Robert J Miller. "Unsteady gust response of tidal stream turbines". In: *2014 Oceans-St. John's*. IEEE. 2014, pp. 1–10.

[8] Gabriel Thomas Scarlett et al. "Unsteady hydrodynamics of a full-scale tidal turbine operating in large wave conditions". In: *Renewable Energy* 143 (2019), pp. 199–213.

[9] Gabriel Thomas Scarlett and Ignazio Maria Viola. "Unsteady hydrodynamics of tidal turbine blades". In: *Renewable Energy* 146 (2020), pp. 843–855.

[10] Mohamad Osman, Richard HJ Willden, and Christopher R Vogel. "The effects of surge motion on floating horizontal axis tidal turbines". In: *International Marine Energy Journal* 3.2 (2020), pp. 45–54.

[11] Benoît Gaurier et al. "Flume tank characterization of marine current turbine blade behaviour under current and wave loading". In: *Renewable Energy* 59.Supplement C (2013), pp. 1–12. ISSN: 0960-1481.

[12] N Barltrop et al. "Wave-current interactions in marine current turbines". In: *Proceedings of the Institution of Mechanical Engineers, Part M: Journal of Engineering for the Maritime Environment* 220.4 (2006), pp. 195–203.

[13] Pascal W Galloway, Luke E Myers, and AbuBakr S Bahaj. "Quantifying wave and yaw effects on a scale tidal stream turbine". In: *Renewable energy* 63 (2014), pp. 297–307.

[14] IA Milne et al. "Blade loading on tidal turbines for uniform unsteady flow". In: *Renewable Energy* 77 (2015), pp. 338–350.

[15] IA Milne et al. "The characterisation of the hydrodynamic loads on tidal turbines due to turbulence". In: *Renewable and Sustainable Energy Reviews* 56 (2016), pp. 851–864.

[16] Christopher R. Vogel and Richard H.J. Willden. "Improving Tidal Turbine Performance Through Multi-Rotor Fence Configurations". In: *J. Mar. Sci. Appl.* 18.1 (2019), pp. 17–25. ISSN: 16719433. DOI: 10.1007/s11804-019-00072-y.

[17] Christopher R Vogel and Richard HJ Willden. "Improving tidal turbine performance through multi-rotor fence configurations". In: *Journal of Marine Science and Application* 18.1 (2019), pp. 17–25.

[18] Filiberto Tartari and Takafumi Nishino. "Numerical study on the limit of power extraction by a dense cross-stream array of wind turbines". In: *European Journal of Mechanics-B/Fluids* 65 (2017), pp. 350–358.

[19] Christopher R Vogel and Richard HJ Willden. "Investigation of wind turbine wake superposition models using Reynolds-averaged Navier-Stokes simulations". In: *Wind Energy* 23.3 (2020), pp. 593–607.

[20] Donald R Noble et al. "Experimental Assessment of Flow, Performance, and Loads for Tidal Turbines in a Closely-Spaced Array". In: *Energies* 13.8 (2020), p. 1977.

[21] Hannah Ross and Brian Polagye. "An experimental assessment of analytical blockage corrections for turbines". In: *Renewable Energy* 152 (2020), pp. 1328–1341.

[22] Nicolo' Lombardi et al. "A hybrid BEM-CFD virtual blade model to predict interactions between tidal stream turbines under wave conditions". In: *Journal of Marine Science and Engineering* 8.12 (2020), p. 969.

[23] Federico Attene et al. "Using Experimentally Validated Navier-Stokes CFD to Minimize Tidal Stream Turbine Power Losses Due to Wake/Turbine Interactions". In: *Sustainability* 12.21 (2020), p. 8768.

[24] J Schluntz and RHJ Willden. "The effect of blockage on tidal turbine rotor design and performance". In: *Renewable Energy* 81 (2015), pp. 432–441.

[25] CR Vogel, GT Houlsby, and RHJ Willden. "Effect of free surface deformation on the extractable power of a finite width turbine array". In: *Renewable Energy* 88 (2016), pp. 317–324.

[26] CR Vogel, RHJ Willden, and GT Houlsby. "Power available from a depth-averaged simulation of a tidal turbine array". In: *Renewable Energy* 114 (2017), pp. 513–524.

[27] B. Murray, S. Leen, and C. M. O Bradaigh. "Void distributions and permeability prediction for rotationally moulded polymers". In: *J. Mater. Des. Appl.* 229.5 (2015), pp. 403–418. ISSN: 1464-4207. DOI: 10.1177/1464420714525135. URL: http://pil.sagepub.com/lookup/doi/10.1177/1464420714525135.

[28] Samuel Draycott et al. "Assessing extreme loads on a tidal turbine using focused wave groups in energetic currents". In: *Renewable Energy* 135 (2019), pp. 1013–1024.

[29] Franck Scuiller et al. "A review of energy storage technologies for marine current energy systems". In: *Renew. Sustain. Energy Rev.* 18 (2013), pp. 390–400. DOI: 10.1016/j.rser.2012.10.006.

[30] James Carroll, Alasdair McDonald, and David McMillan. "Failure rate, repair time and unscheduled O&M cost analysis of offshore wind turbines". In: *Wind Energy* 19.6 (2016), pp. 1107–1119.

[31] Tatiana Delorm. "Tidal stream devices: reliability prediction models during their conceptual & development phases". PhD thesis. Durham University, 2014.

[32] Ciaran R Kennedy et al. "Fatigue life of pitch-and stall-regulated composite tidal turbine blades". In: *Renewable Energy* 121 (2018), pp. 688–699.

[33] Long Chen and Wei-Haur Lam. "A review of survivability and remedial actions of tidal current turbines". In: *Renewable and Sustainable Energy Reviews* 43 (2015), pp. 891–900.

[34] Pengfei Liu and Brian Veitch. "Design and optimization for strength and integrity of tidal turbine rotor blades". In: *Energy* 46.1 (2012), pp. 393–404.

[35] T.K. Barlas and G.A.M. van Kuik. "Review of state of the art in smart rotor control research for wind turbines". In: *Progress in Aerospace Sciences* 46.1 (2010), pp. 1–27. ISSN: 0376-0421.

[36] Torben Juul Larsen, Helge A Madsen, and Kenneth Thomsen. "Active load reduction using individual pitch, based on local blade flow measurements". In: *Wind Energy* 8.1 (2005), pp. 67–80.

[37] Xin Shen, Xiaocheng Zhu, and Zhaohui Du. "Wind turbine aerodynamics and loads control in wind shear flow". In: *Energy* 36.3 (2011), pp. 1424 –1434. ISSN: 0360-5442.

[38] J. Hu and Richard H. J. Willden. "Unsteady load relief of an axial flow tidal turbine in sheared flow by individual pitch control". In: *5th Oxford Tidal Energy Workshop*. Mar. 2016, pp. 50–51.

[39] AJ Eggers Jr et al. "Effects of blade bending on aerodynamic control of fluctuating loads on teetered HAWT rotors". In: (1996).

[40] EA Bossanyi. "Individual blade pitch control for load reduction". In: *Wind energy* 6.2 (2003), pp. 119–128.

[41] Bing Feng Ng et al. "Aeroservoelastic state-space vortex lattice modeling and load alleviation of wind turbine blades". In: *Wind Energy* 18.7 (2015), pp. 1317–1331.

[42] David M Grogan et al. "Design of composite tidal turbine blades". In: *Renewable Energy* 57 (2013), pp. 151–162.

[43] T Barlas and M Lackner. "Smart rotor blade technology applied to the Upwind reference turbine". In: *IEA Top. Expert Meet. Appl. smart Struct. large Wind turbine rotor Bl.* Sandia National Labs, Alberquerque, USA, 2008.

[44] T K Barlas, G J van der Veen, and G A M Kuik. "Model predictive control for wind turbines with distributed active flaps: incorporating inflow signals and actuator constraints". In: *Wind Energy* 15 (2012), pp. 757–771. ISSN: 1099-1824.

[45] AM Young, JR Farman, and RJ Miller. "Load alleviation technology for extending life in tidal turbines". In: *Progress in Renewable Energies Offshore-Proceedings of 2nd International Conference on Renewable Energies Offshore, RENEW 2016*. 2016, pp. 521–530.

[46] CP Van Dam et al. "Computational investigations of small deploying tabs and flaps for aerodynamic load control". In: *Journal of Physics: Conference Series*. Vol. 75. 1. IOP Publishing. 2007, p. 012027.

[47] Peter Bjoern Andersen et al. "Deformable trailing edge flaps for modern megawatt wind turbine controllers using strain gauge sensors". In: *Wind Energy: An International Journal for Progress and Applications in Wind Power Conversion Technology* 13.2-3 (2010), pp. 193–206.

[48] C Plumley et al. "Comparison of individual pitch and smart rotor control strategies for load reduction". In: *Journal of Physics: Conference Series*. Vol. 524. 1. IOP Publishing. 2014, p. 012054.

[49] Lars O Bernhammer, Gijs AM van Kuik, and Roeland De Breuker. "Fatigue and extreme load reduction of wind turbine components using smart rotors". In: *Journal of Wind Engineering and Industrial Aerodynamics* 154 (2016), pp. 84–95.

[50] Christian Bak et al. "Wind tunnel test on airfoil Risø-B1-18 with an Active Trailing Edge Flap". In: *Wind Energy: An International Journal for Progress and Applications in Wind Power Conversion Technology* 13.2-3 (2010), pp. 207–219.

[51] Santiago Basualdo. "Load alleviation on wind turbine blades using variable airfoil geometry". In: *Wind Engineering* 29.2 (2005), pp. 169–182.

[52] Eva Jost, Thorsten Lutz, and Ewald Krämer. "A parametric CFD study of morphing trailing edge flaps applied on a 10 mw offshore wind turbine". In: *Energy Procedia* 94 (2016), pp. 53–60.

[53] Peter Bæk. "Unsteady flow modeling and experimental verification of active flow control concepts for wind turbine blades". In: *PhD thesis* (2011).

[54] Vasilis Pettas et al. "Power performance optimization and loads alleviation with active flaps using individual flap control". In: *Journal of Physics: Conference Series*. Vol. 749. 1. IOP Publishing. 2016, p. 012010.

[55] Helen Markou, Peter Bjørn Andersen, and Gunner Chr Larsen. "Potential load reductions on megawatt turbines exposed to wakes using individual-pitch wake compensator and trailing-edge flaps". In: *Wind Energy* 14.7 (2011), pp. 841–857.

[56] Matthew A Lackner and Gijs van Kuik. "A comparison of smart rotor control approaches using trailing edge flaps and individual pitch control". In: *Wind Energy: An International Journal for Progress and Applications in Wind Power Conversion Technology* 13.2-3 (2010), pp. 117–134.

[57] Leonardo Bergami. "Adaptive trailing edge flaps for active load alleviation in a smart rotor configuration". In: (2013).

[58] Mingming Zhang, Bin Tan, and Jianzhong Xu. "Parameter study of sizing and placement of deformable trailing edge flap on blade fatigue load reduction". In: *Renewable Energy* 77 (2015), pp. 217–226.

[59] Peter Bjørn Andersen et al. "Load alleviation on wind turbine blades using variable airfoil geometry". In: *Proceedings of the EWEC*. 2006.

[60] A Barlas and GAM Van Kuik. "Aeroelastic modelling and comparison of advanced active flap control concepts for load reduction on the upwind 5MW wind turbine". In: *The proceedings of the 2009 European Wind Energy conference & Exhibition, March 2009, Marseille*. Citeseer. 2009.

[61] Mingming Zhang, Bin Tan, and Jianzhong Xu. "Smart fatigue load control on the large-scale wind turbine blades using different sensing signals". In: *Renewable energy* 87 (2016), pp. 111–119.

[62] Leonardo Bergami and Niels K Poulsen. "A smart rotor configuration with linear quadratic control of adaptive trailing edge flaps for active load alleviation". In: *Wind Energy* 18.4 (2015), pp. 625–641.

[63] Joachim Heinz, Niels N Sørensen, and Frederik Zahle. "Investigation of the load reduction potential of two trailing edge flap controls using CFD". In: *Wind Energy* 14.3 (2011), pp. 449–462.

[64] Mac Gaunaa and Peter Bjørn Andersen. "Load reduction using pressure difference on airfoil for control of trailing edge flaps". In: *2009 European Wind Energy Conference and Exhibition*. EWEC. 2009.

[65] Ivo Houtzager, Jan-Willem van Wingerden, and Michel Verhaegen. "Rejection of periodic wind disturbances on an experimental "smart" rotor section using lifted repetitive control". In: *2011 IEEE International Conference on Control Applications (CCA)*. IEEE. 2011, pp. 264–271.

[66] Thanasis Barlas et al. "Extreme load alleviation using industrial implementation of active trailing edge flaps in a full design load basis". In: *Journal of Physics: Conference Series*. Vol. 753. 4. IOP Publishing. 2016, p. 042001.

[67] David G Wilson et al. "Active aerodynamic blade control design for load reduction on large wind turbines". In: *European Wind Energy Conference, Marseille, France*. Vol. 26. 19. 2009, pp. 643–678.

[68] Thomas Buhl, Mac Gaunaa, and Christian Bak. "Potential load reduction using airfoils with variable trailing edge geometry". In: *Journal of Solar Energy Engineering* 127.4 (2005), pp. 503–516.

[69] JW Van Wingerden et al. "On the proof of concept of a 'smart'wind turbine rotor blade for load alleviation". In: *Wind Energy: An International Journal for Progress and Applications in Wind Power Conversion Technology* 11.3 (2008), pp. 265–280.

[70] M Frederick, EC Kerrigan, and JMR Graham. "Gust alleviation using rapidly deployed trailing-edge flaps". In: *Journal of Wind Engineering and Industrial Aerodynamics* 98.12 (2010), pp. 712–723.

[71] Damien Castaignet et al. "Full-scale test of trailing edge flaps on a Vestas V27 wind turbine: active load reduction and system identification". In: *Wind Energy* 17.4 (2014), pp. 549–564.

[72] Mingming Zhang, Xin Li, and Jianzhong Xu. "Smart control of fatigue loads on a floating wind turbine with a tension-leg-platform". In: *Renewable energy* 134 (2019), pp. 745–756.

[73] A Badcock-Broe et al. "Wave and tidal energy market deployment strategy for Europe". In: *SI Ocean* (2014).

[74] Andrew MacGillivray et al. *Ocean Energy Technology: Gaps and Barriers*. Tech. rep. 2013, pp. 1–64. URL: www.si-ocean.eu.

[75] T Gillebaart et al. "Active flap control on an aeroelastic wind turbine airfoil in gust conditions using both a CFD and an engineering model". In: *Journal of Physics: Conference Series*. Vol. 524. IOP Publishing. 2014, p. 012060.

[76] Carlo L Bottasso et al. "Load mitigation for wind turbines by a passive aeroelastic device". In: *Journal of Wind Engineering and Industrial Aerodynamics* 148 (2016), pp. 57–69.

[77] U Cordes et al. "The Adaptive Camber Concept—A passive approach for gust load alleviation on wind turbines". In: *Wind Energy* 21.9 (2018), pp. 732–744.

[78] TTB Wester et al. "High speed PIV measurements of an adaptive camber airfoil under highly gusty inflow conditions". In: *Journal of Physics: Conference Series*. Vol. 1037. 7. IOP Publishing. 2018, p. 072007.

[79] Ulrike Cordes et al. "The Influence of Adaptive Camber on Dynamic Stall". In: ().

[80] Carl C Stringer and Brian L Polagye. "Implications of biofouling on cross-flow turbine performance". In: *SN Applied Sciences* 2.3 (2020), pp. 1–13.

[81] CP Van Dam, Dale E Berg, and Scott J Johnson. *Active load control techniques for wind turbines.* Tech. rep. Sandia National Laboratories, 2008.

[82] Helge Aa Madsen et al. "The potentials of the controllable rubber trailing edge flap (CRTEF)". In: *Proceedings of EWEC*. Vol. 116. 2010.

[83] D Magagna and L. Margheritini. *Workshop on identification of future emerging technologies in the wind power sector*. Tech. rep. March. Joint Research Centre, European Commission's science and knowledge service, 2018, p. 81. DOI: 10.2760/23207.

[84] Paul Veers, Donald Lobitz, and Gunjit Bir. "Aeroelastic tailoring in wind-turbine blade applications". In: (1998).

[85] MC Cheney and PAM Spierings. "Self-regulating composite bearingless wind turbine". In: *Solar Energy* 20.3 (1978), pp. 233–240.

[86] GW Bottrell. "Passive cyclic pitch control for horizontal axis wind turbines". In: *Wind Turbine Dynamics* (1981), pp. 271–275.

[87] NM Karaolis, PJ Mussgrove, and G Jeronimidis. "Active and passive aeroelastic power control using asymmetric fibre reinforced laminates for wind turbine blades". In: *Proceedings of the 10th British Wind Energy Conference, London*. 1988, pp. 446–458.

[88] NM Karaolis, G Jeronimidis, and PJ Mussgrove. "Composite wind turbine blades: coupling effects and rotor aerodynamic performance". In: *Proc., EWEC*. Vol. 89. 1989.

[89] HJT Kooijman. *Bending-torsion coupling of a wind turbine rotor blade*. Netherlands Energy Research Foundation ECN Petten, Netherlands, 1996.

[90] GAM van Kuik and JWM Dekker. "The FLEXHAT program, technology development and testing of flexible rotor systems with fast passive pitch control". In: *Journal of Wind Engineering and Industrial Aerodynamics* 39.1-3 (1992), pp. 435–448.

[91] PA Joosse and RM van der Berg. "Development of a TenTorTube for blade tip mechanisms. Pt. 1: feasibility and material tests". In: (1996).

[92] Vincent Cognet, S Courrech du Pont, and Benjamin Thiria. "Material optimization of flexible blades for wind turbines". In: *Renewable Energy* 160 (2020), pp. 1373–1384.

[93] Vincent Cognet et al. "Bioinspired turbine blades offer new perspectives for wind energy". In: *Proceedings of the Royal Society A: Mathematical, Physical and Engineering Sciences* 473.2198 (2017), p. 20160726.

[94] DC Corbet and CA Morgan. "Report on the passive control of horizontal axis wind turbines". In: (1992).

[95] Christian Pavese, Taeseong Kim, and Juan Pablo Murcia. "Design of a wind turbine swept blade through extensive load analysis". In: *Renewable Energy* 102 (2017), pp. 21–34.

[96] Robynne E Murray et al. "Passively adaptive tidal turbine blades: Design tool development and initial verification". In: *International Journal of Marine Energy* 14 (2016), pp. 101–124.

[97] Robynne E Murray et al. "Towing tank testing of passively adaptive composite tidal turbine blades and comparison to design tool". In: *Renewable energy* 116 (2018), pp. 202–214.

[98] Fernando L Ponta et al. "The adaptive-blade concept in wind-power applications". In: *Energy for Sustainable Development* 22 (2014), pp. 3–12.

[99] Federico Zilic de Arcos, Christopher R Vogel, and Richard HJ Willden. "Hydrodynamic analysis of turbine control through blade-deformation". In: *Developments in Renewable Energies Offshore*. CRC Press, 2020, pp. 591–598.

[100] F Zilic de Arcos, Christopher Vogel, and Richard HJ Willden. "Hydrodynamic modelling of flexible tidal turbine blades". In: Technical Committee of the European Wave and Tidal Energy Conference. 2019.

[101] Piotr Krawczyk, Asfaw Beyene, and David MacPhee. "Fluid structure interaction of a morphed wind turbine blade". In: *International Journal of Energy Research* 37.14 (2013), pp. 1784–1793.

[102] Susann Tully and Ignazio Maria Viola. "Reducing the wave induced loading of tidal turbines blades through the use of a flexible blade". In: *16th Internatioal Symposium on Transport Phenomena and Dynamics of Rotating Machinery, ISROMAC 2016*. 2016.

[103] David Ingram et al. "The design and commissioning of the first, circular, combined current and wave test basin". In: *Flow3d. com* (2014).

[104] Tony Burton et al. *Wind energy handbook*. Vol. 2. Wiley Online Library, 2001.

[105] Yuwei Li et al. "Dynamic overset CFD simulations of wind turbine aerodynamics". In: *Renewable Energy* 37.1 (2012), pp. 285–298.

[106] R Lanzafame, S Mauro, and M Messina. "Wind turbine CFD modeling using a correlation-based transitional model". In: *Renewable Energy* 52 (2013), pp. 31–39.

[107] Ehsan Borouji and Takafumi Nishino. "Fluid Structure Interaction Simulations of the NREL 5 MW Wind Turbine—Part I: Aerodynamics and Blockage Effect". In: *Journal of Offshore Mechanics and Arctic Engineering* 141.2 (2019).

[108] William Hunter, Takafumi Nishino, and Richard HJ Willden. "Investigation of tidal turbine array tuning using 3D Reynolds-averaged Navier–Stokes simulations". In: *International Journal of Marine Energy* 10 (2015), pp. 39–51.

[109] Thomas AA Adcock, Scott Draper, and Takafumi Nishino. "Tidal power generation–a review of hydrodynamic modelling". In: *Proceedings of the Institution of Mechanical Engineers, Part A: Journal of Power and Energy* 229.7 (2015), pp. 755–771.

[110] Jens Norkær Sorensen and Wen Zhong Shen. "Numerical modeling of wind turbine wakes". In: *J. Fluids Eng.* 124.2 (2002), pp. 393–399.

[111] Peter Bachant, Anders Goude, and Martin Wosnik. "Actuator line modeling of vertical-axis turbines". In: *arXiv preprint arXiv:1605.01449* (2016).

[112] Ruiwen Zhao et al. "Aerodynamic analysis of a two-bladed vertical-axis wind turbine using a coupled unsteady RANS and actuator line model". In: *Energies* 13.4 (2020), p. 776.

[113] RH Miller. "The aerodynamic and dynamic analysis of horizontal axis wind turbines". In: (1983).

[114] Amanda SM Smyth, Anna M Young, and Luca Di Mare. "Effect of Three-Dimensional Geometry on Harmonic Gust–Airfoil Interaction". In: *AIAA Journal* 59.2 (2021), pp. 737–750.

[115] G JW Van Bussel. "The aerodynamics of horizontal axis wind turbine rotors explored with asymptotic expansion methods". In: (1995).

[116] *Tidal Bladed Theory Manual Version 4.3*. Tech. rep.

[117] Patrick J Moriarty and A Craig Hansen. *AeroDyn theory manual*. Tech. rep. National Renewable Energy Lab., Golden, CO (US), 2005.

[118] Stig Øye. "FLEX4. Simulation of wind turbine dynamics". In: (1996).

[119] Theodore Theodorsen. *General theory of aerodynamic instability and mechanism of flutter*. NACA Report 496. 1935.

[120] Boyd Perry. *Comparison of Theodorsen's Unsteady Aerodynamic Forces with Double Lattice Generalized Aerodynamic Forces*. National Aeronautics and Space Administration, Langley Research Center, 2017.

[121] Ulrike Cordes et al. "Note on the limitations of the Theodorsen and Sears functions". In: *Journal of Fluid Mechanics* 811 (2017).

[122] Friedrich Keune. "Lift on a bent, flat plate". In: (1955).

[123] BR Williams. "An exact test case for the plane potential flow about two adjacent lifting aerofoils". In: (1971).

[124] Cx K Batchelor and GK Batchelor. *An introduction to fluid dynamics*. Cambridge university press, 2000.

[125] David C Ives. "A modern look at conformal mapping including multiply connected regions". In: *AIAA Journal* 14.8 (1976), pp. 1006–1011.

[126] Isadore Edward Garrick. "Potential flow about arbitrary biplane wing sections". In: (1937).

[127] ND Halsey. "Potential flow analysis of multielement airfoils using conformal mapping". In: *AIAA Journal* 17.12 (1979), pp. 1281–1288.

[128] J Katz and D Weihs. "The effect of chordwise flexibility on the lift of a rapidly accelerated airfoil". In: *Aeronautical Quarterly* 30.1 (1979), pp. 360–370.

[129] J Katz and D Weihs. "Hydrodynamic propulsion by large amplitude oscillation of an airfoil with chordwise flexibility". In: *Journal of Fluid Mechanics* 88.3 (1978), pp. 485–497.

[130] J Gordon Leishman. "Unsteady lift of a flapped airfoil by indicial concepts". In: *Journal of Aircraft* 31.2 (1994), pp. 288–297.

[131] Nagarajan Hariharan and J Gordon Leishman. "Unsteady aerodynamics of a flapped airfoil in subsonic flow by indicial concepts". In: *Journal of Aircraft* 33.5 (1996), pp. 855–868.

[132] Herbert Wagner. "Über die Entstehung des dynamischen Auftriebes von Tragflügeln". In: (1924).

[133] JP Narkiewicz, A Ling, and GTS Done. "Unsteady aerodynamic loads on an aerofoil with a deflecting tab". In: *The Aeronautical Journal* 99.987 (1995), pp. 282–292.

[134] Andrzej Krzysiak and Janusz Narkiewicz. "Aerodynamic loads on airfoil with trailing-edge flap pitching with different frequencies". In: *Journal of aircraft* 43.2 (2006), pp. 407–418.

[135] Mac Gaunaa. "Unsteady two-dimensional potential-flow model for thin variable geometry airfoils". In: *Wind Energy: An International Journal for Progress and Applications in Wind Power Conversion Technology* 13.2-3 (2010), pp. 167–192.

[136] Peter Bjørn Andersen et al. "A dynamic stall model for airfoils with deformable trailing edges". In: *Wind Energy: An International Journal for Progress and Applications in Wind Power Conversion Technology* 12.8 (2009), pp. 734–751.

[137] Niels Troldborg. "Computational study of the Risø-B1-18 airfoil with a hinged flap providing variable trailing edge geometry". In: *Wind Engineering* 29.2 (2005), pp. 89–113.

[138] Tuyen Quang Le and Jin Hwan Ko. "Effect of hydrofoil flexibility on the power extraction of a flapping tidal generator via two- and three-dimensional flow simulations". In: *Renewable energy* 80 (2015), pp. 275–285.

[139] Peter Derek Yeh and Alexander Alexeev. "Free swimming of an elastic plate plunging at low Reynolds number". In: *Physics of Fluids* 26.5 (2014), p. 053604.

[140] Sébastien Michelin and Stefan G Llewellyn Smith. "Resonance and propulsion performance of a heaving flexible wing". In: *Physics of Fluids* 21.7 (2009), p. 071902.

[141] Silas Alben and Michael J Shelley. "Flapping states of a flag in an inviscid fluid: bistability and the transition to chaos". In: *Physical review letters* 100.7 (2008), p. 074301.

[142] Silas Alben. "Optimal flexibility of a flapping appendage in an inviscid fluid". In: *Journal of Fluid Mechanics* 614 (2008), pp. 355–380.

[143] Silas Alben et al. "Dynamics of freely swimming flexible foils". In: *Physics of Fluids* 24.5 (2012), p. 051901.

[144] AK Kancharala and MK Philen. "Optimal chordwise stiffness profiles of self-propelled flapping fins". In: *Bioinspiration & biomimetics* 11.5 (2016), p. 056016.

[145] Kourosh Shoele and Qiang Zhu. "Leading edge strengthening and the propulsion performance of flexible ray fins". In: *Journal of Fluid Mechanics* 693 (2012), pp. 402–432.

[146] Jie Wu et al. "How a flexible tail improves the power extraction efficiency of a semi-activated flapping foil system: A numerical study". In: *Journal of Fluids and Structures* 54 (2015), pp. 886–899.

[147] Jie Wu et al. "Numerical study on the power extraction performance of a flapping foil with a flexible tail". In: *Physics of Fluids* 27.1 (2015), p. 013602.

[148] Jonathan Toomey and Jeff D Eldredge. "Numerical and experimental study of the fluid dynamics of a flapping wing with low order flexibility". In: *Physics of Fluids* 20.7 (2008), p. 073603.

[149] Manoochehr M Koochesfahani. "Vortical patterns in the wake of an oscillating airfoil". In: *AIAA journal* 27.9 (1989), pp. 1200–1205.

[150] James C Wu. "Theory for aerodynamic force and moment in viscous flows". In: *AIAA Journal* 19.4 (1981), pp. 432–441.

[151] William Richard Graham, CW Pitt Ford, and Holger Babinsky. "An impulse-based approach to estimating forces in unsteady flow". In: *Journal of Fluid Mechanics* 815 (2017), pp. 60–76.

[152] SJ Corkery, Holger Babinsky, and WR Graham. "Quantification of added-mass effects using particle image velocimetry data for a translating and rotating flat plate". In: *Journal of Fluid Mechanics* 870 (2019), pp. 492–518.

[153] Simon J Corkery, Holger Babinsky, and John Harvey. "Response of a flat plate wing to a transverse gust at low reynolds numbers". In: *2018 AIAA Aerospace Sciences Meeting*. 2018, p. 1082.

[154] Peter Mancini, Albert Medina, and Anya R Jones. "Experimental and analytical investigation into lift prediction on large trailing edge flaps". In: *Physics of Fluids* 31.1 (2019), p. 013106.

[155] Gregory Z McGowan et al. "Investigations of lift-based pitch-plunge equivalence for airfoils at low Reynolds numbers". In: *AIAA journal* 49.7 (2011), pp. 1511–1524.

[156] Michael V Ol et al. "Shallow and deep dynamic stall for flapping low Reynolds number airfoils". In: *Animal Locomotion*. Springer, 2010, pp. 321–339.

[157] Girguis Sedky, Francis D Lagor, and Anya Jones. "Unsteady aerodynamics of lift regulation during a transverse gust encounter". In: *Physical Review Fluids* 5.7 (2020), p. 074701.

[158] Albert Medina and Maziar Hemati. "Lift Disturbance Cancellation with Fast-Flap Actuation". In: *2018 Fluid Dynamics Conference*. 2018, p. 3090.

[159] Albert Medina et al. "Revisiting conventional flaps at high deflection rate". In: *AIAA Journal* 55.8 (2017), pp. 2676–2685.

[160] Chris Garrett and Patrick Cummins. "The efficiency of a turbine in a tidal channel". In: *Journal of fluid mechanics* 588 (2007), p. 243.

[161] CR Vogel, RHJ Willden, and GT Houlsby. "Blade element momentum theory for a tidal turbine". In: *Ocean Engineering* 169 (2018), pp. 215–226.

[162] Hermann Schlichting and Klaus Gersten. *Boundary-layer theory*. Springer, 2016.

[163] DR Noble et al. "Spatial variation in currents generated in the FloWave Ocean Energy Research Facility". In: *Proceedings of the 11th European Wave and Tidal Energy Conference (EWTEC2015), Nantes, France*. 2015, pp. 6–11.

[164] Health Safety Executive. *Environmental considerations*. `http://https://www.hse.gov.uk/research/otopdf/2001/oto01010.pdf`. 2001.

[165] Ira H Abbott and Albert E Von Doenhoff. *Theory of wing sections: including a summary of airfoil data*. Courier Corporation, 2012.

[166] A Wimshurst and RHJ Willden. "Computational observations of the tip loss mechanism experienced by horizontal axis rotors". In: *Wind Energy* 21.7 (2018), pp. 544–557.

[167] Aidan Wimshurst and Richard Willden. "Spanwise flow corrections for tidal turbines". In: *International Marine Energy Journal* 1.2 (Nov) (2018), pp. 111–121.

[168] A Wimshurst and RHJ Willden. "Analysis of a tip correction factor for horizontal axis turbines". In: *Wind Energy* 20.9 (2017), pp. 1515–1528.

[169] R Lanzafame, and M Messina. "Fluid dynamics wind turbine design: Critical analysis, optimization and application of BEM theory". In: *Renewable energy* 32.14 (2007), pp. 2291–2305.

[170] Hermann Glauert. *The analysis of experimental results in the windmill brake and vortex ring states of an airscrew*. HM Stationery Office, 1926.

[171] Marshall L Buhl Jr. *New empirical relationship between thrust coefficient and induction factor for the turbulent windmill state*. Tech. rep. National Renewable Energy Lab.(NREL), Golden, CO (United States), 2005.

[172] Gunjit S Bir, Michael J Lawson, and Ye Li. "Structural design of a horizontal-axis tidal current turbine composite blade". In: *ASME 2011 30th International Conference on Ocean, Offshore and Arctic Engineering* (2011), pp. 797–808.

[173] UKERC. *Energy Data Centre*. `http://data.ukedc.rl.ac.uk/simplebrowse`. 2018.

[174] Gareth I Gretton and David M Ingram. *Development of a computational fluid dynamics model for a horizontal axis tidal current turbine*. Tech. rep. for the PerAWAT project. The University of Edinburgh, 2011.

[175] I.H. Abbott and A.E. Von Doenhoff. *Theory of Wing Sections, Including a Summary of Airfoil Data*. Dover Books on Aeronautical Engineering Series. Dover Publications, 1959. ISBN: 9780486605869.

[176] M Maureen Hand et al. *Unsteady aerodynamics experiment phase VI: wind tunnel test configurations and available data campaigns*. Tech. rep. National Renewable Energy Lab., Golden, CO.(US), 2001.

[177] NREL UAE 6 website. *UAE6 - Unsteady Aerodynamics Experiment Phase VI NREL-NASA Ames Wind Tunnel Experiment*.

[178] NN Sorensen, JA Michelsen, and S Schreck. "Navier-Stokes predictions of the NREL phase VI rotor in the NASA Ames 80-by-120 wind tunnel". In: *Wind Energy Symposium*. Vol. 7476. 2002, pp. 94–105.

[179] David Simms et al. *NREL unsteady aerodynamics experiment in the NASA-Ames wind tunnel: a comparison of predictions to measurements*. Tech. rep. National Renewable Energy Lab.(NREL), Golden, CO (United States), 2001.

[180] Paul T Lin et al. "Two-dimensional implicit time-dependent calculations on adaptive unstructured meshes with time evolving boundaries". In: *International journal for numerical methods in fluids* 50.2 (2006), pp. 199–218.

[181] Valentina Motta, Alberto Guardone, and Giuseppe Quaranta. "Influence of airfoil thickness on unsteady aerodynamic loads on pitching airfoils". In: *Journal of Fluid Mechanics* 774 (2015), pp. 460–487.

[182] Robert L Halfman. *Experimental aerodynamic derivatives of a sinusoidally oscillating airfoil in two-dimensional flow*. Vol. 2465. National Advisory Committee for Aeronautics, 1952.

[183] Weidong Dai, Gabriele Pisetta, and Ignazio Maria Viola. "Morphing blades for passive load control of tidal turbines". In: *EWTEC proceedings* (2019).

[184] Weidong Dai. "Numerical Modelling of Passively Pitching Blades for In-stream Tidal Turbines". PhD thesis. School of Engineering, University of Edinburgh, 2021.

[185] S Salter. "Proposals for a combined wave and current tank with independent 360∘ capability". In: *Proceedings Marec 2001* (2001).

[186] Steven G Parkinson and William J Collier. "Model validation of hydrodynamic loads and performance of a full-scale tidal turbine using Tidal Bladed". In: *International Journal of Marine Energy* 16 (2016), pp. 279–297.

[187] Grégory S Payne, Tim Stallard, and Rodrigo Martinez. "Design and manufacture of a bed supported tidal turbine model for blade and shaft load measurement in turbulent flow and waves". In: *Renewable Energy* 107 (2017), pp. 312–326.

[188] Ramasamy Murugan, R Ramesh, and Krishan Padmanabhan. "Investigation on static and dynamic mechanical properties of epoxy based woven fabric glass/carbon hybrid composite laminates". In: *Procedia Engineering* 97 (2014), pp. 459–468.

[189] Samuel Draycott et al. "Experimental assessment of tidal turbine loading from irregular waves over a tidal cycle". In: *Journal of Ocean Engineering and Marine Energy* 5.2 (2019), pp. 173–187.

[190] Ionut Geonea, Nicolae Dumitru, and Ilie Dumitru. "Experimental and theoretical study of friction torque from radial ball bearings". In: *IOP Conference Series: Materials Science and Engineering*. Vol. 252. 1. IOP Publishing. 2017, p. 012048.

[191] B SKF. *The SKF model for calculating the frictional moment*. `https://www.skf.com/binaries/pub12/Images/0901d1968065e9e7-The-SKF-model-for-calculating-the-frictional-movement_tcm_12-299767.pdf`. 2018.

[192] Power-Technology Talal Husseini. *The world's largest single-rotor tidal turbine*.

[193] Bryan Thwaites and RE Meyer. "Incompressible aerodynamics". In: *Journal of Applied Mechanics* 27.4 (1960), p. 760.

[194] TS Beddoes. "A third generation model for unsteady aerodynamics and dynamic stall". In: *Westland Helicopter Limited, RP-908* (1993).

[195] Zhaohui Du and MS Selig. "The effect of rotation on the boundary layer of a wind turbine blade". In: *Renewable Energy* 20.2 (2000), pp. 167–181.

[196] H Naumann and H Yeh. "Lift and pressure fluctuations of a cambered airfoil under periodic gusts and applications in turbomachinery". In: (1973).

[197] JH Horlock. "Fluctuating lift forces on aerofoils moving through transverse and chordwise gusts". In: (1968).

[198] HM Atassi. "The Sears problem for a lifting airfoil revisited-new results". In: *Journal of Fluid Mechanics* 141 (1984), pp. 109–122.

[199] Ulrike Cordes. "Experimental investigation of a passively deforming airfoil under dynamic flow conditions". In: (2016).

[200] Robert G Loewy. "A two-dimensional approximation to the unsteady aerodynamics of rotary wings". In: *Journal of the Aeronautical Sciences* 24.2 (1957), pp. 81–92.

[201] Hannah Ross and Brian Polagye. "An experimental evaluation of blockage effects on the wake of a cross-flow current turbine". In: *Journal of Ocean Engineering and Marine Energy* 6.3 (2020), pp. 263–275.

[202] Alex Fisher et al. "The gust-mitigating potential of flapping wings". In: *Bioinspiration & biomimetics* 11.4 (2016), p. 046010.

[203] Andres F Arrieta et al. "Passive load alleviation aerofoil concept with variable stiffness multi-stable composites". In: *Composite structures* 116 (2014), pp. 235–242.

[204] John Young et al. "Numerical simulation of fully passive flapping foil power generation". In: *AIAA journal* 51.11 (2013), pp. 2727–2739.

[205] CR Vogel, RHJ Willden, and GT Houlsby. "Tidal stream turbine power capping in a head-driven tidal channel". In: *Renewable Energy* 136 (2019), pp. 491–499.

[206] Yin Lu Young et al. "Adaptive composite marine propulsors and turbines: progress and challenges". In: *Applied Mechanics Reviews* 68.6 (2016).

[207] AI Winter. "Differences in fundamental design drivers for wind and tidal turbines". In: *OCEANS 2011 IEEE-Spain*. IEEE. 2011, pp. 1–10.

[208] DN Beal et al. "Passive propulsion in vortex wakes". In: *Journal of Fluid Mechanics* 549 (2006), p. 385.

[209] Jorn A Cheney et al. "Bird wings act as a suspension system that rejects gusts". In: *Proceedings of the Royal Society B* 287.1937 (2020), p. 20201748.

[210] Wei Shyy, Mats Berg, and Daniel Ljungqvist. "Flapping and flexible wings for biological and micro air vehicles". In: *Progress in aerospace sciences* 35.5 (1999), pp. 455–505.

[211] Wei Shyy et al. "Recent progress in flapping wing aerodynamics and aeroelasticity". In: *Progress in Aerospace Sciences* 46.7 (2010), pp. 284–327.

[212] Wendi Liu, Qing Xiao, and Qiang Zhu. "Passive flexibility effect on oscillating foil energy harvester". In: *AIAA Journal* 54.4 (2016), pp. 1172–1187.

[213] Sophie Ramananarivo, Ramiro Godoy-Diana, and Benjamin Thiria. "Rather than resonance, flapping wing flyers may play on aerodynamics to improve performance". In: *Proceedings of the National Academy of Sciences* 108.15 (2011), pp. 5964–5969.

[214] Chang-kwon Kang et al. "Effects of flexibility on the aerodynamic performance of flapping wings". In: *6th AIAA Theoretical Fluid Mechanics Conference*. 2011, p. 3121.

[215] Qiang Zhu and Zhangli Peng. "Mode coupling and flow energy harvesting by a flapping foil". In: *Physics of Fluids* 21.3 (2009), p. 033601.

[216] Ismail H Tuncer and Max F Platzer. "Computational study of flapping airfoil aerodynamics". In: *Journal of aircraft* 37.3 (2000), pp. 514–520.

[217] R Knoller and OF Verein. *Die Gesetze Des Luftwiderstandes. Verlag Des OSterreichischer Flugtechnischen Vereines*. 1909.

[218] IE Garrick et al. "Propulsion of a flapping and oscillating airfoil". In: *NACA report* 567 (1937), pp. 419–427.

[219] Sam Heathcote and Ismet Gursul. "Flexible flapping airfoil propulsion at low Reynolds numbers". In: *AIAA journal* 45.5 (2007), pp. 1066–1079.

[220] William McKinney and James DeLaurier. "Wingmill: an oscillating-wing windmill". In: *Journal of energy* 5.2 (1981), pp. 109–115.

[221] Ramiro Godoy-Diana, Jean-Luc Aider, and José Eduardo Wesfreid. "Transitions in the wake of a flapping foil". In: *Physical Review E* 77.1 (2008), p. 016308.

[222] Qing Xiao and Qiang Zhu. "A review on flow energy harvesters based on flapping foils". In: *Journal of fluids and structures* 46 (2014), pp. 174–191.

[223] Jun Zhang. "Footprints of a flapping wing". In: *Journal of Fluid Mechanics* 818 (2017), pp. 1–4.

[224] Attila J Bergou, Sheng Xu, and Z Jane Wang. "Passive wing pitch reversal in insect flight". In: *Journal of Fluid Mechanics* 591 (2007), p. 321.

[225] Matthieu Sacher et al. "Flexible hydrofoil optimization for the 35th America's Cup with constrained EGO method". In: *Ocean Engineering* 157 (2018), pp. 62–72.

[226] Francis Hueber, Giulia Caponnetto, and Carlo Poloni. "A passively morphing trailing edge concept for sailing hydrofoil". In: (2017).

[227] JC Hunsaker and Edward Bidwell Wilson. "Report on behavior of aeroplanes in gusts". In: (1917).

[228] Brian Sellar. "Metocean Data Set from the ReDAPT Tidal Project: Part 1 of 7, 2011-2014". In: *[dataset]. School of Engineering. https://doi.org/10.7488/ds/1686.* 2016.

[229] *et al.* Kornbluh R. D. *Mechanical meta-materials.* US 7598651 B2. 2009.

[230] Karam Y. Maalawi and Mahdy T.S. Badawy. "A direct method for evaluating performance of horizontal axis wind turbines". In: *Renewable and Sustainable Energy Reviews* 5.2 (2001), pp. 175 – 190. ISSN: 1364-0321.

[231] Ulrike Cordes et al. "Experimental investigation of Passive Load Reduction under dynamic inflow conditions". In: *33rd AIAA Applied Aerodynamics Conference.* 2015, p. 3313.

[232] David Lentink. "Bioinspired flight control". In: *Bioinspiration & biomimetics* 9.2 (2014), pp. 020301–020301.

[233] Yang Zhang, Chunhua Zhou, and Haoxiang Luo. "Effect of mass ratio on thrust production of an elastic panel pitching or heaving near resonance". In: *Journal of Fluids and Structures* 74 (2017), pp. 385–400.

[234] H. Glauert. "A theory of thin aerofoils". In: *Reports and Memoranda* 910 (1924).

[235] E. Saliveros. "The aerodynamic performance of the NACA-4415 aerofoil at low reynolds numbers". MA thesis. University of Glasgow, 1988.

[236] Anna Young and Judith Farman. "Adjustable Camber for Extended Fatigue Life". In: *5th Oxford Tidal Energy Workshop*. Mar. 2016, pp. 32–33.

[237] Rodrigo Martinez, Grégory S Payne, and Tom Bruce. "The effects of oblique waves and currents on the loadings and performance of tidal turbines". In: *Ocean Engineering* 164 (2018), pp. 55–64.

[238] Tony Burton et al. "Wind Energy Handbook". In: John Wiley and Sons, Apr. 2002. Chap. 3, pp. 41–171. ISBN: 9780471489979.

[239] Yu-Jen Chen et al. "The Design and Analysis of Passive Pitch Control for Horizontal Axis Wind Turbine". In: *Energy Procedia* 61 (2014), pp. 683 –686. ISSN: 1876-6102.

[240] G.J. Leishman. *Principles of Helicopter Aerodynamics*. Cambridge aerospace series. Cambridge University Press, 2006.

[241] IA Milne et al. "The role of onset turbulence on tidal turbine blade loads". In: 2010.

[242] I.A. Milne et al. "Tidal turbine blade load experiments for oscillatory motion". In: Sept. 2011.

[243] E. A. Bossanyi. "Individual Blade Pitch Control for Load Reduction". In: *Wind Energy* 6.2 (2003), pp. 119–128. ISSN: 1099-1824.

[244] Niels Troldborg et al. "A simple atmospheric boundary layer model applied to large eddy simulations of wind turbine wakes". In: *Wind Energy* 17.4 (2014), pp. 657–669. ISSN: 1099-1824.

[245] C. Lanczos. *The Variational Principles of Mechanics*. Dover Books On Physics. Dover Publications, 1970. ISBN: 9780486650678.

[246] D. MacPhee and A. Beyene. "A flexible turbine blade for passive blade pitch control in wind turbines". In: *2011 IEEE Power Engineering and Automation Conference*. Vol. 1. 2011, pp. 196–199.

[247] Spencer R. Alexander and Peter E. Hamlington. "Analysis of turbulent bending moments in tidal current boundary layers". In: *Journal of Renewable and Sustainable Energy* 7.6 (2015), p. 063118.

[248] L. P. Chamorro et al. "On the interaction between a turbulent open channel flow and an axial-flow turbine". In: *Journal of Fluid Mechanics* 716 (2013), 658–670.

[249] Eelco Hoogedoorn, Gustaaf B. Jacobs, and Asfaw Beyene. "Aero-elastic behavior of a flexible blade for wind turbine application: A 2D computational study". In: *Energy* 35.2 (2010). ECOS 2008, pp. 778 –785. ISSN: 0360-5442.

[250] Wanan Sheng, Roderick A McD Galbraith, and Frank N Coton. "Applications of low-speed dynamic-stall model to the NREL airfoils". In: *Journal of Solar Energy Engineering* 132.1 (2010).

[251] Xavier Lachenal, Stephen Daynes, and Paul M. Weaver. "Review of morphing concepts and materials for wind turbine blade applications". In: *Wind Energy* 16.2 (2013), pp. 283–307. ISSN: 1099-1824.

[252] D. MacPhee and Asfaw Beyene. "Fluid-structure interaction of a morphing symmetrical wind turbine blade subjected to variable load". In: *International Journal of Energy Research* 37.1 (2013), pp. 69–79. ISSN: 1099-114X.

[253] David W. MacPhee and Asfaw Beyene. "Experimental and Fluid Structure Interaction analysis of a morphing wind turbine rotor". In: *Energy* 90.Part 1 (2015), pp. 1055 –1065. ISSN: 0360-5442.

[254] R.F. Nicholls-Lee. "Adaptive Composite Blades for Horizontal Axis Tidal Turbines". PhD thesis. University of Southampton, 2011.

[255] Christopher Bronn York and Sérgio Frascino Müller de Almeida. "On Extension-Shearing Bending-Twisting coupled laminates". In: *Composite Structures* 164.Supplement C (2017), pp. 10 –22. ISSN: 0263-8223.